Optical Diffraction Tomography for Single Cells

D i s s e r t a t i o n s s c h r i f t
zur Erlangung eines doctor rerum naturalium (Dr. rer. nat.)
der Fakultät Mathematik und Naturwissenschaften
der Technischen Universität Dresden

vorgelegt von

Paul Müller

geboren am 25. April 1987 in Leipzig

im März 2016

Vorgeschlagene Gutachter

Erstgutachter: Dr. Jochen Guck
Zweitgutachter: Dr. Kevin Chalut

Abstract

Analyzing the structure of a single cell based on its refractive index (RI) distribution is a common and valued approach, because it does not require any artificial markers. The RI is an inherent structural marker that can be quantified in three dimensions with optical diffraction tomography (ODT), an inverse scattering technique. This work reviews the theory of ODT and its implementation with an emphasis on single-cell analysis, identifying the Rytov approximation as the most efficient descriptor for light propagation. The accuracy of the reconstruction method is verified with *in silico* data and imaging artifacts associated with the inverse scattering approach are addressed. Furthermore, an experimental ODT setup is presented that consists of a bright-field microscope, a phase-imaging camera, and an optical trap combined with a microfluidic chip. A novel image analysis pipeline is proposed that addresses image corrections and frame alignment of the recorded data prior to the RI reconstruction. In addition, for a rotational axis that is tilted with respect to the image plane, an improved reconstruction algorithm is introduced and applied to single, suspended cells *in vitro*, achieving sub-cellular resolution.

Contents

List of Figures

List of Tables

1. Introduction

Developing novel microscopy techniques is a crucial exercise for studying the structure of individual cells. A large variety of imaging techniques exist that visualize, for instance, intracellular compartments, cytoskeletal proteins, or membranes within cells. The most common techniques are fluorescence-based and thus require fluorescent labels that bind to a specific structure of interest. However, in some cases it is important to image specimens without labels, for instance because of limited preparation time, limited access to the sample, or because the label causes unwanted modifications.

This work approaches the topic of marker-free imaging using optical diffraction tomography (ODT), an imaging technique that is compatible with commercial microscopes. ODT quantifies the 3D refractive index (RI) of a specimen, yielding information on both the magnitude of the RI at each point in space and the global structure of the specimen. This work provides a 3D reconstruction algorithm for the ODT community and describes how to resolve most obstacles that arise in ODT for single-cell analysis. The following two sections briefly introduce RI imaging and tomographic reconstruction. Chapter 2 addresses the physical concepts of light propagation through cells, concluding with a comparison between analytical and approximative descriptions. Chapter 3 examines the tomographic RI reconstruction of artificially generated data *in silico* in 3D and includes a discussion of common artifacts in diffraction tomography. The derived theory is applied *in vitro* in chapter 4, showcasing the 3D RI reconstruction of a human myelocytic leukemia cell (HL60/S4).

1.1 The refractive index – imaging without markers

The RI of a transparent object is an optical property that describes how light is diffracted as it propagates through the object. Effects such as refraction and interference that occur in biological imaging are a result of the inhomogeneous RI that is introduced by the sample. In biological tissues, the local RI is dependent on the electron density, which in turn depends on local protein and/or DNA content. This implies a connection between the RI and the mass density in biological tissues, which can be quantified by the refraction increment $\alpha \approx 0.2\,\mathrm{mL\,g^{-1}}$ [Bar52; Dav+52]. Thus, the RI of a biological tissue can serve as an inherent structural property that is defined by the local mass density.

For biological imaging, the RI holds quantitative information that can be used to characterize cells. For instance, the RI can be used to characterize the differen-

tiation state or the cell cycle stage [Pop+08; Cha+12]. In addition, the spatially resolved RI reveals sub-cellular organelles such as the nucleolus [Cho+07]. Measuring the RI allows for a marker-free and quantitative analysis of single cells and as a result, there is a lot of interest in the development of 3D RI imaging techniques.

1.2 Tomographic volume reconstruction

A truly 3D volume reconstruction of a specimen is not possible from only one single image. To obtain a 3D representation, many imaging techniques perform slicing of the imaging volume (e.g. selective plane illumination microscopy) or scan the 3D specimen directly (e.g. confocal laser scanning microscopy). Tomographic imaging takes a different approach. Here, projections of the specimen are recorded for different rotational positions of the specimen relative to the imaging system. To obtain a volume reconstruction in tomographic imaging, a post-processing step is necessary that connects the projections at different angles to the actual object. For instance, in the case of computerized tomography (CT), which is a well established imaging technique in medical applications, x-rays are used to record projection images of biological tissues from different angular directions. From these images, it is possible to reconstruct the original tissue using the inverse Radon transform. The Radon transform assumes that the x-rays travel along straight lines through the sample and that the tissue density is connected to the absorption of x-rays. There are several algorithms that can solve the inverse problem up to a certain degree of accuracy. Irrespective of the specific algorithm used, the reconstruction quality always depends on the resolution of the detector and on the number of angles that are covered during the imaging process.

The tomographic reconstruction with x-rays is fundamentally different from diffraction tomography, which is applied in this work. ODT uses visible light (400-700 nm) to image predominantly transparent objects with RI values between 1.333 (water) up to approximately 1.450 (human epidermis). The combination of object sizes that approach the scale of the imaging wavelength and RI differences that are large inevitably leads to diffraction and the inverse Radon transform becomes inaccurate. The solution to the problem is to take into account the wave nature of light (chapter 2) and to apply a reconstruction algorithm that overcomes the limitations of the inverse Radon transform (chapter 3). To demonstrate the algorithm, this work presents an experimental setup that, in combination with a novel computational image analysis pipeline, enables the 3D RI reconstruction of single, suspended cells (chapter 4).

2. Diffraction at cells

The most important prerequisite for a successful reconstruction with diffraction tomography in biological applications is to understand how light interacts with cells. Only with a proper understanding of light scattering at cells, is it possible to derive a reliable reconstruction algorithm. This chapter reviews the most common techniques that are used to simulate light propagation through cell-sized objects. The chapter especially highlights the Rytov approximation, which is well-suited to describe the interaction of light with cells even though it describes light propagation as a simple linear process. The linearization of the scattering process with the Rytov approximation allows the application of efficient inverse scattering algorithms that are discussed in chapter 3.

2.1 Light and matter

2.1.1 Amplitude and phase

The electric field generated by a plane wave of light in free space can be described by a periodic exponential function

$$\mathbf{E}(\mathbf{r}, t) = \mathbf{E_0}\, e^{i\Phi(\mathbf{r},t)} = \mathbf{E_0}\, e^{i(\mathbf{kr}-\omega t+\Phi_0)} \tag{2.1}$$

with amplitude $|\mathbf{E_0}|$, phase Φ, wave number $k = |\mathbf{k}|$, angular frequency ω, and initial phase Φ_0. When light passes through an object, there are a variety of interactions that may take place. Besides inelastic scattering processes on the atomar and molecular level that result in well-known effects such as fluorescence or Raman scattering, there are two fundamental effects resulting from material properties that influence light propagation altogether: attenuation and phase retardation. The quantity that describes these material properties is the RI n, a complex-valued number[1].

The imaginary part of the RI $\mathfrak{Im}(n)$ determines the attenuation of the amplitude $|\mathbf{E_0}|$. In a material with imaginary RI greater than zero, the transmission of light decreases exponentially with the propagation distance. It is important to note that the structures observed in bright field images are a result of interference and

[1]The RI takes the form of a complex-valued tensor in birefringent materials such as calcite. In biological tissues, collagen is known to form birefringent structures in the extracellular space that can be visualized using polarized light microscopy [Wol+86]. The methods described in this work do not consider birefringence of collagen which is abundant in the extracellular matrix of e.g. skin or bone tissue.

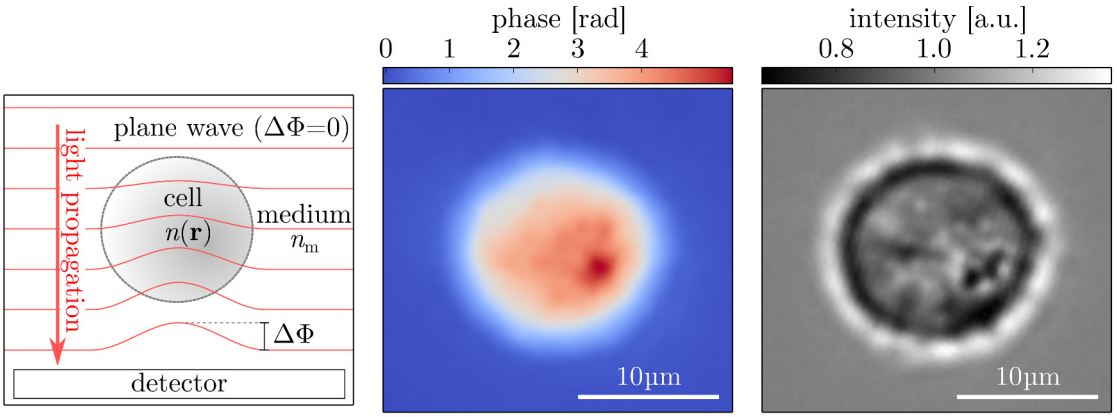

(a) axial section **(b) phase image** **(c) intensity image**

Figure 2.1, Quantitativ phase imaging of single cells. a) The schematic drawing of the cross-section along the optical axis illustrates the phase delay $\Delta\Phi$ of light passing through a cell (wavefronts drawn as red lines). The phase delay is caused by the RI of the cell $n(\mathbf{r})$, which is larger than that of the surrounding medium n_m. The images in **(b)** and **(c)** show phase and intensity images of a representative human myelocytic leukemia cell (HL60/S4). The images were recorded with the setup described in section 4.1.

must not be attributed solely to attenuation. In fact, many cells are too thin to absorb light and thus, light attenuation is not examined in this work.

The real part of a material's RI $\mathfrak{Re}(n)$ dictates the speed of light, $c = c_0/\,\mathfrak{Re}(n)$ with $\mathfrak{Re}(n) > 1$, which is lower than the speed of light in vacuum c_0. Consider two light beams that pass through a dielectric medium with an RI of n_m and that have an identical wave number $k_\mathrm{m} = kn_\mathrm{m}$. If one of the beams passed through the center of a cell with a diameter d_cell and a homogeneous RI of n_cell, it would become phase-shifted relative to the other beam propagating in the surrounding medium by

$$\Delta\Phi = d_\mathrm{cell}(k_\mathrm{cell} - k_\mathrm{m}) = d_\mathrm{cell}k(n_\mathrm{cell} - n_\mathrm{m}).$$

with $k_\mathrm{cell} = kn_\mathrm{cell}$. In quantitative phase imaging (figure 2.1), this fact is used to measure the phase delay introduced by the cell relative to the surrounding medium.

2.1.2 Phase and optical thickness

The measurement of the phase change of light that has passed through an object is always a measurement of the object's optical thickness. The optical thickness is the integral of the RI along the path of light through the object. In practice, this integral poses a problem for the determination of the 3D structure of cells, because it is not possible to obtain the spatial RI distribution or the shape of the cell from a single 2D image of its optical thickness. To uncouple the RI composition of a cell from its shape, there are two approaches. One approach makes assumptions on either the shape (e.g. sphericity) or the RI distribution of the cell (e.g. uniformity).

Consequently, the unknown variable, shape or RI, can then be extracted from the measured optical thickness. Another approach, which does not require any structural assumptions, is tomography. With tomography, it is possible to extract information on both the shape and the RI distribution of the cell. The RI of each voxel[2] is computed separately, eliminating the need for structural models that describe the optical thickness of a cell. Nevertheless, ODT reconstruction algorithms rely on approximations of light propagation. These approximations, which limit the applicability of ODT, are investigated in the following sections.

2.2 Theoretical description

In order to generate ground truth data for testing a diffraction-tomographic reconstruction algorithm, an accurate description of light propagation is essential. Light is an electromagnetic wave and its dynamic behavior and interaction with matter is fully described by the macroscopic Maxwell equations (International System of Units (SI)):

$$\nabla \cdot \mathbf{D} = \rho_\mathrm{f} \tag{2.2a}$$

$$\nabla \cdot \mathbf{B} = 0 \tag{2.2b}$$

$$\nabla \times \mathbf{E} = -\frac{\partial \mathbf{B}}{\partial t} \tag{2.2c}$$

$$\nabla \times \mathbf{H} = \mathbf{j}_\mathrm{f} + \frac{\partial \mathbf{D}}{\partial t} \tag{2.2d}$$

with the divergence $\nabla\cdot$, the curl $\nabla\times$, the time derivative $\partial/\partial t$, the free charge density ρ_f, and the free current density $\mathbf{j}_\mathrm{f}$. The Maxwell equations describe the time evolution and coupling of the electric field $\mathbf{E}$ and the magnetic field $\mathbf{B}$ components. The displacement field $\mathbf{D}$ and the magnetizing field $\mathbf{H}$ are connected to $\mathbf{E}$ and $\mathbf{B}$ by the polarization field $\mathbf{P}$ and the magnetization field $\mathbf{M}$, which describe the response of a material to an external electromagnetic field

$$\mathbf{D} = \varepsilon_0 \mathbf{E} + \mathbf{P} \tag{2.3a}$$

$$\mathbf{H} = \frac{1}{\mu_0}\mathbf{B} - \mathbf{M} \tag{2.3b}$$

with the permeability of free space ε_0 and the permittivity of free space μ_0. By introducing the material properties relative permittivity ε_r and relative permeability μ_r, the constitutive equations describe the interaction of light and matter with a simple linear relation

$$\mathbf{D} = \varepsilon_0 \varepsilon_\mathrm{r} \mathbf{E} \tag{2.4a}$$

$$\mathbf{H} = \frac{1}{\mu_0 \mu_\mathrm{r}}\mathbf{B}. \tag{2.4b}$$

[2] A voxel is the 3D equivalend of a 2D pixel.

The quantity that describes the interaction of a material with light is its RI, which is defined as $n(\mathbf{r}) = \sqrt{\varepsilon_\mathrm{r}(\mathbf{r})\mu_\mathrm{r}(\mathbf{r})}$. Unfortunately, analytical solutions to the Maxwell equations are only available for simple geometries. The description of light propagation through inhomogeneous objects, such as cells, requires numerical approaches. The following two sections discuss two computational approaches that are often used to accurately describe light propagation through objects: Mie theory and the finite-difference time-domain (FDTD) method.

2.2.1 Mie theory

Mie theory can be used in situations where the radial and angular components of the electromagnetic field can be separated. For instance, the description of light scattering at a cylinder falls into this category. Here, two parameters are used: the relative size of the cylinder diameter to the wavelength d/λ and the relative RI of the cylinder to the surrounding medium n/n_m. Because of the cylindrical symmetry of the problem, angular and radial components of the electromagnetic field can be separated using cylindrical coordinates. The solution then takes the form of an infinite series of Bessel functions [Boh+08]. In practice however, this infinite series is computed only up to the Nth term using a stop criterion that ensures numerical accuracy and stability [Wis80]. Using similar techniques, Mie theory is able provide exact solutions to light scattering problems involving cylinders, spheres, and also superpositions of spheroids [Boy+11; Boy+12].

For the purpose of this work, I generated test data for my tomographic reconstruction algorithms, using software that is based on Mie theory (see ap. B.2). Figure 2.2 showcases the computation of the electromagnetic field with Mie theory

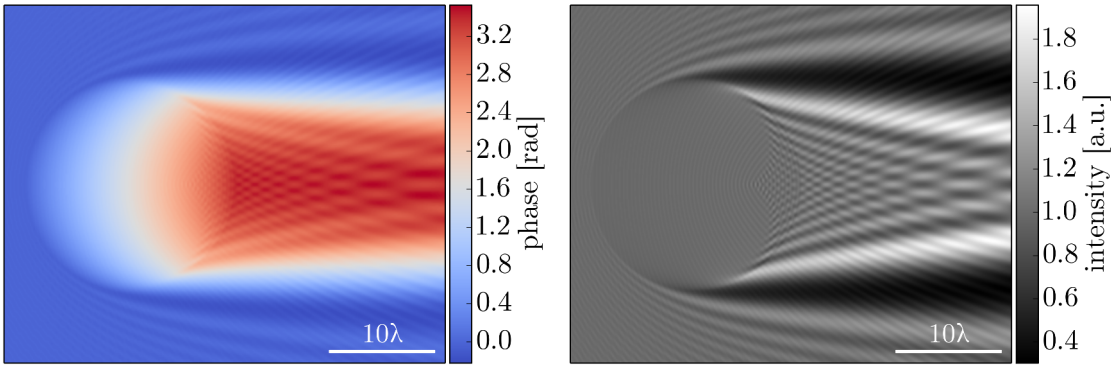

(a) scattered phase **(b) scattered intensity**

Figure 2.2, Mie theory: scattering at a cylinder. The phase **(a)** and intensity **(b)** images of a two-dimensional computation based on Mie theory illustrate how a plane wave, traveling from left to right, is scattered by a cylinder that has a diamter of 20 λ, an RI of 1.360, and that is embedded in a medium with an RI of 1.333. The electric field component was background-corrected by dividing it by the field component obtained from an empty run. The data were generated with the Python library miefield (see ap. B.2).

for a cylinder that has a diameter of 20 wavelengths[3]. The focusing effect of the cylinder, which is expected because of its convex shape, is clearly visible in the intensity image. In the phase image, the gradually increasing delay of the wave front is visible, as is schematically drawn in figure 2.1.

The advantage of computing artificial data for a centered cylinder with Mie theory is, besides the availability of an analytical solution, the rotational symmetry of the problem. Thus, to create a tomographic data set with an arbitrary number of projections, only one single simulation is required.

2.2.2 Finite-difference time-domain method

To be able to test a tomographic reconstruction algorithm for inhomogeneous objects, a corresponding simulation technique is required. In principle, one could also use Mie theory to generate test data for more complex geometries, but unfortunately, to my knowledge there is no Mie-based software package that would allow such computations. However, it is possible to address this problem from a different angle with the finite-difference time-domain (FDTD) method.

Finite-difference methods compute derivatives of a function g with respect to a variable t using the difference quotient:

$$\frac{\partial g(t)}{\partial t} \approx \frac{g(t + \Delta t/2) - g(t - \Delta t/2)}{\Delta t} \tag{2.5}$$

With this approach, divergence, curl, and time-derivative in the Maxwell equations (eqns. 2.2) can be replaced by finite differences that are then computed numerically [Yee+66; Taf+95]. For this work, I used the software MEEP [Osk+10] to perform FDTD simulations. MEEP simulations are based on the Leap-Frog iteration scheme, proposed by Yee et al. [Yee+66], which computes the vectorial components of the electric and magnetic fields on an alternating grid. This alternating computation of magnetic and electric fields is optimized for the curly Maxwell equations (2.2c, 2.2d), which each introduce a connection between orthogonal components of the electric and the magnetic field. In addition, MEEP offers an implementation of perfectly matched layers (PML), which are essential for emulating "open space". PMLs absorb radiation without reflection and when used as boundary conditions, they have the same effect as if simulated electromagnetic waves leave the simulation volume [Ber94]. An exemplary FDTD simulation of an artificial 2D cell phantom is shown in figure 2.3.

The FDTD method is a numerical method and thus, it is prone to numerical errors. Because of the nature of the discrete grid and the approximate description of derivatives, FDTD simulations exhibit a numerical dispersion that depends on the frequency and the direction of light propagation. Furthermore, due to the discretization of the grid, the object must also be discrete, which can lead to numerical errors known as the staircase effect. For the latter problem, MEEP offers

[3]The Maxwell equations are scale-invariant. Therefore, all lengths can be expressed relative to the vacuum wavelength λ. The images shown in figure 2.2 are valid for any object with the same relative RI and whose diameter is 20 times the wavelength of the light used.

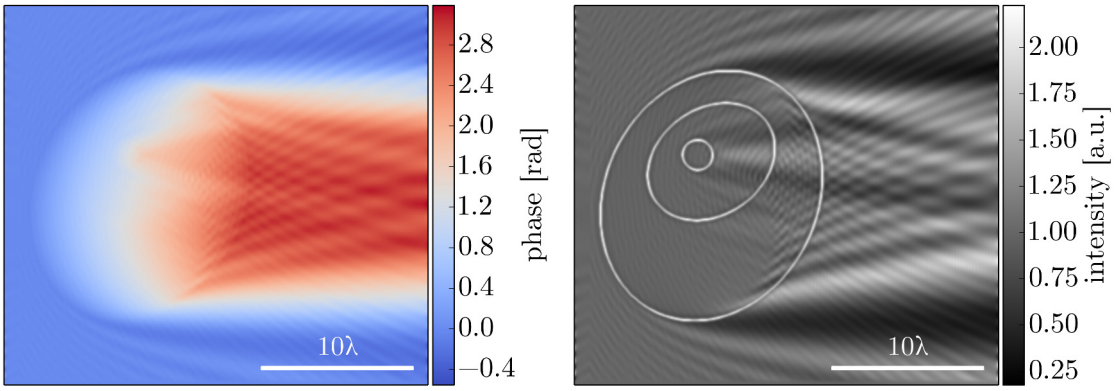

(a) scattered phase **(b) scattered intensity**

Figure 2.3, FDTD simulation: scattering at an asymmetric object. The phase **(a)** and intensity **(b)** images of a two-dimensional finite-difference time-domain (FDTD) simulation illustrate the scattering of a plane wave at an artificial cell phantom, which is outlined in white in the intensity image: The cell phantom consists of cytoplasm ($n_{\text{cytoplasm}} = 1.365$), nucleus ($n_{\text{nucleus}} = 1.360$), and nucleolus ($n_{\text{nucleolus}} = 1.387$) and is embedded in a homogeneous medium ($n_{\text{medium}} = 1.333$). These values are identical to those used in [Mül+15b]. A close look at the boundaries of the simulation (0.5λ) reveals artifacts generated by the perfectly matched layers (see text). The displayed field is the last frame of a simulation with 15 000 steps using the software MEEP. The line source is positioned 1λ away from the left side of the simulation volume and one vacuum wavelength is sampled with 13 grid cells, which corresponds to a sampling of 9.4 pixels per wavelength for $n_{\text{nucleolus}}$.

subpixel-averaging, which smoothens the boundaries of a given curvilinear interface [Far+06]. The problem of numerical dispersion can be minimized by choosing a small sampling distance. The MEEP documentation recommends a sampling distance of 8 pixels per wavelength in the highest dielectric[4]. For comparison, the simulation in figure 2.3 was performed with a sampling distance of 9.4 pixels per wavelength in the highest dielectric, the nucleolus. The drawback of the FDTD method compared to Mie theory is that it is computationally demanding: The size of the simulation volume is limited by the physically available memory and the computation time scales with the size as well[5]. It must be kept in mind that even if the parameters of an FDTD simulation are chosen carefully, balancing computation size, time, and accuracy, numerical errors cannot be avoided completely.

[4] `http://ab-initio.mit.edu/wiki/index.php/Meep_Tutorial#Fields_in_a_waveguide`, accessed Jan 22nd 2016.

[5] A single MEEP simulation with a simulation size of $390 \times 260 \times 260$ voxels and a total number of 15 000 time steps requires about 12 GB of memory and 4-6 h of computation time on an Intel Core i7-3820 CPU @ 3.60 GHz.

2.3 Approximative description

All tomographic reconstruction algorithms are based on assumptions concerning the forward, light scattering process. For instance, tomographic reconstruction algorithms in CT are based on the Radon transform [Rad17; Kak+01], which assumes that light travels along straight lines through the imaged object. While this is a good assumption for imaging human tissue with x-rays, it inaccurately describes the propagation of visible light through cells. As the wavelength approaches the size of the imaged object, diffraction becomes more relevant and the description of the scattering process must involve the wave nature of light. The methods discussed so far, Mie theory and the FDTD method, accurately describe light propagation with the Maxwell equations (eqns. 2.2), but are not an appropriate starting point for tomographic reconstruction, because they are computationally too expensive. This raises the question, whether there exist approximative descriptions of light propagation that yield a good balance between accuracy and computational cost and are thus applicable are applicable to objects such as single cells.

In certain cases, there are approximations that accurately describe the interaction of light and matter. For instance, if the object is much smaller than the used wavelength, then the Rayleigh approximation applies, which explains why the sky is blue. If on the other hand, the object is much larger than the used wavelength, then geometric optics applies, which accurately describes reflection and transmission at the boundary between two media. Neither of the two approximations is applicable for light propagation through cells, because the cell size and the imaging wavelength are at most two orders of magnitude apart. As a result, diffraction takes place and the wave nature of light must be taken into account.

2.3.1 The Helmholtz equation

To simplify the description of light propagation through single cells, the time-dependent electromagnetic field ($\mathbf{D}(\mathbf{r},t)$, $\mathbf{H}(\mathbf{r},t)$) is commonly replaced by a time-independent scalar field ($u(\mathbf{r})$), assuming that the observed system is stationary and that the coupling between the vectorial field components is negligible.

According to the Maxwell equations (eqns. 2.2), light propagation in a homogeneous medium follows the wave equation, which is valid for both the electric displacement field $\mathbf{D}$ and the magnetizing field $\mathbf{H}$:

$$\frac{\partial^2}{\partial t^2}\,\mathbf{D}(\mathbf{r},t) - \left(\frac{c_0}{n_\mathrm{m}}\right)^2 \cdot \nabla^2\,\mathbf{D}(\mathbf{r},t) = 0 \tag{2.6}$$

Note that the speed of the propagating wave c_0/n_m is dependent on the (real-valued) RI of the medium n_m. In a homogeneous medium, the direction in which the field oscillates can be arbitrary and thus, its vectorial nature can be omitted. The vector field $\mathbf{D}(\mathbf{r},t)$ my be replaced by a scalar field $\Psi(\mathbf{r},t)$:

$$\frac{\partial^2}{\partial t^2}\,\Psi(\mathbf{r},t) - \left(\frac{c_0}{n_\mathrm{m}}\right)^2 \cdot \nabla^2\,\Psi(\mathbf{r},t) = 0 \tag{2.7}$$

Furthermore, the time dependence of the wave equation can be neglected, because the scattering problem is stationary. Using separation of variables, the homogeneous Helmholtz equation can be derived [CT+92]

$$\left(\nabla^2 + {k_\mathrm{m}}^2\right) u_0(\mathbf{r}) = 0 \tag{2.8}$$

$$\text{with the wavenumber } \; k_\mathrm{m} = \frac{2\pi n_\mathrm{m}}{\lambda}. \tag{2.9}$$

The homogeneous Helmholtz equation is a second order ordinary differential equation that has plane wave solutions of the form

$$u_0(\mathbf{r}) = a_0 \exp(i k_\mathrm{m}\, \mathbf{s}_0 \cdot \mathbf{r})\,, \tag{2.10}$$

where $\mathbf{s}_0$ is the normal unit vector and a_0 is the amplitude of the plane wave. Note that the *scalar* representation of the electromagnetic field is only correct in a homogeneous medium. In an inhomogeneous medium, the three vectorial field components couple at gradients in the RI. However, this coupling, which amounts to only about 2-10 %[6], is commonly disregarded for studying the RI of cells. This negligence of the coupling between the vectorial field components is an important approximation towards a simpler description of light propagation in inhomogeneous media.

To describe an inhomogeneous medium with the Helmholtz equation, an inhomogeneity $f(\mathbf{r})$ is introduced that is defined by an RI distribution $n(\mathbf{r})$ different from that of the surrounding medium n_m,

$$\left(\nabla^2 + {k_\mathrm{m}}^2\right) u(\mathbf{r}) = -f(\mathbf{r})\, u(\mathbf{r}), \tag{2.11}$$

$$\text{with } f(\mathbf{r}) = {k_\mathrm{m}}^2 \left[\left(\frac{n(\mathbf{r})}{n_\mathrm{m}}\right)^2 - 1\right] \tag{2.12}$$

$$\text{and } n(\mathbf{r}) = n_\mathrm{m} + \epsilon_n(\mathbf{r}). \tag{2.13}$$

In the next two sections, equation 2.11, the inhomogeneous Helmholtz equation, is used as a starting point for deriving both the Born and the Rytov approximation for light propagation through inhomogeneous objects. The Born approximation makes the assumption that the scattered field is small, whereas the Rytov approximation assumes that the RI within the scattering object has a small gradient.

2.3.2 The Born approximation

In scattering theory as well as in quantum mechanics, the Born approximation is a well-known approach to approximate the interaction of a wave or particle with the scattering potential $f(\mathbf{r})$. The Born approximation requires a Green's

[6] For a sphere embedded in water ($n_\mathrm{m} = 1.333$) with a diameter of 12λ and an RI of 1.339, the amplitude of the perpendicular field components have a maximum at about 2 % of the original amplitude of the polarized light. Increasing the RI of the sphere to 1.360 results in a maximum at about 10 %. These estimates were made based on data generated by GMM-FIELD (data not shown) [Rin08].

function $G(\mathbf{r})$, a solution to the inhomogeneous problem, which in the case of the inhomogeneous Helmholtz equation is [Mor+53]

$$\left(\nabla^2 + {k_\mathrm{m}}^2\right) G(\mathbf{r}-\mathbf{r}') = -\delta(\mathbf{r}-\mathbf{r}') \tag{2.14a}$$

$$G(\mathbf{r}-\mathbf{r}') = \frac{\exp(ik_\mathrm{m}\,|\mathbf{r}-\mathbf{r}'|)}{4\pi\;|\mathbf{r}-\mathbf{r}'|}. \tag{2.14b}$$

The scattered wave $u(\mathbf{r})$ can then be described as a convolution of the product $u(\mathbf{r})f(\mathbf{r})$ with the Green's function $G(\mathbf{r})$. With the assumption that $u(\mathbf{r})$ is a sum of an incident plane wave $u_0(\mathbf{r})$ and a scattered component $u_\mathrm{s}(\mathbf{r})$

$$u(\mathbf{r}) = u_0(\mathbf{r}) + u_\mathrm{s}(\mathbf{r}), \tag{2.15}$$

the Lippmann-Schwinger equation can be derived [CT+92]

$$u(\mathbf{r}) = u_0(\mathbf{r}) + \int d^3r'\, G(\mathbf{r}-\mathbf{r}')\, f(\mathbf{r}')\, u(\mathbf{r}'). \tag{2.16}$$

In the Lippmann-Schwinger equation, the field $u(\mathbf{r})$ does not only appear on the left side, but also in $u_\mathrm{s}(\mathbf{r})$, the integral on the right side of equation 2.16. The approach of the Born approximation is to make an approximation for $u(\mathbf{r})$. It is assumed that the plane wave $u_0(\mathbf{r})$ is large compared to the integral on the right side ("$u_\mathrm{s}(\mathbf{r}) \ll u_0(\mathbf{r})$"). Therefore, in the first[7] Born approximation $u_\mathrm{B}(\mathbf{r})$, $u(\mathbf{r})$ in the integral is replaced with the incident wave $u_0(\mathbf{r})$.

$$u(\mathbf{r}) \overset{\text{Born}}{\approx} u_0(\mathbf{r}) + u_\mathrm{B}(\mathbf{r}) \tag{2.17}$$

$$\left(\nabla^2 + {k_\mathrm{m}}^2\right) u_\mathrm{B}(\mathbf{r}) = -f(\mathbf{r})\, u_\mathrm{B}(\mathbf{r}), \tag{2.18}$$

$$u_\mathrm{B}(\mathbf{r}) = \int d^3r'\, G(\mathbf{r}-\mathbf{r}')\, f(\mathbf{r}')\, u_0(\mathbf{r}') \tag{2.19}$$

What are the conditions of validity for the Born approximation? It is difficult to interpret the relation "$u_\mathrm{s}(\mathbf{r}) \ll u_0(\mathbf{r})$", because $u(\mathbf{r})$ and $u_0(\mathbf{r})$ are complex fields and the "$\ll$"-sign is not defined for complex numbers. However, it is known that cells mostly have a real-valued RI and are thus phase-shifting-only objects. Therefore, the above relation can be replaced by a comparison to the absolute phase change that a cell introduces. In a simplified model, this phase change $\Delta\Phi$ is described by the relative optical thickness Δd_opt,

$$\Delta\Phi = \frac{2\pi}{\lambda}\Delta d_\mathrm{opt} = \frac{2\pi}{\lambda} d_\mathrm{cell}(n_\mathrm{cell} - n_\mathrm{m}), \tag{2.20}$$

for a cell with an average RI n_cell and a diameter d_cell. The phase of a complex number may range from 0 to 2π. Thus, if the scattered field $u_\mathrm{s}(\mathbf{r})$ is to be much

[7] Higher order Born approximations are possible, which iteratively replace $u(\mathbf{r})$ in the integral with the right side of the equation. These however, are not considered in this work.

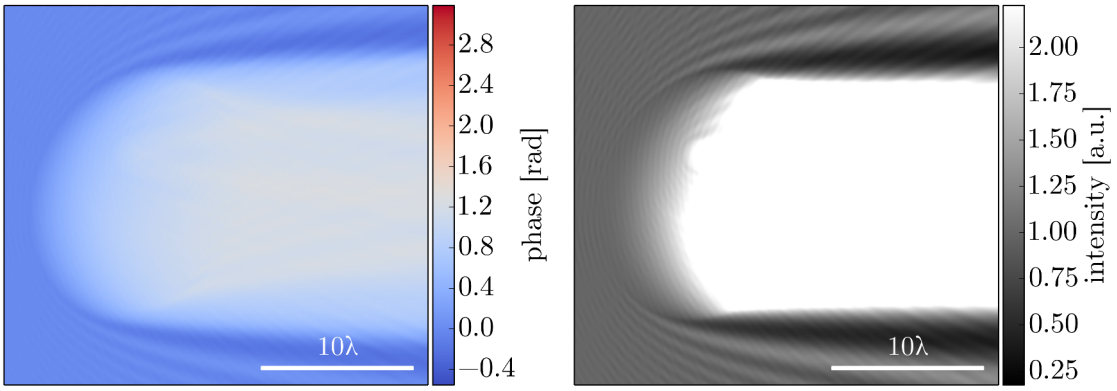

(a) scattered phase **(b) scattered intensity**

Figure 2.4, Born approximation: scattering at an asymmetric object. The figure shows the electric field computed with the Born approximation for the same phantom that was used with the finite-difference time-domain method (fig. 2.3). The color scale for the phase (a) and intensity (b) images are identical to those used in figure 2.3. The strong deviation from the expected result shows that the Born approximation is not suited to describe light propagation through cells.

smaller than the incident wave $u_0(\mathbf{r})$, then the total phase change introduced by $u_s(\mathbf{r})$ must be much smaller than 2π.

$$\Delta\Phi \ll 2\pi \tag{2.21}$$

$$d_{\text{cell}}(n_{\text{cell}} - n_{\text{m}}) = \Delta d_{\text{opt}} \ll \lambda \tag{2.22}$$

Therefore, for dielectric objects, the Born approximation is only valid if the relative optical thickness of the sample Δd_{opt} is much smaller than the imaging wavelength λ. This is a strong restriction that is certainly not valid for cells, because the phase retardation introduced by cells often reaches values above π (see fig. 2.1b). An attempt to simulate a scattering process with the Born approximation is visualized in figure 2.4. The Born approximation fails to reproduce the behavior of the FDTD method observed in figure 2.3. Therefore, the Born approximation is not suited to simulate light propagation through cell-like objects.

2.3.3 The Rytov approximation

The Born approximation is not suitable for single-cell tomography, because the optical thickness of cells is too large. The Rytov approximation takes a different approach, which results in other restrictions and makes it applicable to single cells. The approach is to transform the scattered wave $u(\mathbf{r})$ and the incident wave $u_0(\mathbf{r})$

into exponentials with a complex phase φ

$$u(\mathbf{r}) = \exp(\varphi(\mathbf{r})) \tag{2.23a}$$
$$u_0(\mathbf{r}) = \exp(\varphi_0(\mathbf{r})) \tag{2.23b}$$
$$\varphi(\mathbf{r}) = \varphi_0(\mathbf{r}) + \varphi_\mathrm{s}(\mathbf{r}). \tag{2.23c}$$

The imaginary part of the complex phase is the physical phase of the wave Φ, whereas the real part of the complex phase is the logarithm of the amplitude a.

$$\varphi(\mathbf{r}) = i\Phi(\mathbf{r}) + \ln(a(\mathbf{r})) \tag{2.24a}$$
$$\varphi_0(\mathbf{r}) = i\Phi_0(\mathbf{r}) + \ln(a_0(\mathbf{r})) \tag{2.24b}$$

To derive the Rytov approximation, these complex phases are substituted in the Helmholtz equation (eqns. 2.8, 2.11). Subsequent derivations, which are described in detail in appendix A.1, lead to an expression for the complex phase $\varphi_\mathrm{s}(\mathbf{r})$ that is surprisingly similar to the inhomogeneous Helmholtz equation.

$$(\nabla^2 + {k_\mathrm{m}}^2)u_0(\mathbf{r}) \underbrace{\varphi_\mathrm{s}(\mathbf{r})}_{\overset{\text{Rytov}}{\approx}\varphi_\mathrm{R}(\mathbf{r})} = -u_0(\mathbf{r}) \underbrace{[(\nabla\varphi_\mathrm{s}(\mathbf{r}))^2 + f(\mathbf{r})]}_{\overset{\text{Rytov}}{\approx} f(\mathbf{r})} \tag{2.25}$$

The Rytov approximation replaces the complex phase $\varphi_\mathrm{s}(\mathbf{r})$ with the Rytov phase $\varphi_\mathrm{R}(\mathbf{r})$, which corresponds to a scattered field component of

$$\begin{aligned} u_\mathrm{s}(\mathbf{r}) \approx u_\mathrm{R}(\mathbf{r}) = u(\mathbf{r}) - u_0(\mathbf{r}) &= \exp(\varphi_\mathrm{R}(\mathbf{r}) + \varphi_0(\mathbf{r})) - \exp(\varphi_0(\mathbf{r})) \\ &= u_0(\mathbf{r})[\exp(\varphi_\mathrm{R}(\mathbf{r}) - 1)]. \end{aligned} \tag{2.26}$$

The similarity of the inhomogeneous Helmholtz equation in the Born approximation (eq. 2.18) and equation 2.25 suggests the connection

$$\varphi_\mathrm{R}(\mathbf{r})u_0(\mathbf{r}) = u_\mathrm{B}(\mathbf{r}) \tag{2.27}$$

and, together with equation 2.26, reveals that the Rytov approximation can be expressed in terms of the Born approximation [Kak+01; Wol69]

$$u_\mathrm{B}(\mathbf{r}) = u_0(\mathbf{r}) \ln\left(\frac{u_\mathrm{R}(\mathbf{r})}{u_0(\mathbf{r})} + 1\right). \tag{2.28}$$

This simple[8] translation from Born to Rytov approximation is an extremely important relation. It allows to reuse the much simpler description of the Born approximation, a convolution with the Green's function, for the Rytov approximation. Thereby, both the simulation of light propagation and the tomographic

[8] In practice, this transform requires a phase-unwrapping step [Che+98] for the imaginary part of the complex Rytov phase. However, with the powerful phase-unwrapping algorithms available today (e.g. [Her+02]), this is not an issue.

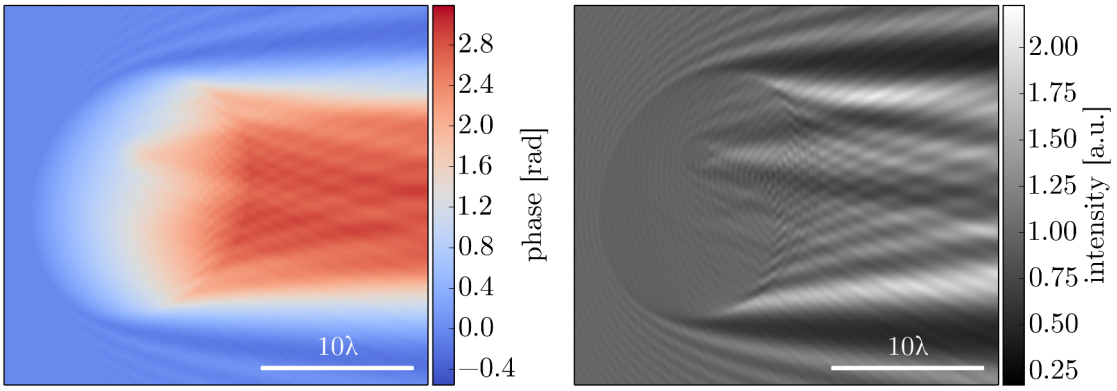

(a) scattered phase **(b) scattered intensity**

Figure 2.5, Rytov approximation: scattering at an asymmetric object. In contrast to the Born approximation (fig. 2.4), the Rytov approximation agrees well with the expected field computed using the finite-difference time-domain method (fig. 2.3). Thus, the Rytov approximation is suitable to describe light propagation through cells.

reconstruction using the Born approximation can be extended to support the Rytov approximation by adding a single computational step.

What are the conditions of validity for the Rytov approximation? As estimated in appendix A.1, the Rytov approximation is valid for a characteristic distance $d_\mathrm{c} > \lambda$ of the sample below which light propagation can be approximated to follow a straight line if [Mül+15d]

$$|\nabla n(\mathbf{r})| \ll \frac{\sqrt{2n_\mathrm{m}|n(\mathbf{r}) - n_\mathrm{m}|}}{d_\mathrm{c}}. \tag{2.29}$$

This criterion of validity is different than that for the Born approximation, because it does not restrict the absolute optical thickness of the sample. Instead, it restricts the gradient of the RI $\nabla n(\mathbf{r})$. For the Rytov approximation to be valid, the gradient of the RI must be small compared to the relative difference between the RIs of the cell and the medium $(n_\mathrm{cell} - n_\mathrm{m})$. The Rytov approximation breaks down when there are large jumps in the RI. A scattering process with the Rytov approximation is illustrated in figure 2.5 for the same cell phantom that was used for the FDTD method (fig. 2.3) and for the Born approximation (fig. 2.4). A qualitative comparison of figure 2.5 with figure 2.3 shows that the Rytov approximation is well-suited for the description of light propagation through cells.

2.4 Conclusion

The data presented in this chapter suggest, that the Rytov approximation is well-suited to describe light propagation through transparent, cell-sized objects, because it is valid for a large range of RI values and because it can be described as a linear process, which makes it much faster compared to the series computation of

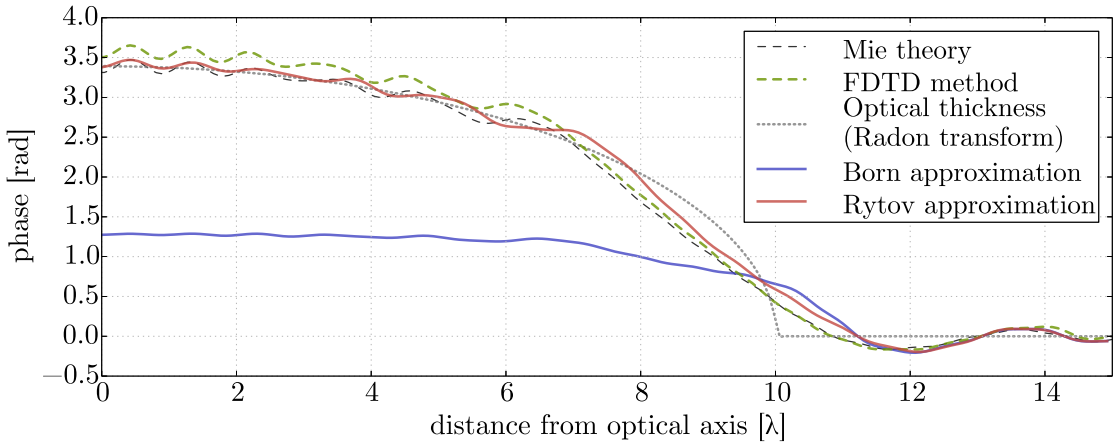

Figure 2.6, Comparison of scattering methods. The plots show the phase of the field, measured one vacuum wavelength (1λ) behind a cylinder that has a radius of 10λ, a refractive index (RI) of 1.360, and that is embedded in a medium with an RI of 1.333 (see fig. 2.2). A list of the software used to generate these data is given in appendix B.2. For each computation, one vacuum wavelength was sampled with 13 pixels. The size of the simulation volume for the Born and Rytov approximation was 30λ by 30λ. The finite-difference time-domain (FDTD) simulation was conducted in a simulation volume of the size 30λ laterally by 34λ axially and ran for 22 100 time steps. The plotted data is discussed in the text.

Mie theory or the numerical FDTD method. To compare the discussed light propagation methods, I applied them to the same problem: scattering at a dielectric cylinder. Figure 2.6 shows a comparison of the scattered phases. Several observations are important to understand the drawbacks and advantages of the different methods. First, the FDTD method slightly deviates from the exact solution (Mie theory) by an offset close to the center of the optical axis, but correctly reproduces the shape of the wavefront. Second, the phase profile computed from the optical thickness of the cylinder (Radon transform) approximately matches the expected phase, but breaks down at the boundaries of the cylinder. Third, the Born approximation fails to describe the scattering process. Fourth, the Rytov approximation yields quite accurate results that match the expected shape of the wave front. There are only minor deviations close to the boundary of the cylinder. The Rytov approximation is faster than the Mie solution or the FDTD method and thus, it is the candidate of choice for inverse scattering algorithms in diffraction tomography for cells.

3. Tomography *in silico*

The traditional approach to inverse scattering is to connect the recorded far field intensity to the Fourier transform of the imaged object. This kind of inverse scattering problem typically employs the Fraunhofer approximation and works well for 2D apertures [Goo05]. Based on this Fourier transform approach, in 1913 Bragg introduced x-ray diffraction tomography to determine the 3D structure of crystals [Bra13], which became a common technique to study the structure of crystallized proteins [AN+11]. However, this diffraction-tomographic approach with the far field is not suited for the investigation of cells, because cells are unordered structures. The theoretical foundation for diffraction tomography of cells was laid out by Wolf in 1969 [Wol69]. For diffraction tomography of weakly scattering semi-transparent objects, he proposed an inverse scattering algorithm that requires the complex-valued near field recordings.

Single-cell diffraction tomography is an imaging technique that obtains a 3D representation of the cell from multiple 2D near field recordings. Figure 3.1 illustrates the image acquisition process in diffraction tomography. An incident plane wave $u_0(\mathbf{r})$ is scattered by a scattering object with an RI distribution $n(\mathbf{r})$. Because of the difference in the RIs of the object $n(\mathbf{r})$ and the surrounding medium n_m, diffraction occurs and the wave front of the outgoing wave $u(\mathbf{r})$ is deformed. The detector records the near field of the outgoing wave for multiple rotational positions of the cell. Altogether, these recorded fields are commonly referred to as a sinogram and resemble the initial data for the tomographic reconstruction process. This chapter introduces diffraction tomography and showcases how the reconstruction algorithm performs for artificially generated sinograms.

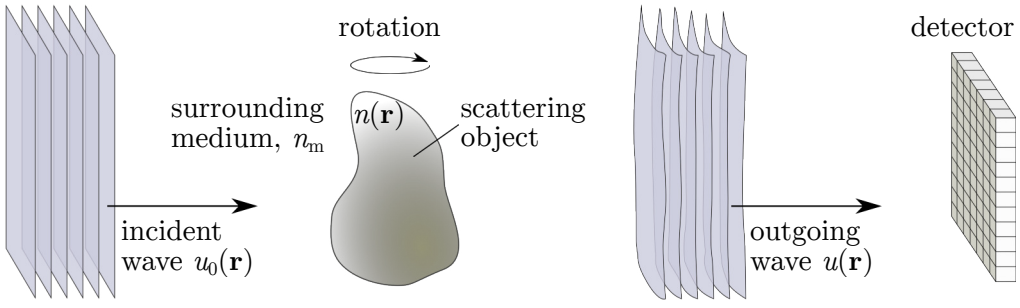

Figure 3.1, Tomographic data acquisition. An incident plane wave $u_0(\mathbf{r})$ is scattered by a transparent object with the refractive index distribution $n(\mathbf{r})$. A detector collects the scattered wave $u(\mathbf{r})$. Multi-angular acquisition is facilitated by rotation of the sample. This figure was previously published in [Mül+15d].

3.1 The inverse problem

Tomographic image reconstruction is an inverse problem: the task is to find the RI distribution $n(\mathbf{r})$ that leads to the observed projection data recorded at the detector. In order to achieve a proper reconstruction, a suitable model for the forward scattering process is required. This section introduces two reconstruction methods: one method is based on the Radon transform and the other method is based on the Rytov approximation. As indicated by the previous chapter, the Rytov approximation yields better results than the Radon transform in diffraction tomography for single cells.

3.1.1 Reconstruction without considering diffraction

Reconstruction techniques that are based on the Radon transform assume that light propagates along straight lines through the cell and thus do not take into account diffraction. Such techniques assume that the measured phase is only defined by the optical thickness of the cell, which is the integral of its RI distribution along a straight line. This section introduces the fundamentals of tomographic imaging, mediating an understanding that is crucial for understanding the more complex reconstruction algorithms encountered in diffraction tomography.

The Radon transform describes a forward scattering process that is equivalent to projecting a rotating (rotation angle ϕ_0) 2D object onto a detection line. Here, the word *projection* means that the value of one point on the detection line is computed from a line integral through the object [Rad17]. The 3D Radon transform can be

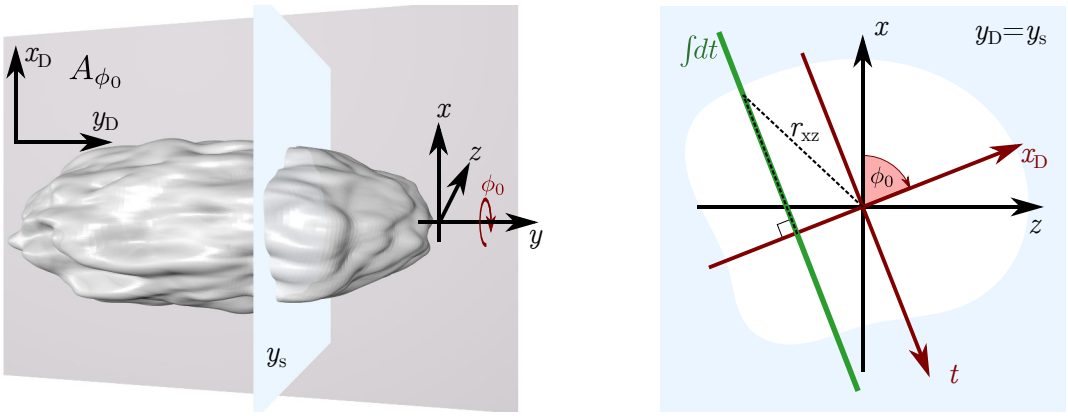

(a) 3D sketch **(b) 2D projection integral**

Figure 3.2, 3D Radon transform. a) Working principle of the three-dimensional (3D) Radon transform of a 3D object with the rotational axis y and the rotational angle ϕ_0. Light propagation takes place along the axis perpendicular to the x_D-y_D-plane. For each slice of the object at y_s (light blue), a two-dimensional (2D) Radon transform is performed. **b)** The 2D Radon transform at y_s is computed by rotation of the object (white) through ϕ_0 (red coordinate system) and integration along t (green line) perpendicular to the detector line x_D. This figure was previously published in [Mül+15d].

replaced by multiple 2D Radon transforms of slices from a 3D object. Here, the 3D object has a scattering potential $f(\mathbf{r})$ and is rotating about the y-axis. The rotational position of the object is defined by the angle ϕ_0. Then, for each slice of the sample $f(\mathbf{r})|_{y=y_\mathrm{s}}$ at y_s, the projection $p_{\phi_0}(\mathbf{r_D}) = p_{\phi_0}(x_\mathrm{D}, y_\mathrm{s})$ of this slice onto a detector plane $(x_\mathrm{D}, y_\mathrm{s})$ is described by the Radon transform operator R_{ϕ_0} (figure 3.2).

$$\begin{aligned} p_{\phi_0}(x_\mathrm{D}, y_\mathrm{s}) &= R_{\phi_0}\{ f(\mathbf{r})|_{y=y_\mathrm{s}}\}(x_\mathrm{D}) \\ &= \int dt\, f(x(t),\, y_\mathrm{s},\, z(t)) \\ &= \int dt\, f(x_\mathrm{D}\cos\phi_0 - t\sin\phi_0,\, y_\mathrm{s},\, x_\mathrm{D}\sin\phi_0 + t\cos\phi_0) \qquad (3.1) \\ r_\mathrm{xz}^2 &= x^2 + z^2 = x_\mathrm{D}^2 + t^2 \qquad (3.2) \\ x_\mathrm{D} &= x\cos\phi_0 + z\sin\phi_0 \qquad (3.3) \\ t &= -x\sin\phi_0 + z\cos\phi_0 \qquad (3.4) \end{aligned}$$

In the discrete case, where the detector is composed of a 2D grid of pixels, the line integral becomes a volume integral over a volume element of the size *pixel area* $\times$ *line length*.

The inversion of the Radon transform, the computation of the object $f(\mathbf{r})$ from the projections p_{ϕ_0}, is based on the Fourier slice theorem (see appendix A.2)

$$\widehat{F}_{\phi_0}(k_\mathrm{Dx}, 0) = \frac{1}{\sqrt{2\pi}}\widehat{P}_{\phi_0}(k_\mathrm{Dx}). \qquad (3.5)$$

The Fourier slice theorem states that the Fourier transform $\widehat{P}_{\phi_0}$ of a projection p_{ϕ_0}, measured at the angle ϕ_0, is equal to the data that are distributed along a rotated line in the Fourier transform $\widehat{F}$ of the object f, as shown in figure 3.3. This theorem is important, because it leads to two reconstruction techniques: interpolation in Fourier space and backprojection. Interpolation in Fourier space solves the reconstruction problem by interpolating all of the recorded and Fourier-transformed projections $\widehat{P}$ in Fourier space on a regular grid and then performing an inverse Fourier transform to obtain the object $f(\mathbf{r})$. For large data sets (large number of projections N_A, high resolution) and the corresponding large interpolation grids, the interpolation becomes very time-consuming and slows down the reconstruction process. In contrast, the backprojection method is not affected by this expensive interpolation task. The backprojection algorithm performs the reconstruction in real space, not in Fourier space and each of the N_A projections is backprojected onto the reconstruction volume separately (see appendix A.3).

$$f(x,z) = \frac{1}{\sqrt{2\pi}}\sum_{j=1}^{N_\mathrm{A}} \Delta\phi_0\, D_{-\phi_j}\Big\{\mathrm{FFT}_\mathrm{1D}^{-1}\left\{|k_\mathrm{Dx}|\cdot \mathrm{FFT}_\mathrm{1D}\{p_{\phi_j}(x_\mathrm{D})\}\right\}\Big\} \qquad (3.6)$$

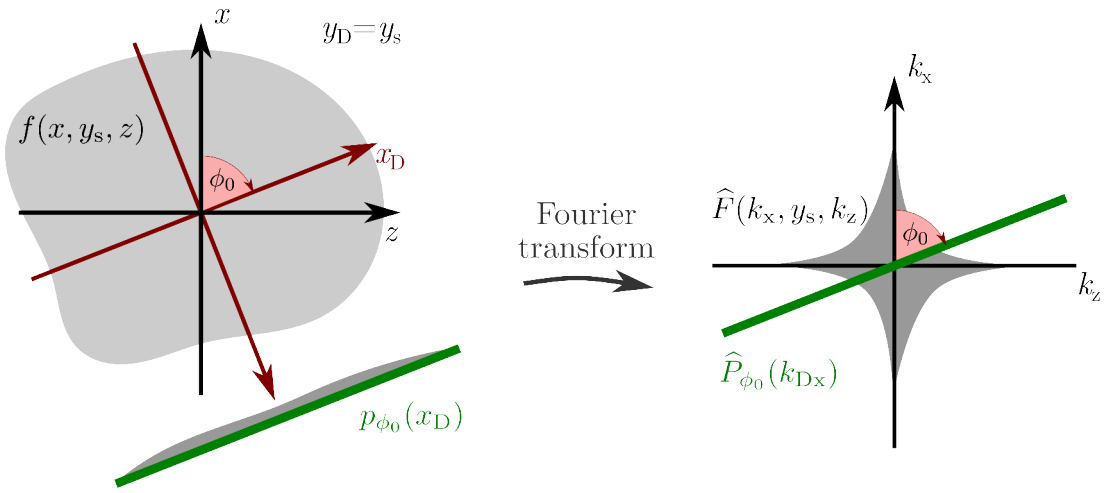

Figure 3.3, Fourier slice theorem. The theorem states that the Fourier transform $\widehat{P}$ of a projection p from an object f is equal to the Fourier transform $\widehat{F}$ of the object on a line through the origin that is tilted by the angle ϕ_0.

Here, $\Delta\phi_0 = \pi/N_A$ is the angular distance between the rotational positions of the projections, $\phi_j = j \cdot \Delta\phi_0$ are the angles at which the projections where imaged ($j = 1, 2, \ldots, N_A$), $D_{-\phi_j}$ is the rotation operator, and FFT_{1D} and FFT_{1D}^{-1} are the one-dimensional forward and inverse fast Fourier transforms. Equation 3.6 reveals a recipe for implementing the backprojection algorithm in three steps:

1. Each projection is multiplied with a ramp function $|k_{Dx}|$ in Fourier space. This filtering step can be done efficiently with the fast Fourier transform.
2. The filtered projection is backprojected (smeared) onto the image volume according to its acquisition angle ϕ_0.
3. The sum of all backprojections constitutes the reconstructed image.

Figure 3.4 shows the reconstruction of an artificial test target, a 2D cell phantom, with the backprojection algorithm. The sinogram data were generated with the FDTD method (see section 2.2.2), which is based on the Maxwell equations. As a result, the reconstruction, which is based on the Radon transform, exhibits blurring artifacts.

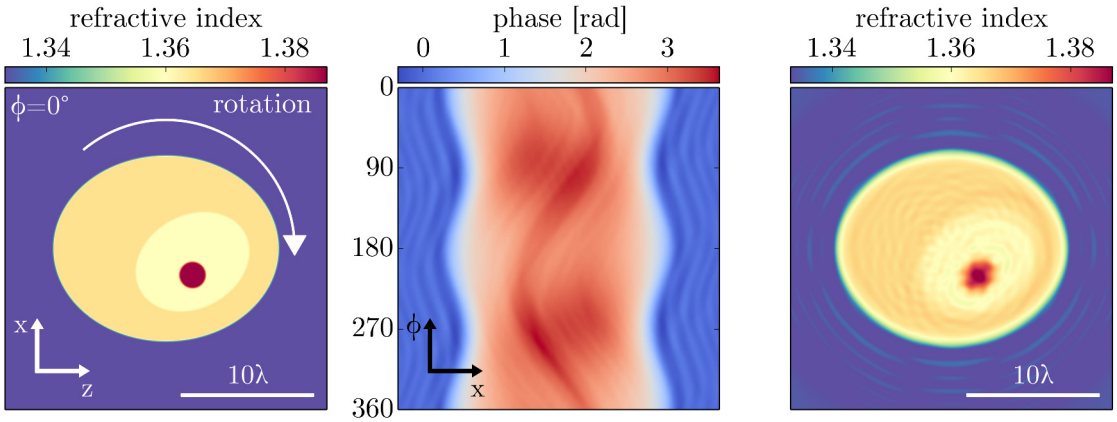

(a) phantom **(b) sinogram** **(c) backprojection**

Figure 3.4, Backprojection of an FDTD sinogram. a) The two-dimensional cell phantom is identical to that used in figures 2.3, 2.4, and 2.5. **b)** The sinogram consists of 200 projections for a full 360 degree rotation. Each finite-difference time-domain (FDTD) simulation ran for 15 000 time steps and had a resolution of 13 px/λ. **c)** The reconstruction with the backprojection algorithm is blurry, which is most easily seen in the blurred shape of the nucleolus (red dot). The reconstruction was performed with radontea [Mül13b].

3.1.2 Reconstruction with diffraction

To take into account diffraction and to improve the reconstruction quality, the Rytov approximation is commonly applied in diffraction tomography of single cells [Su+13; Kos+15; Kim+13; Sun+09]. As discussed in section 2.3.3, the Rytov approximation and the Born approximation are linked by a simple computational step

$$u_\mathrm{B}(\mathbf{r}) = u_0(\mathbf{r}) \ln\left(\frac{u_\mathrm{R}(\mathbf{r})}{u_0(\mathbf{r})} + 1\right). \tag{2.28}$$

Therefore, the tomographic reconstruction techniques derived using the Born approximation are also valid for the Rytov approximation.

The scattering process described by the Born approximation in section 2.3.2 is more complicated than the Radon transform and thus, the reconstruction process is more elaborate than the backprojection algorithm discussed in the previous section. Nevertheless, it is possible to derive a relation between the scattered field in the Born approximation $u_\mathrm{B}(\mathbf{r})$ and the Fourier transform of the image object $\widehat{F}(\mathbf{k})$ that is similar to the Fourier slice theorem (see eq. 3.5). In 2D, the Fourier diffraction theorem, illustrated in figure 3.5, states that the Fourier transform $\widehat{U}_\mathrm{B}(\mathbf{k})$ of the scattered field $u_\mathrm{B}(\mathbf{r})$ is distributed along circular arcs in Fourier space [Wol69].

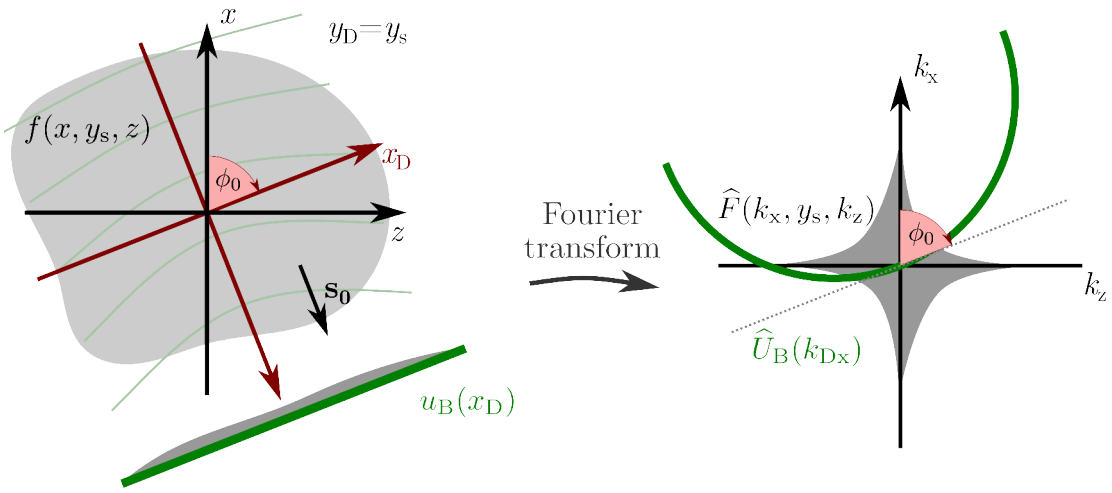

Figure 3.5, Fourier diffraction theorem in 2D. The theorem states that the Fourier transform $\widehat{U}_B$ of a scattered field from an object f in the Born approximation u_B is equal to the Fourier transform $\widehat{F}$ of the object on a semicircular arc through the origin.

$$\widehat{F}(k_m(\mathbf{s} - \mathbf{s}_0)) = -\sqrt{\frac{2}{\pi}} \frac{ik_m}{a_0} M \widehat{U}_{B,\phi_0}(k_{Dx}) \exp(-ik_m M l_D) \tag{3.7}$$

Here, k_m is the wave number of the light, a_0 is the amplitude of the incident plane wave, $\mathbf{s}_0$ is the direction of propagation of the incident plane wave, l_D is the distance between detector and center of rotation, and M is the constrained z-component of the vector $\mathbf{s}$, which forces the data onto the semi-circular arc with a radius of k_m. The subscript ϕ_0 denotes the angle of rotation that is defined by $\mathbf{s}_0$. A thorough derivation of equation 3.7 is given in appendix A.4. As for the Fourier slice theorem, a reconstruction algorithm for the Fourier diffraction theorem can be derived (see ap. A.5), which is called back*propagation* algorithm

$$f(x, z) = -\frac{ik_m}{\sqrt{2\pi}} \sum_{j=1}^{N_A} \Delta\phi_0 D_{-\phi_j} \Bigg\{ \mathrm{FFT}_{1D}^{-1} \left\{ |k_{Dx}| \cdot e^{ik_m(M-1)\left[z_{\phi_j} - l_D\right]} \cdot \mathrm{FFT}_{1D} \left\{ \frac{u_{B,\phi_j}(x_D)}{u_0(l_D)} \right\} \right\} \Bigg\}. \tag{3.8}$$

In comparison to the backprojection algorithm (eq. 3.6), the backpropagation algorithm has a filter with an additional exponential term that is dependent on the backpropagation distance z_{ϕ_j}. Thus, the 1D inverse Fourier transform FFT_{1D}^{-1} is applied to a 2D array, which is computationally more expensive compared to the backprojection algorithm where this array is 1D only. Equation 3.8 describes the backpropagation algorithm for the Born approximation. To apply the Rytov approximation, equation 2.28 is used to substitute the $u_{B,\phi_j}(x_D)$ data. A comparison between backprojection and backpropagation in 2D is shown in figure 3.6. The line

profiles through the reconstructed cell phantom for backprojection and backpropagation seem to indicate a similar reconstruction quality, which was also observed by Wedberg et al. [Wed+95]. However, the reconstruction with the backprojection algorithm is more blurred, indicating that the Rytov approximation describes the scattering problem better. Furthermore, the Born approximation breaks down (figure 3.6d), because the overall phase change is too high. In summary, the data show that diffraction tomography with the Rytov approximation yields better image reconstruction than tomography based on the inverse Radon transform.

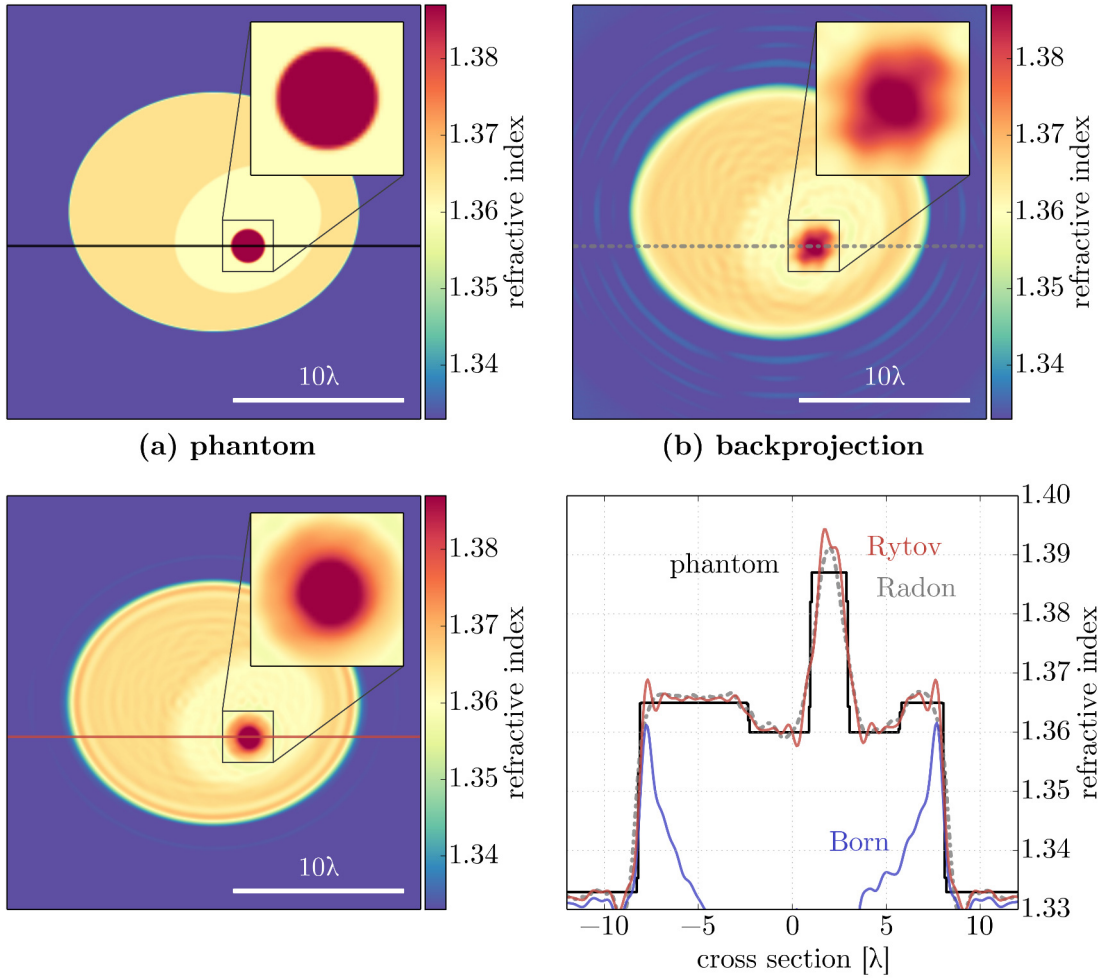

Figure 3.6, Backprojection versus backpropagation. **a)** 2D cell phantom [Mül+15b]. **b)** Reconstruction with the backprojection algorithm (inverse Radon transform). **c)** Backpropagation with the Rytov approximation. **d)** Line profiles through the nucleolus (positions indicated in the other plots). The Born approximation breaks down and fails to reconstruct the cell phantom quantitatively.

3.2 Backpropagation in 3D

In 3D, the theoretical description of diffraction tomography is similar to the 2D case [Mül+15d]. The Fourier diffraction theorem in 3D states that the Fourier transform of the detector image $\widehat{U}_{\mathrm{B}}(k_{\mathrm{Dx}}, k_{\mathrm{Dy}})$ is projected onto a semi-spherical surface as illustrated in figure 3.7. This result is analogous to the theorem in 2D, in which the data are distributed on circular arcs (see fig. 3.7). The backpropagation algorithm in 3D then becomes

$$f(x,y,z) = -\frac{ik_{\mathrm{m}}}{\sqrt{2\pi}} \sum_{j=1}^{N_{\mathrm{A}}} \Delta\phi_0 D_{-\phi_j} \Bigg\{ \mathrm{FFT}_{2\mathrm{D}}^{-1} \left\{ |k_{\mathrm{Dx}}| \cdot e^{ik_{\mathrm{m}}(M-1)\left[z_{\phi_j} - l_{\mathrm{D}}\right]} \cdot \mathrm{FFT}_{2\mathrm{D}} \left\{ \frac{u_{\mathrm{B},\phi_j}(x_{\mathrm{D}}, y_{\mathrm{D}})}{u_0(l_{\mathrm{D}})} \right\} \right\} \Bigg\}. \quad (3.9)$$

The only difference to equation 3.8 is that the dimensionality of the problem increases by one. Note that the filter in Fourier space $|k_{\mathrm{Dx}}|$ remains one-dimensional. It is always perpendicular to the rotational axis. A comparison of the backpropagation algorithm with a focus on the dimensionality of the problem is given in appendix A.5.2. As part of this work, I implemented the backpropagation algorithm for diffraction tomography with the Rytov approximation (see appendix B.5).

In order to test the implementation, I generated artificial scattering data using FDTD simulations with a 3D cell phantom. The result of such a simulation series is shown in figure 3.8. For each of the rotational positions of the cell phantom, one simulation is performed that contributes with one detector image to the resulting sinogram. In the intensity images of the sinogram, the diffraction spot generated by the nucleolus is clearly visible. Constructive and destructive interference make it appear black or white depending on its position relative to the image plane. In the phase images, the nucleolus generates a visible trace of increased phase retardation. The artificial sinogram corresponds to aligned raw data from a tomographic experiment and is the starting point for backpropagation.

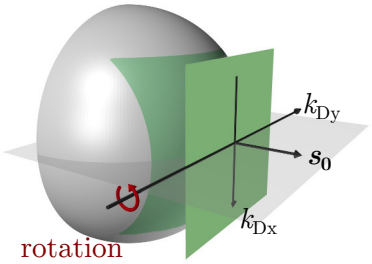

Figure 3.7, Fourier diffraction theorem in 3D. The data $\widehat{U}_{\mathrm{B},\phi_0}(\mathbf{k_D})$ (green) are projected onto a semi-sphere in Fourier space according to ${k_{\mathrm{m}}}^2 = k_{\mathrm{Dx}}^2 + k_{\mathrm{Dy}}^2 + k_{\mathrm{Dz}}^2$. The radius of the sphere is k_{m}. The surface of the sphere is oriented along the direction of propagation $\mathbf{s}_0$ of the incident plane wave $u_0(\mathbf{r})$. This figure was previously published in [Mül+15d].

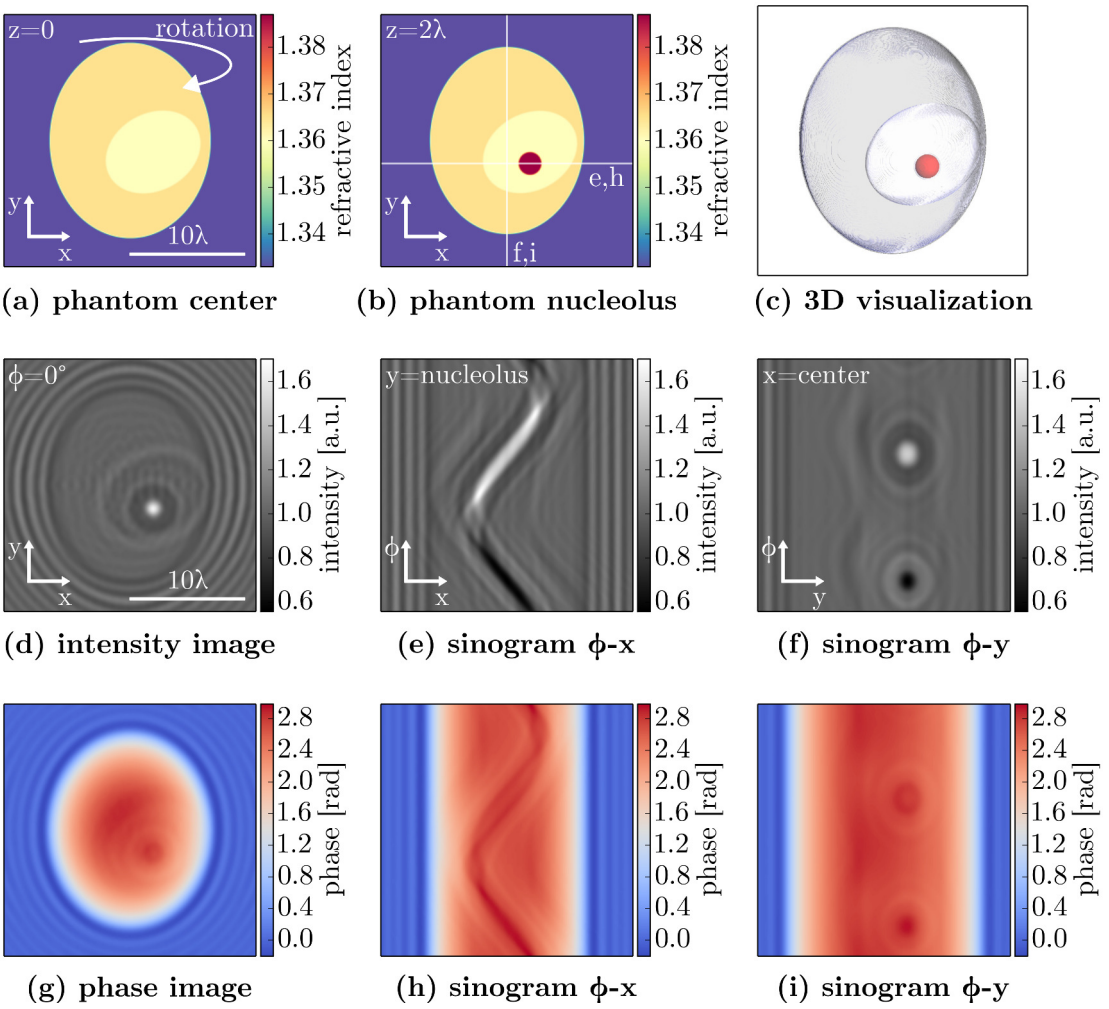

Figure 3.8, 3D sinogram from FDTD simulations. **a)** Cross sections of the cell phantom at the center. **b)** Cross section through the nucleolus at $z = 2\lambda$. The white lines indicate the slice positions of the sinograms in e,f,h, and i. **c)** 3D representation of the cell phantom. **d-f)** Slices through the sinogram: (d) shows one intensity image of the sinogram and (e,f) each show a slice through the sinogram parallel to the acquisition angle ϕ_0. **g-i)** Corresponding phase images of the sinogram. The sinogram was recorded using $N_\mathrm{A} = 200$ equidistant angles. Each finite-difference time-domain (FDTD) simulation ran for 15 000 time steps with a resolution of 13 px/λ. To improve the reconstruction quality, the entire sinogram was numerically autofocused (discussed in section 3.3.2).

Here, in contrast to the actual experiment (see sec. 4), the original RI distribution is known. To quantify the quality of the reconstruction, I compared the RI values with the original values of the cell phantom. For the comparison, I used two different error norms, the root mean square (RMS) error and the total variation (TV) error [Mül+15b]:

$$\mathrm{E_{RMS}} = \sqrt{\frac{\sum_{\mathrm{vol}} \left(n_{\mathrm{ph}}(\mathbf{r}) - n_{\mathrm{rec}}(\mathbf{r})\right)^2}{\sum_{\mathrm{vol}} \left(n_{\mathrm{ph}}(\mathbf{r}) - 1\right)^2}} \tag{3.10}$$

$$\mathrm{E_{TV}} = \sqrt{\frac{\sum_{\mathrm{vol}} \left(\mathrm{TV}^{N\mathrm{D}}_{\mathrm{avg}}(n_{\mathrm{ph}}(\mathbf{r}) - n_{\mathrm{rec}}(\mathbf{r}))\right)}{\sum_{\mathrm{vol}} \left(n_{\mathrm{ph}}(\mathbf{r}) - 1\right)^2}} \tag{3.11}$$

where $\sum_{\mathrm{vol}}$ is the sum over all pixels/voxels of the reconstruction volume, n_{ph} is the RI of the cell phantom, n_{rec} is the RI of the reconstruction, and $\mathrm{TV}^{N\mathrm{D}}_{\mathrm{avg}}$ is the average TV norm in N dimensions ($N = 2, 3$)

$$\mathrm{TV}^{2\mathrm{D}}_{\mathrm{avg}}(n(\mathbf{r})) = \frac{1}{2}\left[|\partial_x n(\mathbf{r})| + |\partial_z n(\mathbf{r})|\right] \tag{3.12}$$

$$\mathrm{TV}^{3\mathrm{D}}_{\mathrm{avg}}(n(\mathbf{r})) = \frac{1}{3}\left[|\partial_x n(\mathbf{r})| + |\partial_y n(\mathbf{r})| + |\partial_z n(\mathbf{r})|\right]. \tag{3.13}$$

The RMS error quantifies how the absolute values of the reconstructed RI deviate from the correct values. In contrast, the TV error quantifies the difference in the gradient (∂_x, ∂_y, and ∂_z) of the RI and is thus suited to describe the blurring in the reconstruction that is observed, for instance, with the backprojection algorithm (see figure 3.6b). Using these error norms, it is possible to quantitatively assess the reconstruction quality of the backprojection algorithm (Radon) and the backpropagation algorithm (Born, Rytov) in 2D and in 3D. The result is summarized in figure 3.9. For low RI differences between the cell phantom and the medium, the Born and Rytov approximations achieve the same reconstruction quality that is better when compared to the Radon transform. It is worth noting that the Born approximation has a lower TV error than the Radon transform in all cases, which means that the Born approximation is better at reconstructing boundaries. On the other hand, the Radon transform has a lower RMS error than the Born approximation, which is not surprising given the preceding discussions (e.g. figure 3.6). However, in both cases the Rytov approximation has the lowest TV and RMS errors. In addition, the Rytov approximation is valid for a large range of RI values, including those commonly observed for cells, which makes it the preferable choice for ODT.

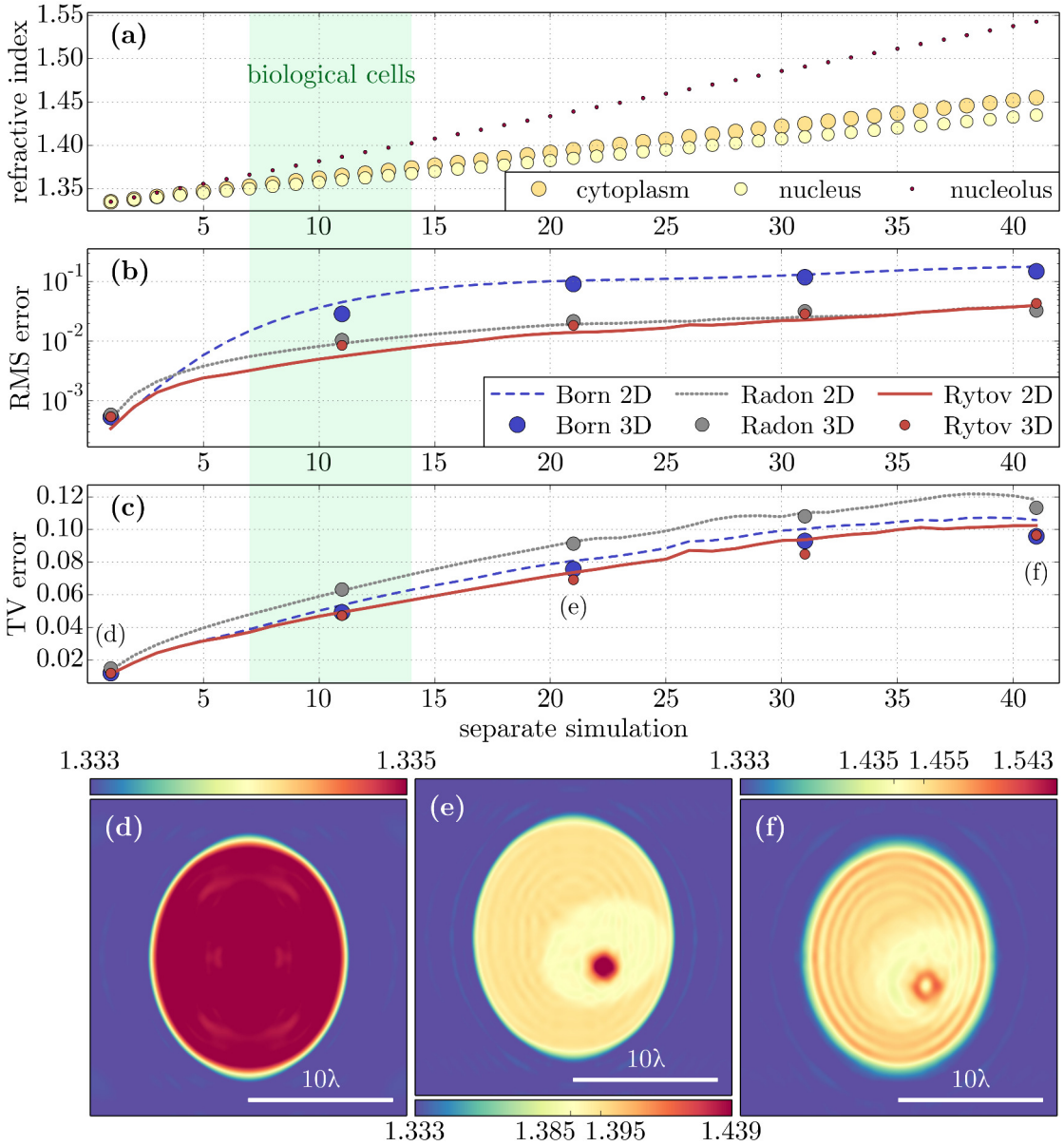

Figure 3.9, Applicability of diffraction tomography for single cells. For different refractive indices (RIs) of the cell phantom, the reconstruction quality of the inverse Radon transform, the Born approximation, and the Rytov approximation are compared. **a)** For each simulation (horizontal axis), the RI values of the cell phantom increase from 1.334 to 1.455 (cytoplasm), 1.435 (nucleus), and 1.543 (nucleolus) in a linear fashion. RI values that are similar to those of cells are highlighted in green [Cho+12]. **b)** The root mean square (RMS) error (eq. 3.10) in dependence of the RI values in (a). **c)** The total variation (TV) error (eq. 3.11) in dependence of the RI values in (a). **d,e,f)** Cross sections of the 3D RI reconstruction with the Rytov approximation. The three simulations are labeled in (c). The RI values displayed in each colorbar range from medium (lowest) to nucleus, cytoplasm, and nucleolus (highest). The diameter (largest extent 17λ) of the cell phantom and the total number of projections ($N_\mathrm{A} = 200$) are unchanged for all simulations. These data have been previously published in [Mül+15b].

3.3 Reconstruction artifacts

In practice, the inversion process of diffraction tomography is afflicted with artifacts. This section addresses several issues that are important to consider for the computational and experimental implementation of diffraction tomography.

3.3.1 Amplitude data

The RI reconstruction presented in the previous section was computed using both amplitude and phase information of the scattered wave $u_{\mathrm{B}}(\mathbf{r})$. The phase information, which quantifies the optical thickness of the sample, is critical for the reconstruction of the RI. The amplitude information, which is sometimes not accessible due to experimental restrictions, does not quantify optical thickness. This raises the question of how the absence of the amplitude information influences the reconstruction quality. Figure 3.10 shows a comparison between a reconstruction with and without the amplitude information for the 3D cell phantom discussed above. The absolute RI value of the nucleolus 1.387 is not correctly reproduced if the amplitude information of the sinogram (figures 3.8d-f) is set to unity during reconstruction. Furthermore, it is important to note that the use of incorrect amplitude data $|u_{\mathrm{B}}(\mathbf{r})|$ directly translates to a scaling of the scattering potential $f(\mathbf{r})$, which affects the reconstructed RI $n(\mathbf{r})$ through equation 2.12. In practice, it is thus very important to correctly normalize the amplitude image with background data. Experimental implementations that do not allow the measurement of the amplitude data, but only the phase data, lead to error-prone reconstructions in diffraction tomography.

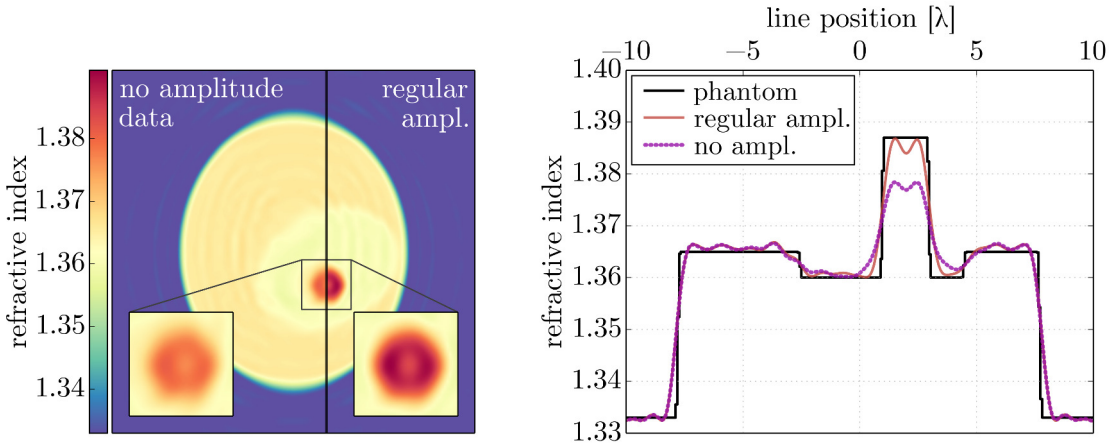

(a) cross section **(b) line plots**

Figure 3.10, Missing amplitude information distorts the reconstruction. a) The cross section shows the reconstruction without the amplitude information in the sinogram (left) and a reference that was computed using the full complex sinogram displayed in figure 3.8 (right). **b)** The line plot through the nucleolus (black vertical line on the left) shows that the reconstruction without the amplitude information does not correctly reproduce the cell phantom.

3.3.2 Numerical focusing

The backpropagation algorithm (eq. 3.8) has the parameter l_D, which is the distance from the center of rotation to the detector plane in a tomographic setup. In practice, the detector plane is a conjugate image plane to the plane defined by the focal position of the microscope. Thus, if the focal position of a microscope coincides with the center of rotation, then $l_\mathrm{D} = 0$. In cases where the focal plane and the rotational axis do not overlap, previous studies have shown that the reconstruction quality can be improved by numerically autofocusing the recorded sinogram prior to the reconstruction [Kos+14; Wu+14]. In addition, even if the correct focal position is known and used in combination with the Rytov approximation, the reconstruction nevertheless becomes blurry (see fig. 3.11). This can be understood by noting that the backpropagation algorithm is derived for the Born approximation and the Rytov approximation is just inserted into the backpropagation formula. Thus, for the Rytov approximation, a numerical focusing step $\exp(-ik_\mathrm{m}(M-1)l_\mathrm{D})$ *during* backpropagation is different than a numerical focusing step *prior to* backpropagation [Wed+95].

To find the focal position for numerical and experimental data, I implemented a numerical autofocusing algorithm that minimizes the gradient norm of the amplitude image (see ap. B.4). Note that the determination of the focus with the gradient norm might not be correct and therefore, should be checked for plausibility. In summary, diffraction tomography in combination with the Rytov approximation should always involve a numerical autofocusing step prior to backpropagation.

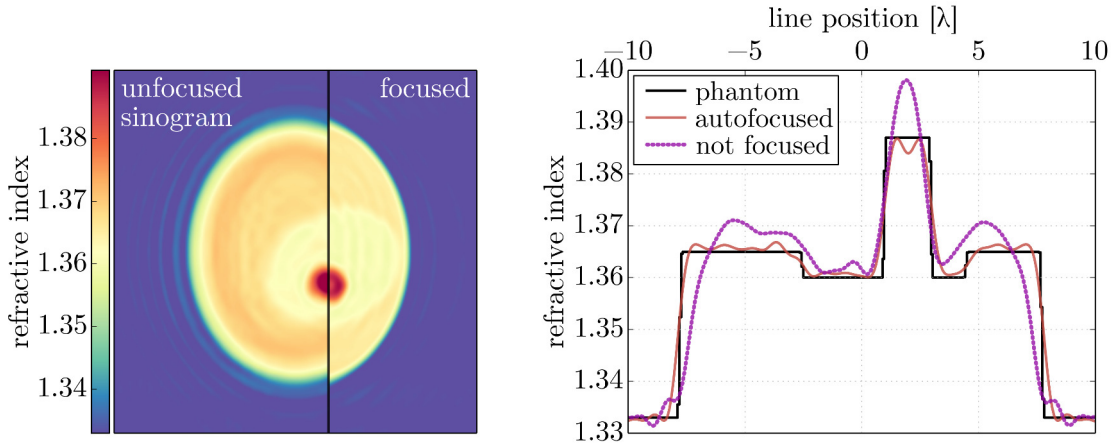

(a) cross section **(b) line plots**

Figure 3.11, Numerical refocusing is essential for diffraction tomography. **a)** The cross section shows the positive effect of numerical focusing prior to backpropagation with the Rytov approximation. **b)** The line plots (black vertical line on the left) show that if the focusing distance l_D is used in the backpropagation algorithm with the Rytov approximation, the reconstruction overshoots dramatically and cannot reproduce RI boundaries correctly.

3.3.3 Angular resolution

Angular resolution, which defines the number of images a sinogram is composed of, affects the reconstruction quality. In a previous publication, we could show that the RMS and TV errors reach a minimum that depends on the number of projections that are used for a reconstruction [Mül+15b]. We showed that reconstruction artifacts that are caused by insufficient angular resolution can be avoided when the reconstruction is performed with at least 160 projections for a cell with a diameter of about 17λ. Lower angular resolution introduces noise, as shown in figure 3.12.

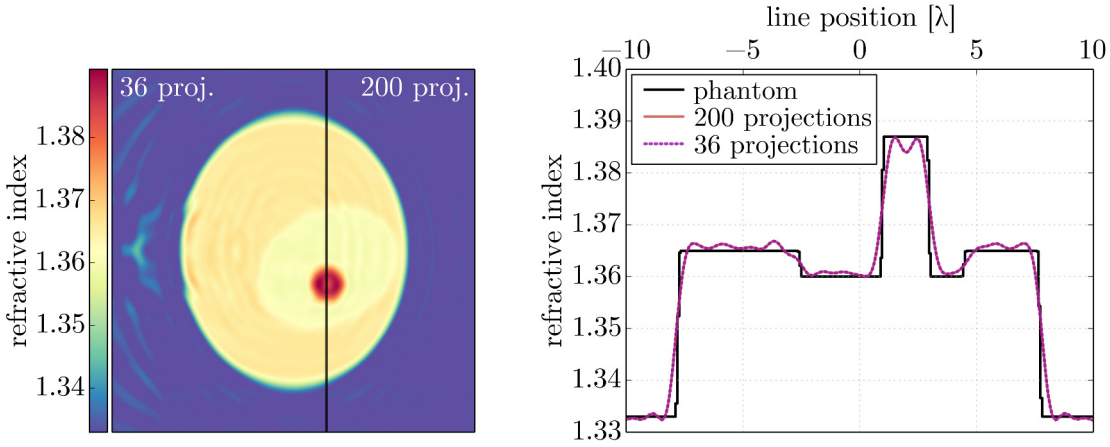

(a) cross section **(b) line plots**

Figure 3.12, Low angular resolution introduces noise. If the number of projections used for a reconstruction is low, the reconstruction will exhibit artifacts. **a)** In the extreme case of only 36 projections, deformations become visible in the cross section. **b)** However, the line plot at the nucleolus shows that the absolute value of the RI can be correctly reconstructed, depending on the region of the reconstruction.

3.3.4 Uneven angular sampling

The backpropagation algorithm shown in equation 3.8 assumes that the acquired projections are recorded from equidistant angles with an angular spacing of $\Delta\phi_0$. If the angles are sampled unevenly but not considered during reconstruction, then artifacts appear. This is a well-known problem in tomographic imaging and can be resolved by introducing weights that reflect the angular coverage of each projection [Tam+81]

$$\Delta\phi_0 \longmapsto \Delta\phi_j = \frac{\phi_{j+1} - \phi_{j-1}}{2}. \tag{3.14}$$

Figure 3.13 illustrates the quality improvement when using weights in the backpropagation process. Note that for full-view tomography, the angular coverage must be at least 180 degrees (half a rotation of the cell). In few-view tomography, projections from an angular range of more than 180 degrees are missing and thus,

the reconstruction exhibits more severe artifacts than those shown in figure 3.13. Few-view artifacts can be addressed with regularization such as total variation minimization already proposed for computerized tomography [LaR+08].

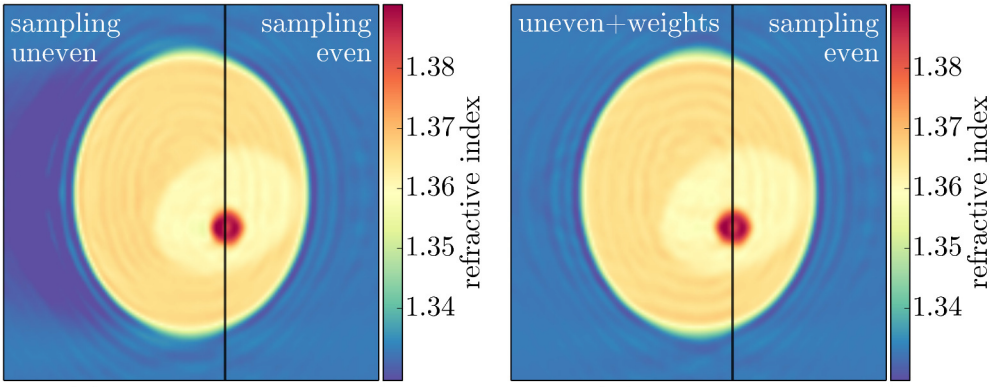

(a) without weights **(b) with weights**

Figure 3.13, Angular weighting improves the reconstruction quality. Each reconstruction was performed using 90 projections. The reconstruction shown on the right in each image shows the reference reconstruction with even angular sampling. **a)** If the sinogram is composed of images that are taken at irregular angular positions, then the reconstruction may contain serious artifacts (e.g. RI values below that of water). **b)** Angular weighting according to equation 3.14 prevents these artifacts.

3.3.5 Directional blurring

Tomographic reconstruction in diffraction tomography with a rotation about a fixed axis is not able to fully reconstruct a 3D object. The Fourier slice theorem and the Fourier diffraction theorem in 2D allow to fill the Fourier space of the imaged object homogeneously with a 360 degree rotation. However, in 3D this is not the case if the sample is rotated about only one axis. If the semi-spherical surface in figure 3.7 is rotated about the k_{Dy}-axis, then frequencies that are located about the k_{Dy}-axis are not available in the reconstruction. This missing apple core in Fourier space leads to directional blurring along the y-axis in the reconstruction [Ver+09; Kou+09]. The effect of this directional blurring is shown in figure 3.14. In principle, this problem can be solved by rotating the sample about two different axes and combining the two complementary reconstructions in Fourier space.

Is it possible to obtain a full 3D coverage without two separate rotations? Technically, this is possible. The backpropagation algorithm requires a one-dimensional representation of all rotational positions. One possibility is to rotate the sample along a spiral from pole to pole. However, it is difficult to implement such a sophisticated rotational control for single cells and therefore, it is unlikely to be

applied in practice. However, investigating the theoretical domain of modified reconstruction algorithms yields new insights. An example that discusses a tilted axis of rotation is given in the next section. Nevertheless, addressing the problem of an arbitrarily rotating cell with a more general version of the backpropagation algorithm is beyond the scope of this theses and may be investigated in future studies.

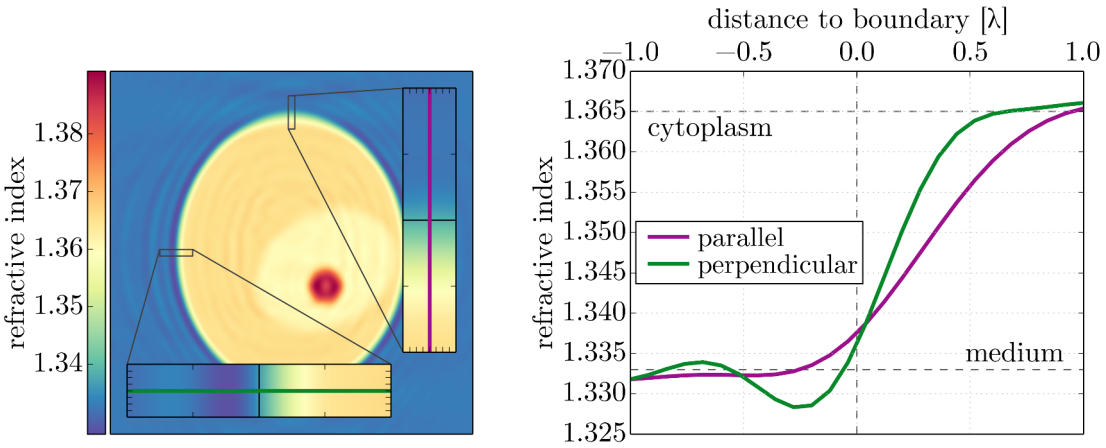

(a) cross section **(b) line plots**

Figure 3.14, Rotation about a single axis introduces directional blurring. **a)** The chosen color map covers the full range of the reconstruction RI values. **b)** The line plots indicated in (a) show a blurring effect parallel to the rotational axis compared to perpendicular to the rotational axis. The reason for that are missing Fourier coefficients along the rotational axis, the so-called missing apple core [Ver+09].

3.3.6 Tilted axis of rotation

In the experimental setup that I will discuss in the next chapter, the imaged cell does not always rotate about a fixed axis. If the rotational axis is tilted in the image plane (laterally), then a simple coordinate transform will make the data compatible to the described backpropagation algorithm. However, if the rotational axis is tilted perpendicular to the image plane (axially), then a successful reconstruction is not always guaranteed. For instance, if the rotational axis is axially tilted by $\theta_{\mathrm{tilt}} = 90°$ with respect to the image plane, then the sinogram consists of only one image of the cell that rotates in the detector plane and tomographic reconstruction is impossible. The transition from good data quality ($\theta_{\mathrm{tilt}} = 0°$) to purely impossible reconstruction ($\theta_{\mathrm{tilt}} = 90°$) is continuous. The amount of data in Fourier space is reduced from a sphere with a missing apple core (see sec. 3.3.5) to a single semi-spherical surface as θ_{tilt} approaches 90°. To allow a reconstruction

for small tilt angles θ_{tilt}, a different backpropagation algorithm is required

$$f(x,y,z) = -\frac{ik_{\text{m}}}{\sqrt{2\pi}} \sum_{j=1}^{N_{\text{A}}} \Delta\phi_0 D^{\text{tilt}}_{-\phi_j} \Bigg\{ \text{FFT}^{-1}_{\text{2D}} \Bigg\{ |k_{\text{Dx}} \cdot \cos\theta_{\text{tilt}}| \cdot e^{ik_{\text{m}}(M-1)\left[z_{\phi_j} - l_{\text{D}}\right]} \cdot \text{FFT}_{\text{2D}} \left\{ \frac{u_{\text{B},\phi_j}(x_{\text{D}}, y_{\text{D}})}{u_0(l_{\text{D}})} \right\} \Bigg\} \Bigg\}. \tag{3.15}$$

The modified backpropagation algorithm in equation 3.15 can be derived analogous to the backpropagation algorithm in equation 3.9. The rotational angles for backpropagation are not anymore distributed on the equator of the unit sphere. Instead, the angles are distributed on a circular path of constant latitude θ_{tilt}. These new rotational positions are defined by the rotation operator $D^{\text{tilt}}_{-\phi_j}$. Furthermore, the filter in Fourier space now contains an additional factor $\cos\theta_{\text{tilt}}$. For single-cell tomography, we could show that this modified algorithm noticeably improves the quality of the reconstruction [Mül+15c].

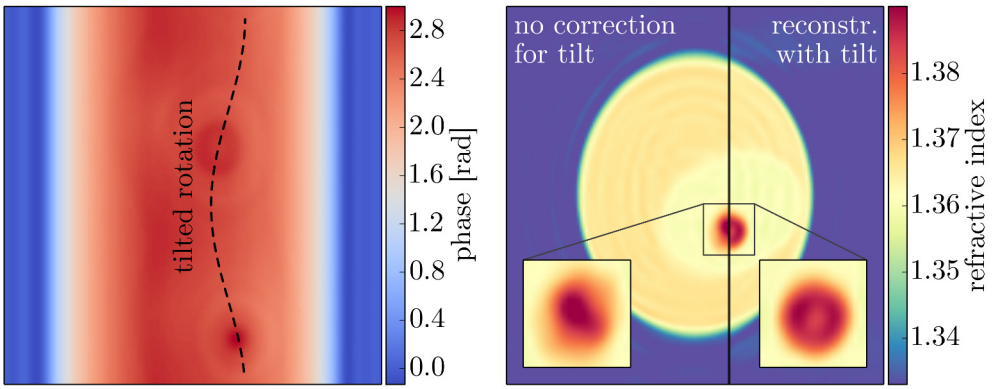

(a) sinogram ϕ-y **(b) cross section**

Figure 3.15, A tilted axis of rotation requires a modified reconstruction algorithm. a) The axial tilt of 0.2 rad (11.5°) is visualized in the sinogram of the finite-difference time-domain (FDTD) simulation with a black sine curve (compare to figure 3.8f). **b)** The reconstruction with the algorithm that does not take into account the tilt correction (eq. 3.9) causes blurring artifacts visible at the nucleolus (left inset). The algorithm that does take into account the tilted axis of rotation (eq. 3.15) improves the quality of the reconstruction (right inset).

4. Single-cell tomography

The objective of optical diffraction tomography (ODT) for single cells is to obtain a quantitative RI map in 3D with sub-cellular resolution. All ODT techniques require a combination of quantitative phase-imaging and some means to acquire phase images from multiple angles. Quantitative phase-imaging techniques originally evolved from phase contrast microscopy [Zer42a; Zer42b]. Then in 1948, Gabor introduced holographic imaging [Gab48], which, with the development of digital camera sensors, allowed the development of digital holographic microscopy (DHM). To acquire phase images from multiple angles, several experimental geometries have been proposed. For instance, the illumination beam in a microscope with a high numerical aperture objective can be tilted up to $\pm 70°$, effectively scanning the cell [Cho+07; Isi+11; Sun+09]. A similar approach is synthetic aperture tomography, which in addition allows to image suspended cells [Lue+08; Sun+14]. Both of these techniques are subject to few-view artifacts, because the angular coverage, limited by the illumination objective, does typically not exceed 140°. To address few-view artifacts, these reconstruction techniques require regularization methods that infer additional information during the reconstruction process [Tam+81; LaR+08]. Another approach to this problem is to use multiple imaging wavelengths. According to the Fourier diffraction theorem (see sec. 3.1.2), multiple illumination wavelengths improve the reconstruction quality, because multiple semi-spherical surfaces with different radii k_m increase the coverage in Fourier space [Hos+15]. Nevertheless, a full angular coverage can only be achieved when the detector or the sample is allowed to rotate by at least 180°. For instance, a *full view* coverage can be achieved by embedding the cell in a gel and rotating it relative to the microscope [Cha+06; Kuj+14; Kos+14; Kos+15] or by rotating the microscope relative to the sample chamber [Lin+14]. However, none of these techniques permit tomographic imaging of suspended cells in a microfluidic environment with a full angular coverage.

In principle, full angular coverage in a microfluidic environment is achievable with optical methods, for instance by all-optical cell rotation [Kre+08; Kre+14], by holographic tweezers [Hab+15], or by optofluidic rotation [Kol+14]. In this work, the optofluidic approach is used, because of its comparatively simple setup. Quantitative phase images are recorded with a commercial camera [Mou+06] (see sec. 4.1). The HL60/S4 cells were prepared according to appendix C. The proposed setup comes with the issue of irregular rotation of the cells, which is addressed computationally (see sec. 4.2). With the presented approach, the proposed setup is suitable to quantify the 3D RI of a cell and to describe its intracellular structure.

4.1 Devices and assembly

The tomographic imaging setup is composed of an inverted microscope (Axiovert 200M, Zeiss, Oberkochen, Germany), a microfluidic channel with an optical trap (sec. 4.1.1), and a quantitative phase-imaging camera (sec. 4.1.2). The used objective is a Plan-Apochromat (40×/0.95 Corr M27, WD0.25, Zeiss). The arrangement is outlined in figure 4.1. In this setup, the image plane and the object plane are conjugate optical planes. In theory, this results in a distance between rotational axis and detector plane of $l_D = 0$. In practice, the planes do not always match and a numerical focusing step is required, as previously discussed in section 3.3.2.

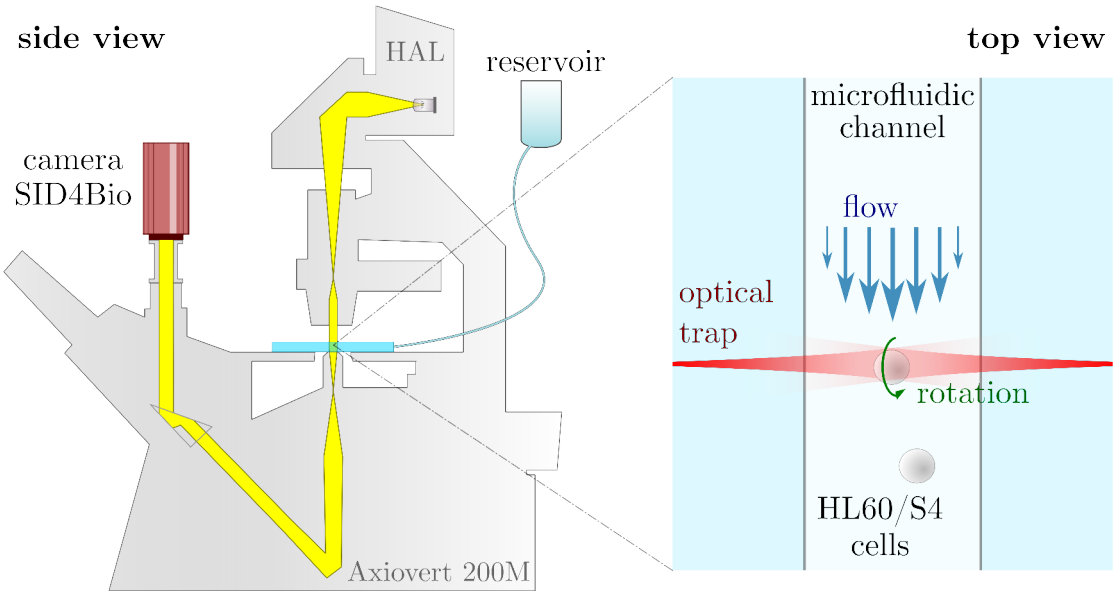

Figure 4.1, Schematic: tomographic imaging setup. The setup is composed of an inverted microscope, a dual-beam laser trap in a microfluidic chip, and a quantitative phase-imaging camera. The left side shows a sketch of the optical beam path (Köhler illumination) of a white-light source (Halogen lamp) within the microscope. The microfluidic chip is connected to a reservoir containing human myelocytic leukemia cells (HL60/S4). The right side shows a close-up of the microfluidic chip. A single cell is trapped by two counter-propagating laser beams and starts to rotate when flow is introduced.

4.1.1 Optofluidic cell rotator

The optofluidic cell rotator combines optical forces to trap and microfluidic forces to rotate single cells. The cells are trapped in a dual-beam laser trap, which is built using two optical fibers that are located on opposing sides of a microfluidic channel. Laser light that is coupled into these fibers results in two counter-propagating laser beams that generate optical forces, moving the cell to the center of the channel (see fig. 4.1). The optical trap used in this work is an optical stretcher [Guc+05; Lin+07] operated at low laser powers and was built for the mechanical

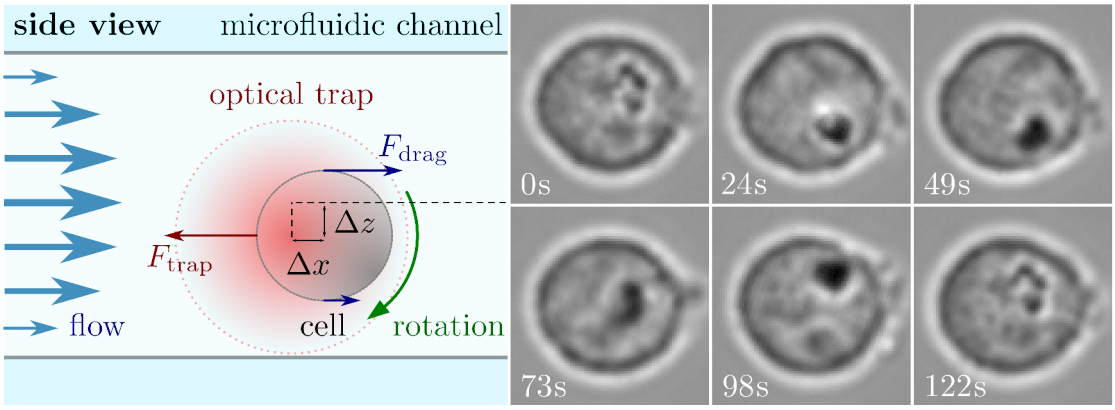

Figure 4.2, Optofluidic cell rotation. The sketch on the left shows the geometry of the optofluidic cell rotator perpendicular to the imaging axis (comp. fig. 4.1). The optical trap, indicated in red, is located a distance Δz away from the center of the microfluidic channel. Thus, if flow is introduced into the channel, the drag forces F_{drag} (blue) at the top and at the bottom of the cell (gray) have different magnitudes. The sum of the drag forces and the trapping force F_{trap} results in a displacement Δx with respect to the center of the trap and introduces a torque which causes the cell to rotate (indicated in green) [Kol+14]. The intensity images on the right side showcase one revolution of a human myelocytic leukemia cell (HL60/S4) within a time interval of two minutes.

characterization of single cells by Chii Jou Chan and Andrew Ekpenyong (e.g. [Cha+15]). To rotate cells, flow is introduced into the channel. The optical trap is located in the lower half of the channel and thus, due to higher flow speeds at the center of the channel, the cell experiences a torque and starts to rotate. Figure 4.2 describes the different forces that act on the cell and shows a 360° rotation of an HL60/S4 cell in the optofluidic cell rotator. Chii Jou Chan and I conducted the presented measurements. The combination of optical trapping and microfluidics for tomographic imaging was first presented by Kolb et al., who used a similar device to perform single-cell fluorescence tomography [Kol+14]. The optofluidic cell rotator, in combination with a commercial microscope, facilitates tomographic imaging of single cells.

Even though optofluidic cell rotation is promising for single-cell tomography, it is inaccurate in two ways. First, the optical trap is not completely stable. The microfluidic flow makes the cell move and rotate slightly in all directions. For instance, comparing the intensity images in figure 4.2 before (0 s) and after (122 s) one revolution reveals a slight tilt. Second, the angle of rotation for each image, which depends on the flow speed and the frame rate of the camera, is not known during the measurement. These issues can be addressed with image pre-processing and image analysis, which are discussed in section 4.2.

4.1.2 Quantitative phase-imaging camera

To reconstruct the RI of single cells, ODT requires quantitative phase-imaging techniques. Typically, quantitative phase-imaging is achieved with interference-based techniques such as DHM, which extract the phase from an interference pattern generated by an object and a reference beam [Sch+15]. In this work however, phase images are obtained with a commercially available phase-imaging camera (SID4Bio, Phasics, Saint Aubin, France). The imaging principle of this camera, quadriwave lateral-shearing interferometry [Mou+06], is similar to that of a Shack-Hartmann wavefront sensor [Cha05]: a diffraction grating is put directly in front of a camera, generating a pattern of diffraction spots on the camera sensor (see inset in figure 4.3). The lateral position of each diffraction spot is dependent on the tilt of the wavefront that hit the diffraction grating at that particular point. Thus, each diffraction spot contains information on the *gradient* of the phase from which the full phase can be computed in a post-processing step. Such a phase-imaging camera has advantages over DHM: reduced complexity, easy combination with commercially available microscopes, high phase accuracy[1] ($\sim 0.07°$ or 1.22×10^{-3} rad), and no dependence on the light source (e.g. no coherent light is required). The drawback of this particular camera is the limited frame

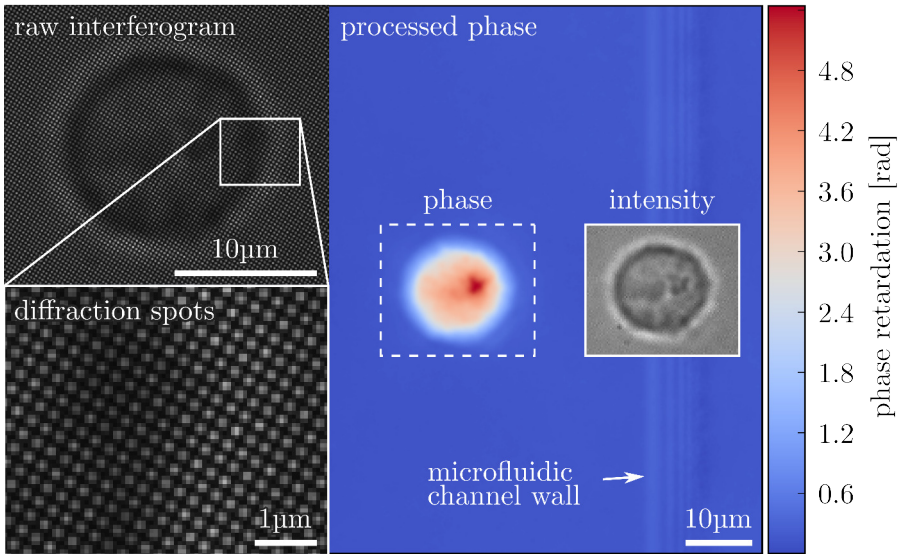

Figure 4.3, Quantitative phase-imaging. The left side shows a section of a raw interferogram of a human myelocytic leukemia cell (HL60/S4), which is recorded with the SID4Bio camera in the "Camera Acquisition Scheduling" mode. The magnification of the interferogram shows the diffraction spots from which the phase is computed (see text). The right side shows the processed phase obtained with the proprietary software SID4Bio. The inset shows the corresponding intensity image, which is not automatically background corrected (see text).

[1] Here, phase accuracy is defined as the standard deviation of a background-corrected blank phase image.

rate ($\sim 8\,\mathrm{fps}$). The resolution of the camera is 1600×1200 pixels, which translates to an effective resolution of 400×300 pixels, because an area of 4×4 pixels is required to determine the displacement of each diffraction spot that was generated by the grating. This results in a relatively large effective physical pixel size of $29.6\,\mu\mathrm{m}$. To address these issues, the manufacturer recently brought forward a phase-imaging camera with a higher frame rate ($\sim 100\,\mathrm{fps}$) and a higher effective resolution $(853 \times 720\ \mathrm{px})^2$. Note that DHM also suffers from a reduced effective resolution, because of a low-pass filtering step in Fourier space that is necessary to separate the object wave from the central band. In summary, the SID4Bio is a convenient tool that is suitable for the quantitative phase-imaging of biological cells [Bon+09; Akn+15].

The sinogram acquisition process using the SID4Bio phase-imaging camera is divided into three steps. First, the raw images are recorded using the "Camera Acquisition Scheduling" functionality of the proprietary software SID4Bio (version 2.2.0.45) that is shipped with the camera. Second, in a post processing step, the raw data images are converted to phase and intensity data with the same software. This post-processing step is computationally demanding and therefore cannot be done live during imaging. To obtain accurate phase data, the software allows to perform a background correction with a reference image recorded prior to the actual image acquisition. However, the intensity data are not background corrected with that reference image. Therefore, in a third step, an additional background image must be recorded prior to and/or after acquiring the raw sinogram data. This step is crucial, because the background-corrected intensity information is important for diffraction tomography (see sec. 3.3.1). The image analysis, including the background correction, of the obtained phase and intensity data are discussed in the next section.

[2]personal communication with Arnaud Rehel, Phasics S.A., France

4.2 Image pre-processing

The phase and intensity images from the SID4Bio camera require several pre-processing steps before the actual RI reconstruction with the backpropagation algorithm. The data need to be background-corrected and focused, the lateral position of the cell in each image must be determined, and the rotational angle of the cell in each frame must be identified. I addressed these issues with self-written Python scripts that are summarized in appendix B.

4.2.1 Local field corrections

In an initial step, the region of interest that contains the cell must be found (see ap. B.3). To retrieve the complex scattered field of the cell, several correction steps need to be performed. The most important step is the background correction of phase and intensity data. The background-correction of the phase data $\Phi(\mathbf{r_D})$ have three contributions. The reference phase data $\Phi_{\mathrm{BG}}^{\mathrm{ref}}(\mathbf{r_D})$, a linear ramp correction $\Phi_{\mathrm{BG}}^{\mathrm{ramp}}(\mathbf{r_D})$ to correct for a tilt of the incident wave [Sch+15], and a histogram-based background correction $\Phi_{\mathrm{BG}}^{\mathrm{hist}}$. The histogram-based correction uses the mode[3] of the phase data that are outside of the region occupied by the cell to force the average background phase to be approximately centered about $\Phi = 0$. The intensity data $I(\mathbf{r_D})$ are background-corrected by normalizing to the reference intensity data $I_{\mathrm{BG}}^{\mathrm{ref}}(\mathbf{r_D})$. The amplitude data are then obtained by computing the square root of the intensity data. In summary, the complex scattered wave $u_{\mathrm{s}}(\mathbf{r_D})$ is obtained using

$$u_{\mathrm{s}}(\mathbf{r_D}) = \sqrt{\frac{I(\mathbf{r_D})}{I_{\mathrm{BG}}^{\mathrm{ref}}(\mathbf{r_D})}} \cdot e^{i\left[\Phi(\mathbf{r_D}) - \Phi_{\mathrm{BG}}^{\mathrm{ref}}(\mathbf{r_D}) - \Phi_{\mathrm{BG}}^{\mathrm{ramp}}(\mathbf{r_D}) - \Phi_{\mathrm{BG}}^{\mathrm{hist}}\right]}. \tag{4.1}$$

In some cases, the focal plane during imaging does not coincide with the rotational axis. As previously discussed in section 3.3.2, the backpropagation algorithm will be inaccurate unless a numerical focusing step (see ap. B.4) is performed prior to the reconstruction. All individual fields of a sinogram are focused to the same distance by first determining the optimal focusing position for each field and then focusing the entire sinogram to the average of the optimal focus positions. A summary of the field corrections for exemplary data of an HL60/S4 cell is shown in figure 4.4. The field corrections remove image artifacts, which is the basis for the image analysis steps that are discussed in the following sections.

[3] the most common histogram value

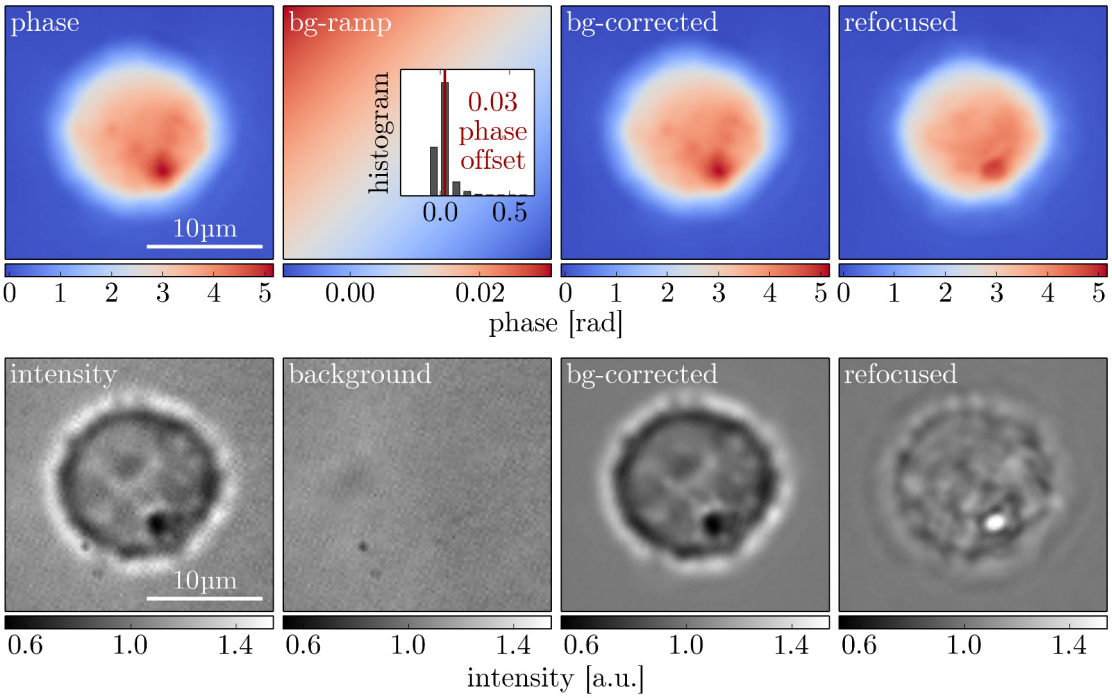

Figure 4.4, Background correction and autofocusing. The top row illustrates the image processing steps for the phase data. The phase data recorded with the SID4Bio camera are already background-corrected with the reference data. In addition, a linear background phase ramp (bg-ramp) and the average background phase are subtracted (see text). The background phase is the mode (red line in the inset histogram plot) of the phase data in the region that do not contain the cell. The linear ramp correction and the histogram correction have no visible impact on the phase image. This is an indicator for a good background correction with the reference phase data. The autofocusing step (focus distance 9.45 µm) generates a phase image with a sharper cell boundary. Note that the seemingly reduced size of the cell can be explained by this sharpening effect. The intensity data are background corrected by dividing by a backgound image. The background-corrected data appear smoother. The numerically autofocused intensity data lose the black-and-white halo around the cell.

4.2.2 Translational image alignment

The optofluidic cell rotator has a design flaw: small perturbations in the flow profile, caused for instance by an asymmetric cell, result in uncontrolled movements of the cell. Therefore, the trapped cell exhibits uncontrolled lateral motion and may rotate arbitrarily during image acquisition. The lateral translational motion can be addressed with image analysis, as discussed in this section. The rotational degrees of freedom are discussed in the next section.

My approach to correct for the lateral movement of the cell involves fitting a circle to the background-corrected, but not numerically autofocused intensity images. These images exhibit a white halo around the cell which is well-suited for the Canny edge detection algorithm [Can86]. To determine the center of the cell, I applied a circle fit to the detected edge, as shown in figure 4.5b. The cell center of each intensity image in the sinogram is thus determined with sub-pixel accuracy and the sinogram can be aligned to the cell center using spline interpolation. As shown in figure 4.5c, the resulting aligned sinogram exhibits less noise along the angular direction than the original data. The sinogram image alignment with this fitting-and-interpolation method is essential for the following step, the determination of the rotational axis.

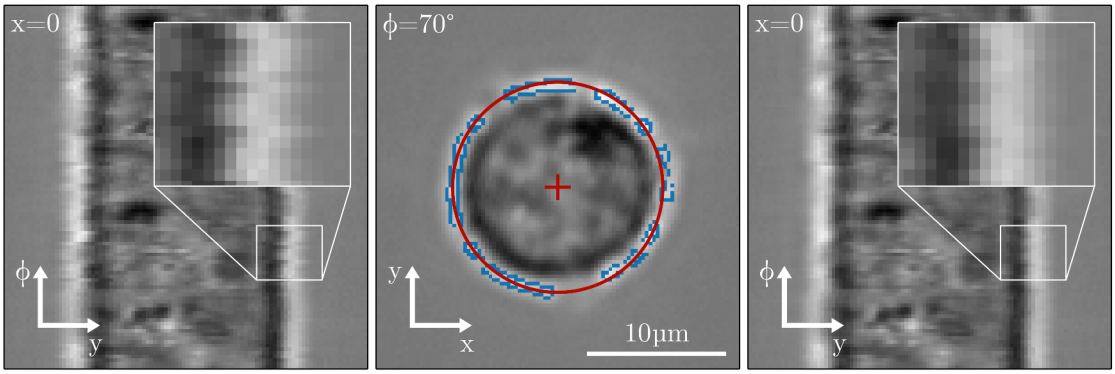

(a) not aligned **(b) sinogram slice** **(c) aligned**

Figure 4.5, Translational sinogram alignment. a) The sinogram of a human myelocytic leukemia cell (HL60/S4) consists of 100 frames that cover an angular range of almost two revolutions (680°). The cell has a region of high refractive index which, due to destructive interference, generates a black diffraction spot in the image plane at the detector. The spot does not change between black and white, because the data are not numerically focused to the center of the rotational axis. The cut at the center of the sinogram shows the black diffraction spot as it passes the x=0-plane of the intensity sinogram. **b)** The center of the cell (red cross) is determined by fitting a circle (red) to the contour (blue) of the white halo in the intensity image. This procedure is performed for every image of the sinogram. **c)** All sinogram images are aligned with respect to the center of the cell using spline interpolation of the order three. The zoomed inset shows a smoother boundary of the cell across the sinogram when compared to (a).

4.2.3 Determination of the rotational axis

In addition to the translational movement of the cell in the optofluidic cell rotator, the trapped cell does not always rotate about a stable axis. This phenomenon seems to be a flaw by design[4] and is difficult to address. However, it is possible to record a full rotation of the cell about an axis that is nearly stable, but is slightly tilted with respect to the image plane. As discussed in section 3.3.6, I have derived and implemented a modified version of the backpropagation algorithm that addresses such an axial tilt. Thus, the challenge here is the determination of the rotational axis and the rotational position for each sinogram image.

The determination of the rotational positions from the complex-valued sinogram is no trivial task. Due to the RI of the cell, the intensity images exhibit black and white diffraction patterns that, for a horizontal rotational axis, move up and/or down at various speeds depending on the 3D structure of the cell. In addition, this indeterminacy is made more complicated by the fact that the rotational axis may be tilted as mentioned above. Kolb et al. [Kol+14] determined the rotational angles by analyzing sections of the sinogram from fluorescence images. However, due to the tilted axis of rotation in the optofluidic cell rotator, this approach cannot be applied here. I approached this problem by tracking a diffraction spot in the sinogram images. Figure 4.6 shows the numerically autofocused images of a cell with a diffraction spot that is generated by a high-refractive-index feature inside the cell. I wrote the Python script `determine_rotation_pt.py` (see ap. B.5), which detects the strongest signal, black or white, in the intensity images and

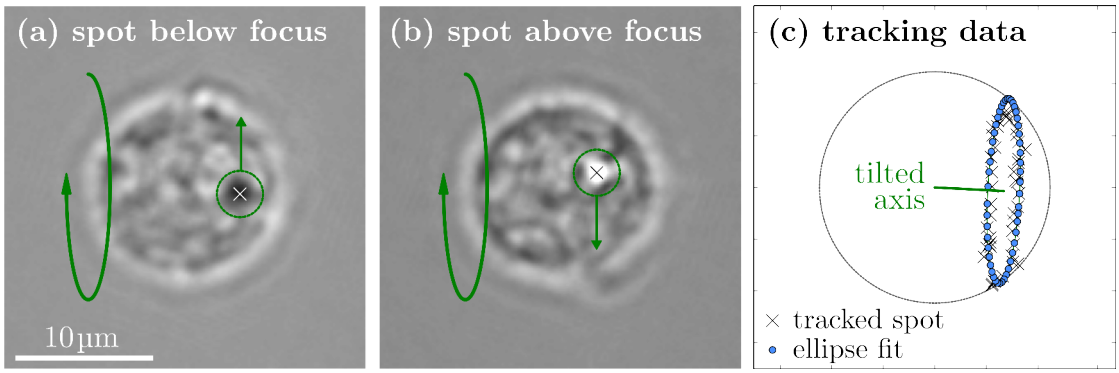

Figure 4.6, Determination of the rotational axis. The aligned and numerically refocused intensity images of an human myelocytic leukemia cell (HL60/S4) are used to determine the rotational position by tracking a diffraction spot. **a)** The diffraction spot is black when it is located in a region of the cell that points away from the observer. **b)** After passing the focal plane, the diffraction spot becomes white and moves in the opposite direction. **c)** An ellipse fit (green) to the the tracked positions (black crosses) allows to determine the rotational axis (green) of the cell. To rotational positions that are used in the backpropagation algorithm are marked as blue circles.

[4]Such instabilities also appear in the supplementary video `jbio_201300196_sm_movie02.mp4` in [Kol+14].

fits an ellipse to the obtained points. To ensure consistency with the model of a rotating sphere, the fit is designed in such a way that the ellipse is the projection of a circle that is located on the surface of the unit sphere onto a plane. The vector from the origin to the center of the ellipse determines the direction of the laterally projected rotational axis. The minor axis of the ellipse determines the axial tilt of the rotational axis. The axial tilt direction is determined by the shade of the diffraction spot. A bright spot indicates that the feature is located on the side of the cell facing the observer. A dark spot indicates that the feature is located in the far side of the cell. In figure 4.6, the dark spots are on the right and the bright spots are on the left part of the ellipse. Therefore, the cell is rotating about an axis whose right end sticks out of the paper plane. The drawbacks of this approach are that the rotational axis is not entirely stable, that the tracked position of the diffraction spot is imprecise, and that the spot is impossible to track when it is located on the perimeter of the cell image. Therefore, the tracked positions are projected onto the fitted ellipse and sinogram images that did not allow tracking are assigned to evenly distributed angular positions. The resulting final rotational position of each sinogram image is projected onto a 3D circle on the unit sphere, as indicated by the blue circles in figure 4.6. The position of the rotational axis and the points on the unit sphere are important parameters for the backpropagation algorithm (eq 3.15). I tested and verified the entire pipeline from phase acquisition to RI reconstruction with a tilted axis of rotation with *in silico* (FDTD) sinograms. The application of the pipeline to experimental data are shown in the next sections.

4.3 Tomographic reconstruction

4.3.1 Reconstruction of a human myelocytic leukemia cell

The pre-processing steps discussed in the previous sections produce all the data required for the backpropagation step described by equation 3.15. The sinogram data of an HL60/S4 cell are background-corrected (eq. 4.1), numerically focused ($l_\mathrm{D} = 0$), and centered (see fig. 4.7a). The rotational position of each sinogram image ϕ_j as well as the axial tilt angle of the rotational axis θ_tilt are obtained by tracking a diffraction spot in the intensity images of the rotating cell. The wavelength used in the algorithm is set to $\lambda = 550\,\mathrm{nm}$, which is approximately the average wavelength of the used halogen lamp. The resolution of the setup is $0.263\,\mu\mathrm{m/px}$. To apply the Rytov approximation, the recorded sinogram data are interpreted as u_R which is transformed to u_B using equation 2.28. The resulting reconstruction with the backpropagation algorithm is shown in figure 4.7b,c. To visualize the sub-cellular structure of the cell, figure 4.7c shows iso-surfaces at different RI values. I manually defined a boundary of the cell at an RI value of 1.349, which is approximately the mean of the cytoplasm and the surrounding medium, as shown in figure 4.8. The volume defined by this iso-surface is $1200\,\mu\mathrm{m}^3$ ($1.2\,\mathrm{pL}$), which corresponds to an effective radius (assuming sphericity) of about $6.60\,\mu\mathrm{m}$. The resulting average RI of the cell computes to 1.359. With a refraction increment of $\alpha \approx 0.2\,\mathrm{mL\,g^{-1}}$ [Bar52; Dav+52], these values imply a dry mass of about $140\,\mathrm{pg}$.

The 3D visualization of the HL60/S4 cell clearly shows a small region of high RI (red) that is responsible for the observed diffraction spot in the image plane. The region appears as a black and a white diffraction spot in the intensity sinogram in figure 4.7a and as a region of high phase retardation in the corresponding phase sinogram. The RI of this small region is above 1.38, which is shown in the quantitative line plots in figure 4.8. Furthermore, the iso-surfaces shown in the cross-sectional image of figure 4.7c uncover regions within the cell that appear to have a lower RI than the average of the cell (black arrow).

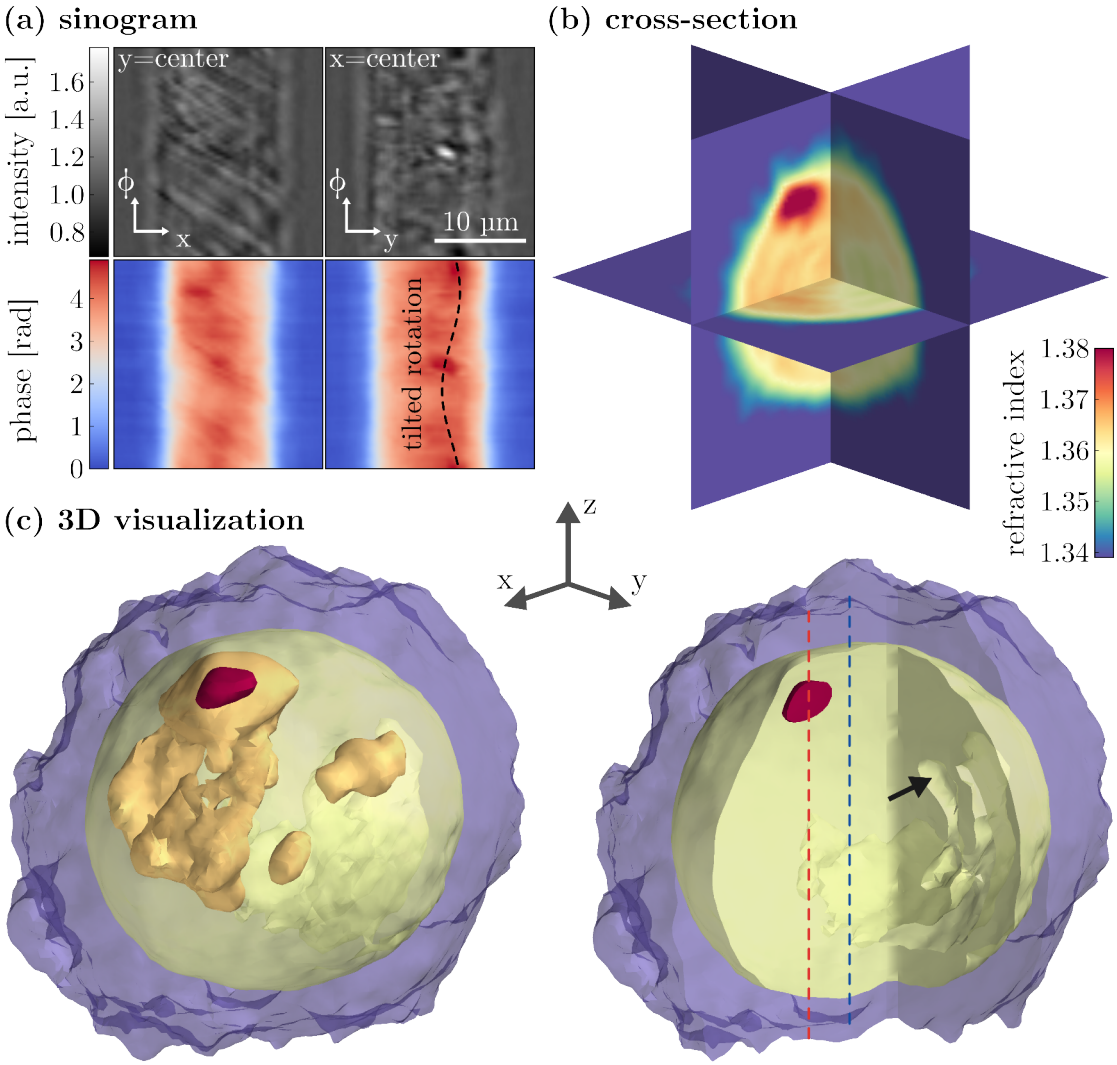

Figure 4.7, Refractive index reconstruction of an HL60/S4 cell. a) The cuts through the center of the phase and intensity sinograms show that there is a tilted axis of roation, highlighted by a dashed sine curve that follows the diffraction spot (see also fig. 3.15). **b)** Cross-sectional images of the reconstructed human myelocytic leukemia cell (HL60/S4). **c)** The visualization in 3D shows the refractive index (RI) iso-surfaces at 1.339 (violet), 1.357 (yellow), 1.363 (orange), and 1.380 (red). The orange iso-surface is not shown in the right plot. In the cross-section of the right plot there are yellow iso-surfaces visible at the inside of the cell, indicating that the cell contains regions with low RI (black arrow). The red and blue dashed lines indicate the position of the line plots shown in figure 4.8.

4.3.2 Accuracy and resolution

It is not possible to verify the quantitative RI reconstruction, because there is no ground truth data of the imaged HL60/S4 cell. However, it is possible to quantify the effect of the imaging noise and to compare the obtained average RI values to the result of other techniques.

With the radius obtained from the 3D reconstruction, I performed a 2D phase analysis following Schürmann et al. [Sch+15] for all 56 sinogram images and found an average RI and a standard deviation of 1.366 ± 0.001. The difference to the average RI of the 3D reconstruction may have multiple causes. First, the 2D phase analysis does not take into account diffraction and assumes that the cell is a homogeneous sphere. In addition, I have observed in Mie simulations that 2D phase analysis over-estimates the average RI by about 0.002 to 0.005 (data not shown). However, the 3D reconstruction clearly shows that the cell is not homogeneous and thus, the computation of the average RI from a weighted 2D phase image is prone to error. The 2D approach does not describe the scattering at a cell as accurate as the backpropagation algorithm does. Second, even though the pre-processing steps give information about the tilted axis of rotation, the exact rotational positions are not known and therefore, the 3D reconstruction may become blurry. This blurring leads to a washed-out boundary between the medium and the cell, artificially lowering the 3D RI. Therefore, due to the unknown magnitudes of the different contributions to deviations from the real value, it remains elusive which average

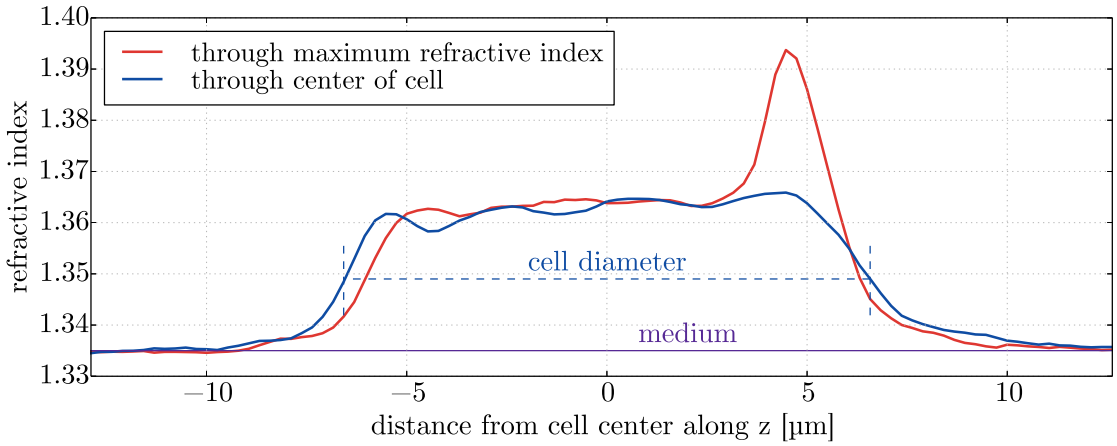

Figure 4.8, Line plots through the reconstruction of an HL60/S4 cell. The position of the line plots through the reconstructed human myelocytic leukemia cell (HL60/S4) are indicated as dashed lines with the same colors in figure 4.7. The red line plot goes through the maximum of the refractive index (RI). The blue line plot follows the z-axis through the center of the reconstrucion. The axial extent of the cell, which is determined by the isosurface with a manually selected RI value of 1.349, is indicated by the blue dashed line (cell diameter). The RI of the surrounding medium (PBS) is $n_\mathrm{m} = 1.335$.

RI value best represents that of the imaged cell.

The phase accuracy of the phase-imaging camera of 0.07° (see sec. 4.1.2) can be translated to a noise in the RI reconstruction by generating empty sinograms that exhibit the same noise level and backpropagating them. The standard deviation of the resulting noise in the RI is less than 5×10^{-4}, which is well below the noise introduced by the low angular sampling. Thus, the phase accuracy of the used camera has no measurable effect on the RI reconstruction.

The resolution of the presented setup could be improved by increasing the magnification of the setup and by moving to shorter illumination wavelengths. Furthermore, for white-light illumination, I had to assume an average wavelength of $\lambda = 550\,\mathrm{nm}$ for the backpropagation algorithm. To improve accuracy, the spectrum could be reduced to a narrow band, allowing a better approximation of the used wavelength. However, the largest contribution to the reconstruction error is probably the inaccurate determination of the rotational position of the cell and the subsequent backpropagation along directions that do not reflect the acquisition direction. To address this problem, an approach more robust than the proposed tracking algorithm is required.

5. Conclusion and outlook

This thesis addressed the refractive index (RI) measurements of single cells in suspension with optical diffraction tomography (ODT). On the theoretical side, I approached the problem by deriving the theory of ODT, implementing the corresponding reconstruction algorithm, and testing the algorithm using ground truth data that I generated using the finite-difference time-domain (FDTD) method. In an experimental part, I could demonstrate ODT with an optofluidic setup, as previously described by Kolb et al. [Kol+14]. My *in silico* studies confirmed that, with surprising accuracy, the Rytov approximation is well-suited for imaging biological cells [Sla+84; Kak+01; Mül+15b] and thereby, I found strong evidence against the notion that the Rytov approximation is equivalent to the inverse Radon transform as proposed by Wedberg et al. [Wed+95]. Furthermore, my work contributes to the advancement of ODT by introducing a novel method to deduce the rotational motion of a cell from the recorded image data and by providing the necessary software to perform the subsequent tomographic reconstruction.

My achievements are of general interest to the ODT community. For instance, prior to my work, an implementation of the 3D backpropagation algorithm was not publicly available. Furthermore, the additional information on data analysis given in my thesis complements the ground work of Kak and Slaney [Kak+01], makes ODT readily-available and simple to use, and places ODT into perspective for single-cell imaging. As a result, my thesis contributes by greatly reducing expenditures for data analysis in upcoming ODT applications.

My work presents a technique that could potentially extend the toolbox of marker-free methods for cancer diagnosis. For instance, it has been shown that the mechanical characterization of human breast epithelial cells allows to tell the difference between normal and cancerous cells [Guc+05]. The physical properties (structure, refractive index, dry mass) that can be measured with the presented ODT setup might yield useful complementary data to improve accuracy or to determine new signatures for other cell types.

There are, nevertheless, also limitations to the presented technique. In the present work, I was not able to achieve identification of cell organelles, because the necessary ground truth data, the positions of cell organelles, were not available. However, expanding the presented setup with fluorescence imaging will allow to colocalize organelles, such as the nucleus, and enable their characterization using RI, volume, or dry mass. With increasing knowledge, these RI signatures could then eventually be used to identify sub-cellular organelles without the necessity

of complementary fluorescence imaging. A current limitation of the presented setup is the low spatial resolution. By increasing the magnification, enhancing the resolution of the detector, or switching to shorter, narrow-banded illumination wavelengths, the reconstruction quality can be greatly improved. However, the largest limitation of the optofluidic setup in its current state is the inaccurate determination of the rotational position of the trapped cell. Further research may be advisable to improve tracking of the cell across the sinogram. One solution could involve an intermediate regularization step using the forward process with the Rytov approximation. In this approach, each sinogram projection is compared to a corresponding projection that is computed from the 3D reconstruction. I believe that an iterative search algorithm could then find the exact angular position for each projection, effectively improving the reconstruction quality step-by-step. However, this kind of approach would be computationally demanding and might only be feasible with the application of graphical processing units (GPUs). To quantify the accuracy of the proposed setup and to strengthen the validity of the backpropagation algorithm, future studies could examine the reconstruction of physical cell phantoms, for instance conglomerates of transparent beads with known RI values.

Optofluidic rotation in combination with ODT has a high potential for single-cell analysis in microfluidic devices, because the experimental setup is robust and easy to use. The marker-free nature of ODT makes it complementary to other imaging methods and provides quantitative, structural data for the discrimination and identification of single cells. To exploit the full potential of the proposed technique, several issues still need to be addressed. My work has isolated, described, and resolved some but not all of these issues, providing insight into and extending the foundation of ODT for single cells.

A. Derivations

We have published the derivations presented in this appendix in a similar form [Mül+15d]. That publication and the text presented in this appendix are both based on the same draft which was written by me.

A.1 The Rytov approximation

The Rytov approximation is well-known in the field of diffraction tomography [Wol69; Sla85; Kak+01]. The simple translation between Born and Rytov approximation shown here is commonly used to simplify data analysis in diffraction tomography.

The equations 2.23 given in section 2.3.3 were

$$\begin{aligned} u(\mathbf{r}) &= \exp(\varphi(\mathbf{r})) \\ u_0(\mathbf{r}) &= \exp(\varphi_0(\mathbf{r})) \\ \varphi(\mathbf{r}) &= \varphi_0(\mathbf{r}) + \varphi_\mathrm{s}(\mathbf{r}) \end{aligned}$$

with the complex Rytov phase defined in equations 2.24

$$\begin{aligned} u(\mathbf{r}) &= u_0(\mathbf{r}) + u_\mathrm{s}(\mathbf{r}) \\ u_\mathrm{s}(\mathbf{r}) &= \exp(\varphi_0(\mathbf{r}))\left[\exp(\varphi_\mathrm{s}(\mathbf{r})) - 1\right]. \end{aligned}$$

Using these relations, the inhomogeneous Helmholtz equation becomes

$$(\nabla^2 + {k_\mathrm{m}}^2) u(\mathbf{r}) = -f(\mathbf{r}) u(\mathbf{r}) \tag{A.1}$$

$$(\nabla^2 + {k_\mathrm{m}}^2) \exp(\varphi(\mathbf{r})) = -f(\mathbf{r}) \exp(\varphi(\mathbf{r})). \tag{A.2}$$

We can now compute $\nabla^2 \exp(\varphi(\mathbf{r}))$

$$\nabla^2 \exp(\varphi(\mathbf{r})) = \nabla\left[\exp(\varphi(\mathbf{r})) \cdot \nabla\varphi(\mathbf{r})\right] \tag{A.3}$$

$$\nabla^2 \exp(\varphi(\mathbf{r})) = \exp(\varphi(\mathbf{r}))\left[\nabla^2\varphi(\mathbf{r}) + (\nabla\varphi(\mathbf{r}))^2\right] \tag{A.4}$$

to obtain a differential equation for $\varphi(\mathbf{r})$.

$$\exp(\varphi(\mathbf{r}))\left[\nabla^2\varphi(\mathbf{r}) + (\nabla\varphi(\mathbf{r}))^2 + {k_\mathrm{m}}^2\right] = -f(\mathbf{r}) \exp(\varphi(\mathbf{r})) \tag{A.5}$$

$$\nabla^2\varphi(\mathbf{r}) + (\nabla\varphi(\mathbf{r}))^2 + {k_\mathrm{m}}^2 = -f(\mathbf{r}) \tag{A.6}$$

Equation A.6 is a non-linear differential equation for the complex phase $\varphi(\mathbf{r})$. In the same manner, a differential equation for $\varphi_0(\mathbf{r})$ can be derived

$$\nabla^2\varphi_0(\mathbf{r}) + (\nabla\varphi_0(\mathbf{r}))^2 + {k_\mathrm{m}}^2 = 0. \tag{A.7}$$

The next step is to insert equation 2.23 and to find a differential equation for $\varphi_\mathrm{s}(\mathbf{r})$.

$$\nabla^2[\underline{\varphi_0(\mathbf{r})} + \varphi_\mathrm{s}(\mathbf{r})] + \underbrace{(\nabla[\varphi_0(\mathbf{r}) + \varphi_\mathrm{s}(\mathbf{r})])^2}_{\underline{(\nabla\varphi_0(\mathbf{r}))^2}+2\nabla\varphi_0(\mathbf{r})\cdot\nabla\varphi_\mathrm{s}(\mathbf{r})+(\nabla\varphi_\mathrm{s}(\mathbf{r}))^2} + \underline{{k_\mathrm{m}}^2} = -f(\mathbf{r}) \tag{A.8}$$

The terms marked with a line compute to zero (eq. A.7) and the equation above becomes

$$\nabla^2\varphi_\mathrm{s}(\mathbf{r}) + 2\nabla\varphi_\mathrm{s}(\mathbf{r})\cdot\nabla\varphi_0(\mathbf{r}) + (\nabla\varphi_\mathrm{s}(\mathbf{r}))^2 = -f(\mathbf{r}). \tag{A.9}$$

It is possible to simplify this expression by considering:

$$\nabla^2 u_0(\mathbf{r})\varphi_\mathrm{s}(\mathbf{r}) = \underbrace{\nabla^2 u_0(\mathbf{r})}_{-{k_\mathrm{m}}^2 u_0(\mathbf{r})}\cdot\varphi_\mathrm{s}(\mathbf{r}) + 2\underbrace{\nabla u_0(\mathbf{r})}_{u_0(\mathbf{r})\nabla\varphi_0(\mathbf{r})}\cdot\nabla\varphi_\mathrm{s}(\mathbf{r}) + u_0(\mathbf{r})\nabla^2\varphi_\mathrm{s}(\mathbf{r}) \tag{A.10}$$

$$\downarrow$$

$$(\nabla^2 + {k_\mathrm{m}}^2)u_0(\mathbf{r})\varphi_\mathrm{s}(\mathbf{r}) = 2u_0(\mathbf{r})\nabla\varphi_0(\mathbf{r})\cdot\nabla\varphi_\mathrm{s}(\mathbf{r}) + u_0(\mathbf{r})\nabla^2\varphi_\mathrm{s}(\mathbf{r}). \tag{A.11}$$

If we multiply equation A.9 by $u_0(\mathbf{r})$ then we can substitute with equation A.11 to obtain

$$(\nabla^2 + {k_\mathrm{m}}^2)u_0(\mathbf{r})\ \underbrace{\varphi_\mathrm{s}(\mathbf{r})}_{\overset{\text{Rytov}}{\approx}\varphi_\mathrm{R}(\mathbf{r})} = -u_0(\mathbf{r})\underbrace{[(\nabla\varphi_\mathrm{s}(\mathbf{r}))^2 + f(\mathbf{r})]}_{\overset{\text{Rytov}}{\approx}f(\mathbf{r})}. \tag{2.25}$$

Thus, the Rytov approximation assumes that the gradient of the Rytov phase $\nabla\varphi_\mathrm{R}(\mathbf{r})$ is small compared to the scattering potential $f(\mathbf{r})$. We can now make use of the Green's function $G(\mathbf{r})$ again (eqns. 2.14) and arrive at the formula for the Rytov phase $\varphi_\mathrm{R}(\mathbf{r})$ [Kak+01]:

$$u_0(\mathbf{r})\varphi_\mathrm{R}(\mathbf{r}) = \int d^3r'\, G(\mathbf{r}-\mathbf{r}')\, f(\mathbf{r}')\, u_0(\mathbf{r}') \tag{A.12}$$

$$\varphi_\mathrm{R}(\mathbf{r}) = \frac{\int d^3r'\, G(\mathbf{r}-\mathbf{r}')\, f(\mathbf{r}')\, u_0(\mathbf{r}')}{u_0(\mathbf{r})} \tag{A.13}$$

By comparing this expression to the Born approximation (eq. 2.19), we find that we can compute the Rytov approximation $u_\mathrm{R}(\mathbf{r})$ from the Born approximation

$u_\mathrm{B}(\mathbf{r})$ and vice versa.

$$\varphi_\mathrm{R}(\mathbf{r}) = \frac{u_\mathrm{B}(\mathbf{r})}{u_0(\mathbf{r})} \tag{A.14}$$

$$u_\mathrm{R}(\mathbf{r}) = u_0(\mathbf{r}) \left[\exp\left(\frac{u_\mathrm{B}(\mathbf{r})}{u_0(\mathbf{r})} \right) - 1 \right] \tag{A.15}$$

$$u_\mathrm{B}(\mathbf{r}) = u_0(\mathbf{r}) \ln\left(\frac{u_\mathrm{R}(\mathbf{r})}{u_0(\mathbf{r})} + 1 \right) \qquad = u_0(\mathbf{r})\varphi_\mathrm{R}(\mathbf{r}) \tag{A.16}$$

$$u(\mathbf{r}) \overset{\text{Born}}{\approx} u_0(\mathbf{r}) + u_\mathrm{B}(\mathbf{r})$$

$$u(\mathbf{r}) \overset{\text{Rytov}}{\approx} u_0(\mathbf{r}) + u_\mathrm{R}(\mathbf{r})$$

This simple translation between Born and Rytov approximation allows the application of the Rytov approximation in tomographic algorithms derived for the Born approximation, a fact that is exploited in diffraction tomography.

Validity of the Rytov approximation

This section attempts to make a statement regarding the validity of the Rytov approximation in terms of a given RI distribution. The above derivations used a constraint for the scattered Rytov phase $\varphi_\mathrm{s}(\mathbf{r})$.

$$\begin{aligned} (\nabla\varphi_\mathrm{s}(\mathbf{r}))^2 &\ll f(\mathbf{r}) \\ &\overset{\text{eq. 2.12}}{\ll} {k_\mathrm{m}}^2 \left[\left(\frac{n(\mathbf{r})}{n_\mathrm{m}} \right)^2 - 1 \right] \end{aligned} \tag{A.17}$$

$$n(\mathbf{r})^2 \gg {n_\mathrm{m}}^2 \left[\frac{(\nabla\varphi_\mathrm{s}(\mathbf{r}))^2}{{k_\mathrm{m}}^2} + 1 \right] \tag{A.18}$$

From this inequality, we want to derive a condition that connects the RI with its gradient. We insert the definitions of the wave vector k_m and the RI distribution $n(\mathbf{r})$ (eq. 2.9, 2.13) to retrieve a condition for the variation in RI $\epsilon_n(\mathbf{r})$

$$n(\mathbf{r})^2 \gg {n_\mathrm{m}}^2 \left(\frac{\nabla\varphi_\mathrm{s}(\mathbf{r})\lambda}{2\pi n_\mathrm{m}} \right)^2 + {n_\mathrm{m}}^2 \tag{A.19}$$

$$n(\mathbf{r})^2 - {n_\mathrm{m}}^2 \gg \left(\frac{\nabla\varphi_\mathrm{s}(\mathbf{r})\lambda}{2\pi} \right)^2 \tag{A.20}$$

$$\underbrace{\epsilon_n(\mathbf{r})^2}_{\approx 0} + 2n_\mathrm{m}\epsilon_n(\mathbf{r}) \gg \left(\frac{\nabla\varphi_\mathrm{s}(\mathbf{r})\lambda}{2\pi} \right)^2 . \tag{A.21}$$

Because the local variation $\epsilon_n(\mathbf{r})$ is small, we may neglect[1] $\epsilon_n(\mathbf{r})^2$. The resulting constraint for the phase gradient is [Kak+01]

$$\frac{|\nabla\varphi_\mathrm{s}(\mathbf{r})|}{2\pi} \ll \frac{\sqrt{2n_\mathrm{m}\,|\epsilon_n(\mathbf{r})|}}{\lambda}, \tag{A.22}$$

which can be interpreted as

$$\frac{|\mathrm{d}\varphi_\mathrm{s}(\mathbf{r})|}{2\pi} \ll \frac{\sqrt{2n_\mathrm{m}\,|\epsilon_n(\mathbf{r})|}\cdot|\mathrm{d}\mathbf{r}|}{\lambda}. \tag{A.23}$$

For any position $\mathbf{r}$ inside a sample, equation A.23 reads: the sample induces a phase change over a period of 2π radians. This number must be smaller than the variation in RI $\epsilon_n(\mathbf{r})$ along the corresponding optical path scaled by the used wavelength λ. Thus, compared to the Born approximation, where the overall phase change must be smaller than 2π, the Rytov approximation is also valid for thicker samples, as long as the phase change per path length remains small [Sla+84].

It is desirable to translate the constraints on the change of the complex Rytov phase $\varphi_\mathrm{s}(\mathbf{r})$ to constraints on the RI $n(\mathbf{r})$. To achieve that, we assume that the changes in the Rytov phase are equivalent to phase delays due to the real RI

$$|\varphi_\mathrm{s}(\mathbf{r})| \approx |\Delta\Phi(\mathbf{r})|. \tag{A.24}$$

The phase delay $\Delta\Phi(\mathbf{r})$ at a location $\mathbf{r}$ is defined by the optical path that the light has traveled before. We approximate the light path by a straight line along the z-axis and express the phase change in terms of optical path difference

$$\frac{\Delta\Phi(\mathbf{r})}{2\pi} \approx \frac{1}{\lambda}\int_{-\infty}^{z}\epsilon_n(x,y,z')dz'. \tag{A.25}$$

The left side of equation A.22 thus becomes

$$\frac{|\nabla\varphi_\mathrm{s}(\mathbf{r})|}{2\pi} \approx \frac{1}{\lambda}\left|\nabla\int_{-\infty}^{z}dz'\epsilon_n(x,y,z')\right|. \tag{A.26}$$

The right side is valid as long as the light path follows approximately a straight line, which is true within homogeneous objects of a size larger than the wavelength λ. To simplify the expression, we only integrate over characteristic length scale $d_\mathrm{c} > \lambda$ below which the light path can be approximated by a straight line (e.g within the smallest homogeneous compartment in a cell). We change the limits of the integral accordingly, allowing us to move the gradient inside the integral.

$$\frac{|\nabla\varphi_\mathrm{s}(\mathbf{r})|}{2\pi} \approx \frac{1}{\lambda}\left|\int_{0}^{d_\mathrm{c}}dz\nabla\epsilon_n(\mathbf{r})\right| \tag{A.27}$$

[1] This can be shown by solving the quadratic equation A.21 for $\epsilon_n(\mathbf{r})$ and Taylor-expanding for small $\nabla\varphi_\mathrm{s}(\mathbf{r})$ to the second order.

The integral over the z-component of $\nabla\epsilon_n(\mathbf{r})$ computes to zero. The integral over the other two components $\nabla_\perp\epsilon_n(\mathbf{r})$ can be approximated with its average along z ($\langle\cdot\rangle_z$) multiplied by the characteristic length d_c.

$$\frac{|\nabla\varphi_\mathrm{s}(\mathbf{r})|}{2\pi} \approx \frac{1}{\lambda}\,|d_\mathrm{c}\langle\nabla_\perp\epsilon_n(\mathbf{r})\rangle_z| \tag{A.28}$$

Note that the quantity "axially averaged lateral gradient" along z is only defined over the distance d_c. However, because in tomographic imaging cells are imaged from multiple directions, this relation must also hold true when replacing $\nabla_\perp$ by ∇. In addition, we assume that the average gradient of the RI variation is similar in magnitude to $\nabla\epsilon_n(\mathbf{r})$. We then obtain

$$\frac{|\nabla\varphi_\mathrm{s}(\mathbf{r})|}{2\pi} \approx \frac{d_\mathrm{c}\,|\nabla\epsilon_n(\mathbf{r})|}{\lambda}. \tag{A.29}$$

A comparison with equation A.22 yields a criterion of validity for the Rytov approximation expressed in terms of the RI

$$|\nabla n(\mathbf{r})| \ll \frac{\sqrt{2n_\mathrm{m}|n(\mathbf{r})-n_\mathrm{m}|}}{d_\mathrm{c}}, \qquad d_\mathrm{c} > \lambda \tag{2.29}$$

where we substituted $n(\mathbf{r}) = n_\mathrm{m} + \epsilon_n(\mathbf{r})$. Thus, the Rytov approximation is valid when the gradient in the RI is much smaller than the local RI variation. For large objects, the Rytov approximation eventually breaks down.

A.2 The Fourier slice theorem

The Fourier slice theorem is the central theorem in computerized tomography, where x-rays can be assumed to travel along straight lines. The theorem makes a connection between the Fourier transform of each recorded projection and the Fourier transform of the sample volume. This connection in Fourier space has led to the development of the backprojection algorithm, which makes use of the fast Fourier transform to reconstruct tomographic images efficiently (see appendix A.3).

To derive the Fourier slice theorem, consider the projection of a 2D object $f(\mathbf{r})$ onto a detector line. The object is rotated with respect to its center at $\mathbf{r} = 0$ through an angle ϕ_0. For an arbitrary angle ϕ_0, the projection $p_{\phi_0}(x_\mathrm{D})$ at the detector line is the integral of $f(\mathbf{r})$ along lines that are tilted by ϕ_0

$$p_{\phi_0}(x_\mathrm{D}) = \int dt\, f(x(t), z(t)). \tag{A.30}$$

The Fourier transform of this one-dimensional data at the detector line is

$$\widehat{P}_{\phi_0}(k_\mathrm{Dx}) = \frac{1}{\sqrt{2\pi}} \int dx_\mathrm{D}\, p_{\phi_0}(x_\mathrm{D}) \exp(-ik_\mathrm{Dx}x_\mathrm{D}). \tag{A.31}$$

Next, we define the 2D Fourier transform $\widehat{F}(\mathbf{k})$ of the 2D image $f(\mathbf{r})$:

$$\widehat{F}(k_\mathrm{x}, k_\mathrm{z}) = \frac{1}{2\pi} \iint dx dz\, f(x,z) \exp(-i(k_\mathrm{x} x + k_\mathrm{z} z)) \tag{A.32}$$

In order to draw a connection between $\widehat{F}(k_\mathrm{x}, k_\mathrm{z})$ and $\widehat{P}_{\phi_0}(k_\mathrm{Dx})$, the coordinates of the object $f(\mathbf{r})$ must be rotated through the angle ϕ_0. The coordinate transform from (x, z) to the detector line (x_D and the and the integration parameter t yields

$$\widehat{F}_{\phi_0}(k_\mathrm{Dx}, k_\mathrm{t}) = \frac{1}{2\pi} \iint dx_\mathrm{D} dt\, f_{\phi_0}(x_\mathrm{D}, t) \exp(-i(k_\mathrm{Dx} x_\mathrm{D} + k_\mathrm{t} t)) \tag{A.33}$$

$$f_{\phi_0}(x_\mathrm{D}, t) = f(x_\mathrm{D} \cos\phi_0 - t \sin\phi_0,\ x_\mathrm{D} \sin\phi_0 + t \cos\phi_0) \tag{A.34}$$

$$\widehat{F}_{\phi_0}(k_\mathrm{Dx}, k_\mathrm{t}) = F(k_\mathrm{Dx} \cos\phi_0 - k_\mathrm{t} \sin\phi_0,\ k_\mathrm{Dx} \sin\phi_0 + k_\mathrm{t} \cos\phi_0) \tag{A.35}$$

For the case $k_\mathrm{t} = 0$, which implies slicing the Fourier transform $\widehat{F}(\mathbf{k})$ at the angle ϕ_0, we arrive at the Fourier slice theorem [Bra56; Mer76; Bro+76]

$$\widehat{F}_{\phi_0}(k_\mathrm{Dx}, 0) = \frac{1}{\sqrt{2\pi}} \widehat{P}_{\phi_0}(k_\mathrm{Dx}) \tag{3.5}$$

This formula, the Fourier slice theorem, states that the Fourier transform of a projection $\widehat{P}$ imaged at an angle ϕ_0 lies on a straight line that slices through the center of the Fourier transform of the object $\widehat{F}$ at the same angle ϕ_0 (see figure 3.3).

A.3 The backprojection algorithm

The backprojection algorithm is a tomographic reconstruction method that is based on the Fourier slice theorem (appendix A.2). Its implementation takes advantage of the fast Fourier transform, which makes it a highly efficient technique.

To derive the backprojection algorithm, we start by expressing the object function in terms of its Fourier transform $\widehat{F}(\mathbf{k})$.

$$f(x,z) = \frac{1}{2\pi} \iint dk_\mathrm{x} dk_\mathrm{z}\, \widehat{F}(k_\mathrm{x}, k_\mathrm{z}) \exp(i(k_\mathrm{x} x + k_\mathrm{z} z)) \tag{A.36}$$

We then perform a coordinate transform from $(k_\mathrm{x}, k_\mathrm{z})$ to (k_Dx, ϕ_0). It can be easily shown that the Jacobain of this coordinate transform computes to

$$\left| \det \left(\frac{d(k_\mathrm{x}, k_\mathrm{z})}{d(k_\mathrm{Dx}, \phi_0)} \right) \right| = |k_\mathrm{Dx}| \tag{A.37}$$

$$k_\mathrm{x} = k_\mathrm{Dx} \cos\phi_0 - k_\mathrm{t} \sin\phi_0 \tag{A.38}$$

$$k_\mathrm{z} = k_\mathrm{Dx} \sin\phi_0 + k_\mathrm{t} \cos\phi_0 \tag{A.39}$$

$$k_\mathrm{t} = 0 \tag{A.40}$$

Therefore, using equations 3.5 to A.40, we obtain directions for computing the object function $f(x, z)$ from the Fourier-transformed projections $\widehat{P}_{\phi_0}(k_\mathrm{Dx})$ [Bra56;

Mer76; Bro+76; Cro+70; Ram+71]:

$$f(x,z) = \frac{1}{2\pi}\int dk_{\mathrm{Dx}} \int_0^{\pi} d\phi_0 \; |k_{\mathrm{Dx}}| \, \frac{\widehat{P}_{\phi_0}(k_{\mathrm{Dx}})}{\sqrt{2\pi}} \exp[ik_{\mathrm{Dx}}(x\cos\phi_0 + z\sin\phi_0)] \quad \text{(A.41)}$$

Here, the integral over ϕ_0 runs from 0 to π. The integrals of k_{x}, k_{z}, and k_{Dx} are computed over the entire k-space, i.e. over the interval $(-\infty, +\infty)$. The term $|k_{\mathrm{Dx}}|$ is a ramp filter in Fourier space[2]. Note that because of our chosen coordinate system, at the angle $\phi_0 = 0$, k_{Dx} coincides with the k_{x} axis ($x_{\mathrm{D}} \overset{\phi_0=0}{=} x$).

We do not need to numerically integrate equation A.41. Instead, we identify another Fourier transform for the reciprocal vector $\mathbf{k_D}$ that allows us to apply the fast Fourier transform. The data in real space at $\mathbf{r} = (x, z)$ are computed from integrals over k_{Dx} and ϕ_0. We can introduce a coordinate transform $D_{-\phi_0}$ that rotates $\mathbf{r}$ through the angle $-\phi_0$ along the y-axis, such that $x_{\phi_0} = x\cos\phi_0 + z\sin\phi_0$. In the following, equation we identify a one-dimensional inverse Fourier transform

$$f(x,z) = \frac{1}{2\pi}\int_0^{\pi} d\phi_0 \; D_{-\phi_0}\Bigg\{ \underbrace{\int dk_{\mathrm{Dx}} \, |k_{\mathrm{Dx}}| \, \frac{\widehat{P}_{\phi_0}(k_{\mathrm{Dx}})}{\sqrt{2\pi}} \exp[ik_{\mathrm{Dx}} x_{\phi_0}]}_{\mathrm{FFT}_{1\mathrm{D}}^{-1}\left\{|k_{\mathrm{Dx}}|\widehat{P}_{\phi_0}(k_{\mathrm{Dx}})\right\}} \Bigg\} \quad \text{(A.42)}$$

We have effectively replaced the integral over k_{Dx} by a one-dimensional inverse fast Fourier transform ($\mathrm{FFT}_{1\mathrm{D}}^{-1}$) and a rotation in real space ($D_{-\phi_0}$). To obtain a discrete description of the problem, we replace the remaining integral over ϕ_0 by a discrete sum over N_{A} equidistant projections.

$$f(x,z) = \frac{1}{2\pi} D_{-\phi_j}\Big\{ \mathrm{FFT}_{1\mathrm{D}}^{-1}\left\{ |k_{\mathrm{Dx}}| \, \widehat{P}_{\phi_j}(k_{\mathrm{Dx}}) \right\} \Big\} \quad \text{(3.6)}$$

with the discrete angular distance $\Delta\phi_0 = \pi/N_{\mathrm{A}}$ and the discrete angles $\phi_j = j \cdot \Delta\phi_0$ ($j = 1, 2, \ldots, N_{\mathrm{A}}$). A numerical method that implements equation 3.6 is much faster than the direct computation of equation A.41, because it can make use of the fast Fourier transform. Figure A.1 depicts the process from image acquisition to image reconstruction with the backprojection algorithm.

Besides the backprojection algorithm, there exist other reconstruction techniques for computerized tomography that are all based on the Radon transform. Iterative techniques such as SART (simultaneous algebraic reconstruction technique) are able to improve the reconstructed image quality but require a larger computational effort.

[2]This ramp filter is what gave the *filtered* backprojection algorithm its name

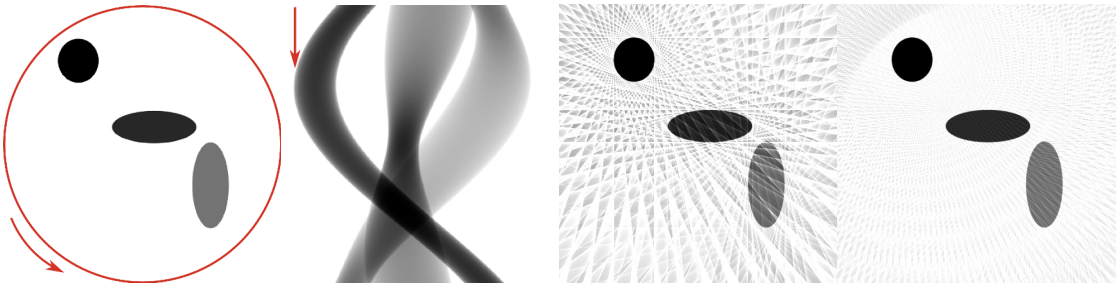

(a) original image, 500×500 **pixels** | **(b) sinogram, 500 projections** | **(c) reconstruction from 30 projections** | **(d) reconstruction from 100 projections**

Figure A.1, Qualitative description of the backprojection algorithm. a) The original two-dimensional image contains ellipses with different gray-scale levels. **b)** The sinogram shows 500 projection of image (a) from 0° to 180°. For the computation of the sinogram, only the circular region of the original image (red) was used. **c)** Reconstruction using 30 equisdistant projections. **d)** Reconstruction with 100 projections. The data were generated with radontea [Mül13b]. This figure was previously published in [Mül+15d].

A.4 The Fourier diffraction theorem in 2D

To derive the Fourier diffraction theorem, we start with the inhomogeneous wave equation previously discussed in section 2.3.1.

$$\left(\nabla^2 + {k_\mathrm{m}}^2\right) u(\mathbf{r}) = -\delta(\mathbf{r} - \mathbf{r}') \tag{A.43}$$

In the 2D case, the Green's function is the zero-order Hankel function of the first kind.

$$G(\mathbf{r} - \mathbf{r}') = \frac{\exp(ik_\mathrm{m} \left|\mathbf{r} - \mathbf{r}'\right|)}{4\pi \left|\mathbf{r} - \mathbf{r}'\right|} \tag{A.44}$$

$$= \frac{i}{4} H_0^{(1)}(k_\mathrm{m} \left|\mathbf{r} - \mathbf{r}'\right|) \tag{A.45}$$

$$H_0^{(1)}(k_\mathrm{m} \left|\mathbf{r} - \mathbf{r}'\right|) = \frac{1}{\pi} \int dk_\mathrm{x} \frac{1}{k_\mathrm{z}} \exp\{i \left[k_\mathrm{x}(x - x') + k_\mathrm{z}(z - z')\right]\} \tag{A.46}$$

$$k_\mathrm{z} = \sqrt{{k_\mathrm{m}}^2 - k_\mathrm{x}^2} \tag{A.47}$$

Equation A.47 is a restriction for the wave vector $\mathbf{k} = (k_\mathrm{x}, k_\mathrm{z})$ in Fourier space. Its magnitude is defined by the wave number k_m. To simplify the notation, we introduce the unit vector s that describes the direction of propagation of a plane wave $\mathbf{k} = k_\mathrm{m}\mathbf{s}$. Accordingly, we introduce the following substitutions:

$$k_\mathrm{x} = k_\mathrm{m} p\,, \qquad k_\mathrm{z} = k_\mathrm{m} M \tag{A.48}$$

$$M = \sqrt{1 - p^2}\,, \qquad M_0 = \sqrt{1 - p_0^2} \tag{A.49}$$

$$\mathbf{s} = (p,\, M)\,, \qquad \mathbf{s}_0 = (p_0,\, M_0) \tag{A.50}$$

The unit vector $\mathbf{s}_0$ describes the propagation direction of the incident plane wave $u_0(\mathbf{r})$ and points at the z-direction when $\phi_0 = 0$.

$$u_0(\mathbf{r}) = a_0 \exp(ik_\mathrm{m}\mathbf{s}_0\mathbf{r}) \tag{A.51}$$

$$\mathbf{s}_0 = (-\sin\phi_0,\ \cos\phi_0) \tag{A.52}$$

With these substitutions, the Green's function becomes

$$G(\mathbf{r}-\mathbf{r}') = \frac{i}{4\pi}\int dp \frac{1}{M}\exp\{ik_\mathrm{m}\left[p(x-x') + M(z-z')\right]\}. \tag{A.53}$$

The first Born approximation in 2D then reads (see section 2.3.2)

$$u_\mathrm{B}(\mathbf{r}) = \iint d^2r' G(\mathbf{r}-\mathbf{r}')f(\mathbf{r}')u_0(\mathbf{r}'). \tag{A.54}$$

Our goal is to invert this equation and obtain $f(\mathbf{r})$ from the measured field $u_\mathrm{B}(\mathbf{r})$. To achieve that, we search for a way to rewrite the double integral as a Fourier transform. In this notation, the Fourier transform $\widehat{F}(\mathbf{k})$ of a function $f(\mathbf{r})$ is defined as

$$\widehat{F}(\mathbf{k}) = \frac{1}{2\pi}\iint d^2r\, f(\mathbf{r})\exp(-i\mathbf{k}\mathbf{r}) \tag{A.55}$$

$$f(\mathbf{r}) = \frac{1}{2\pi}\iint d^2k\, \widehat{F}(\mathbf{k})\exp(i\mathbf{k}\mathbf{r}). \tag{A.56}$$

In the derivations that follow, we will also make use of the identity of the Dirac delta distribution

$$\delta(p-a) = \frac{1}{2\pi}\int dx\ \exp(i(p-a)x). \tag{A.57}$$

Our first step is to insert equation A.53 into equation A.54:

$$u_\mathrm{B}(\mathbf{r}) = \frac{i}{4\pi}\iint d^2r'\ \int dp\ \frac{1}{M}\exp[ik_\mathrm{m}p(x-x') + ik_\mathrm{m}M(z-z')]\cdot f(\mathbf{r}')a_0\exp(ik_\mathrm{m}(p_0x'+M_0z')) \tag{A.58}$$

We can replace the integral over r' with the Fourier transform of $f(\mathbf{r}')$, but have to take into account the argument with the shifted coordinates $(\mathbf{s}-\mathbf{s_0})$

$$\widehat{F}(k_\mathrm{m}(\mathbf{s}-\mathbf{s}_0)) = \frac{1}{2\pi}\iint d^2r' f(\mathbf{r}')\exp(-ik_\mathrm{m}(\mathbf{s}-\mathbf{s}_0)\mathbf{r}'). \tag{A.59}$$

Thus, the equation for the Born approximation simplifies to

$$u_\mathrm{B}(\mathbf{r}) = \frac{ia_0}{4\pi}\int dp\ \frac{2\pi}{M}\widehat{F}(k_\mathrm{m}(\mathbf{s}-\mathbf{s}_0))\exp(ik_\mathrm{m}\mathbf{s}\mathbf{r}). \tag{A.60}$$

The field $u_{\mathrm{B}}(\mathbf{r})$ describes the the field of the scattered wave in the Born approximation at any point $\mathbf{r}$. However, we are interested in the field at the detector line $\mathbf{r_D}$. Therefore, we substitute $\mathbf{r} \rightarrow \mathbf{r_D} = (x_{\mathrm{D}}, l_{\mathrm{D}})$, where l_{D} is the distance of the detector plane from the center of rotation. Furthermore, we now explicitly point out the ϕ_0-dependence in the subscript $u_{\mathrm{B}}(\mathbf{r_D}) \rightarrow u_{\mathrm{B},\phi_0}(\mathbf{r_D})$, which denotes the angular position of the detector and the direction of the incoming plane wave with respect to the sample $\mathbf{s}_0$.

$$u_{\mathrm{B},\phi_0}(\mathbf{r_D}) = \frac{ia_0}{2} \int dp \, \frac{1}{M} \widehat{F}(k_{\mathrm{m}}(\mathbf{s}-\mathbf{s}_0)) \exp(ik_{\mathrm{m}}\mathbf{s}\mathbf{r_D}) \tag{A.61}$$

The next step is to perform a one-dimensional Fourier transform of $u_{\mathrm{B}}(\mathbf{r_D})$ along x_{D}

$$\widehat{U}_{\mathrm{B},\phi_0}(k_{\mathrm{Dx}}) = \frac{ia_0}{2\sqrt{2\pi}} \int dx_{\mathrm{D}} \int dp \, \frac{1}{M} \widehat{F}(k_{\mathrm{m}}(\mathbf{s}-\mathbf{s}_0)) \cdot \exp(ik_{\mathrm{m}}(px_{\mathrm{D}}+Ml_{\mathrm{D}})) \exp(-ik_{\mathrm{Dx}}x_{\mathrm{D}}), \tag{A.62}$$

where we identify the delta distribution

$$\delta(k_{\mathrm{m}}p - k_{\mathrm{Dx}}) = \frac{1}{2\pi} \int dx_{\mathrm{D}} \, \exp(i(k_{\mathrm{m}}p - k_{\mathrm{Dx}})x_{\mathrm{D}}) \tag{A.63}$$

$$\delta(k_{\mathrm{m}}p - k_{\mathrm{Dx}}) = \frac{1}{|k_{\mathrm{m}}|} \delta(p - k_{\mathrm{Dx}}/k_{\mathrm{m}}) \tag{A.64}$$

which simplifies out expression to

$$\widehat{U}_{\mathrm{B},\phi_0}(k_{\mathrm{Dx}}) = \frac{ia_0 2\pi}{2\sqrt{2\pi}} \int dp \, \frac{1}{M} \widehat{F}(k_{\mathrm{m}}(\mathbf{s}-\mathbf{s}_0)) \exp(ik_{\mathrm{m}}Ml_{\mathrm{D}}) \delta(k_{\mathrm{m}}p - k_{\mathrm{Dx}}). \tag{A.65}$$

Finally, we use the delta distribution to solve the integral over dp and arrive at the Fourier diffraction theorem.

$$\widehat{U}_{\mathrm{B},\phi_0}(k_{\mathrm{Dx}}) = \frac{ia_0}{k_{\mathrm{m}}} \sqrt{\frac{\pi}{2}} \frac{1}{M} \widehat{F}(k_{\mathrm{m}}(\mathbf{s}-\mathbf{s}_0)) \exp(ik_{\mathrm{m}}Ml_{\mathrm{D}}) \tag{A.66}$$

Solving for the Fourier transformed object $\widehat{F}$ yields

$$\widehat{F}(k_{\mathrm{m}}(\mathbf{s}-\mathbf{s}_0)) = -\sqrt{\frac{2}{\pi}} \frac{ik_{\mathrm{m}}}{a_0} M \widehat{U}_{\mathrm{B},\phi_0}(k_{\mathrm{Dx}}) \exp(-ik_{\mathrm{m}}Ml_{\mathrm{D}}) \, . \tag{3.7}$$

The restriction in equation A.49 forces the one-dimensional Fourier transform of the scattered wave $\widehat{U}_{\mathrm{B},\phi_0}(k_{\mathrm{Dx}})$ to be placed on circular arcs in Fourier space.

$$k_{\mathrm{m}}\mathbf{s} = (k_{\mathrm{Dx}} \cos\phi_0 - k_{\mathrm{m}}M \sin\phi_0, k_{\mathrm{Dx}} \sin\phi_0 + k_{\mathrm{m}}M \cos\phi_0) \tag{A.67}$$

$$k_{\mathrm{m}}M = \sqrt{{k_{\mathrm{m}}}^2 - k_{\mathrm{Dx}}^2} \tag{A.68}$$

The argument $k_{\mathrm{m}}(\mathbf{s}-\mathbf{s}_0)$ shifts the circular arcs in Fourier space such that $\widehat{U}_{\mathrm{B},\phi_0}(0)$ is centered at $\widehat{F}(0,0)$ (see figure 3.5).

A.4.1 Comparison to the Fourier slice theorem

We can write equation 3.7 in the same manner as equation 3.5, with the subscript ϕ_0 denoting the rotation of the object $f(\mathbf{r})$. Hence, we can easily compare the 2D Fourier diffraction theorem with the Fourier slice theorem from appendix A.2:

	$\widehat{F}_{\phi_0}(k_{\mathrm{x}},k_{\mathrm{z}}) = A_{\mathrm{rel}} \cdot \sqrt{\frac{1}{2\pi}}\widehat{P}_{\phi_0}(k_{\mathrm{Dx}})$	
	Fourier slice theorem (eq. 3.5)	**Fourier diffraction theorem** (eq. 3.7)
Sinogram $\widehat{P}_{\phi_0}(k_{\mathrm{Dx}})$	Fourier transform of projections $\widehat{P}_{\phi_0}(k_{\mathrm{Dx}})$	Fourier transform of complex scattered wave $\widehat{U}_{\mathrm{B},\phi_0}(k_{\mathrm{Dx}})$
Factor A_{rel}	$A_{\mathrm{rel}} = 1$	$A_{\mathrm{rel}} = -\frac{2ik_{\mathrm{m}}M}{a_0}\exp(-ik_{\mathrm{m}}Ml_{\mathrm{D}})$
Coordinates $(k_{\mathrm{x}},k_{\mathrm{z}})$ sliced at ϕ_0	$k_{\mathrm{x}} = k_{\mathrm{Dx}}$ $k_{\mathrm{z}} = k_{\mathrm{t}} = 0$ (straight line)	$k_{\mathrm{x}} = k_{\mathrm{Dx}}$ $k_{\mathrm{z}} = \sqrt{{k_{\mathrm{m}}}^2 - k_{\mathrm{Dx}}^2} - k_{\mathrm{m}}$ (semicircular arc)

Table A.1, The Fourier slice theorem and the Fourier diffraction theorem. Both theorems connect the measured data to the Fourier transform of the object. The differences are the complex factor A_{rel} and the distribution of measured data in Fourier space.

A.4.2 Comparison to the Fourier diffraction theorem in 3D

In 3D, the Fourier diffraction theorem can be derived analogous to the 2D case. The main difference in the derivation is the Green's function, which in 3D becomes [Alf66].

$$G(\mathbf{r}-\mathbf{r}') = \frac{ik_\mathrm{m}}{8\pi^2}\iint dpdq\frac{1}{M}\exp\{ik_\mathrm{m}\left[p(x-x')+q(y-y')+M(z-z')\right]\} \quad \text{(A.69)}$$

The Fourier diffraction theorem in 3D, which is derived in detail in [Mül+15d], is identical to the theorem in 2D. Table A.2 shows the only differences between them, which are a result of the different dimensions.

	$\widehat{F}(\mathbf{k}) = A_\mathrm{rel}\cdot\sqrt{\frac{1}{2\pi}}\widehat{U}_{\mathrm{B},\phi_0}(\mathbf{k_D})$	
	2D	**3D**
Sinogram $\widehat{U}_{\mathrm{B},\phi_0}(\mathbf{k_D})$	1D Fourier transform of complex scattered wave $\widehat{U}_{\mathrm{B},\phi_0}(k_\mathrm{Dx})$	2D Fourier transform of complex scattered wave $\widehat{U}_{\mathrm{B},\phi_0}(k_\mathrm{Dx}, k_\mathrm{Dy})$
Factor A_rel	$A_\mathrm{rel} = -\frac{2ik_\mathrm{m}M}{a_0}\exp(-ik_\mathrm{m}Ml_\mathrm{D})$	
	$M = \frac{1}{k_\mathrm{m}}\sqrt{{k_\mathrm{m}}^2 - k_\mathrm{Dx}^2}$	$M = \frac{1}{k_\mathrm{m}}\sqrt{{k_\mathrm{m}}^2 - k_\mathrm{Dx}^2 - k_\mathrm{Dy}^2}$
Coordinates $\mathbf{k}$ at $\phi_0 = 0$	$\mathbf{k} = (k_\mathrm{x}, k_\mathrm{z})$ $k_\mathrm{x} = k_\mathrm{Dx}$ $k_\mathrm{z} = \sqrt{{k_\mathrm{m}}^2 - k_\mathrm{Dx}^2} - k_\mathrm{m}$ (semicircular arc)	$\mathbf{k} = (k_\mathrm{x}, k_\mathrm{y}, k_\mathrm{z})$ $k_\mathrm{x} = k_\mathrm{Dx}, \quad k_\mathrm{y} = k_\mathrm{Dy}$ $k_\mathrm{z} = \sqrt{{k_\mathrm{m}}^2 - k_\mathrm{Dx}^2 - k_\mathrm{Dy}^2} - k_\mathrm{m}$ (semispherical surface)

Table A.2, The Fourier diffraction theorem in 2D and in 3D. The Fourier diffraction theorem in 3D has the same form as the 2D version. The only differences come from the different number of dimensions. Note that this notation implies a rotation about the y-axis and that the 2D version has coordinates (x, z). For a comparison to the Fourier slice theorem, see table A.1.

A.5 The backpropagation algorithm in 2D

The backpropagation algorithm solves the inverse problem for the Born or the Rytov approximation for diffraction tomography. Its derivation follows closely that of the backprojection algorithm discussed in appendix A.3. We again perform a coordinate transform from $(k_\mathrm{x}, k_\mathrm{z})$ to (k_Dx, ϕ_0) and start by computing the inverse 2D Fourier transform of equation 3.7.

$$\widehat{F}(k_\mathrm{m}(\mathbf{s}-\mathbf{s}_0)) = -\sqrt{\frac{2}{\pi}}\frac{ik_\mathrm{m}}{a_0} M\widehat{U}_{\mathrm{B},\phi_0}(k_\mathrm{Dx})\exp(-ik_\mathrm{m}Ml_\mathrm{D}) \tag{3.7}$$

$$f(\mathbf{r}) = -\sqrt{\frac{2}{\pi}}\frac{ik_\mathrm{m}}{2a_0\pi}\iint dk_\mathrm{x}dk_\mathrm{z}\, M\widehat{U}_{\mathrm{B},\phi_0}(k_\mathrm{Dx})\cdot \exp(-ik_\mathrm{m}Ml_\mathrm{D})\exp(ik_\mathrm{m}(\mathbf{s}-\mathbf{s}_0)\mathbf{r}) \tag{A.70}$$

$$(k_\mathrm{x}, k_\mathrm{z}) = k_\mathrm{m}(\mathbf{s}-\mathbf{s}_0) \tag{A.71}$$

As described in table A.1, the input data are distributed along circular arcs in Fourier space. The orientation of these arcs is defined by the acquisition angle ϕ_0 with the rotation matrix D_{ϕ_0}.

$$D_{\phi_0} = \begin{pmatrix} \cos\phi_0 & -\sin\phi_0 \\ \sin\phi_0 & \cos\phi_0 \end{pmatrix} \tag{A.72}$$

$$\mathbf{k} = D_{\phi_0}\mathbf{k}' \tag{A.73}$$

Here, $\mathbf{k}$ denotes the non-rotated Fourier space, whereas $\mathbf{k}'$ denotes the positions of acquisition at a certain angle ϕ_0. We have defined the angle ϕ_0 such that, $k'_\mathrm{x} = k_\mathrm{Dx}$ and therefore $k'_\mathrm{z} = \sqrt{{k_\mathrm{m}}^2 - k_\mathrm{Dx}^2} - k_\mathrm{m}$. The coordinate transform from $(k_\mathrm{x}, k_\mathrm{z})$ to (k_Dx, ϕ_0) is fully described by

$$k_\mathrm{x} = k_\mathrm{Dx}\cos\phi_0 - \left[\sqrt{{k_\mathrm{m}}^2 - k_\mathrm{Dx}^2} - k_\mathrm{m}\right]\sin\phi_0 \tag{A.74}$$

$$k_\mathrm{z} = k_\mathrm{Dx}\sin\phi_0 + \left[\sqrt{{k_\mathrm{m}}^2 - k_\mathrm{Dx}^2} - k_\mathrm{m}\right]\cos\phi_0. \tag{A.75}$$

To perform the change of variables in the integral above from $dk_\mathrm{x}dk_\mathrm{z}$ to $dk_\mathrm{Dx}d\phi_0$, we compute the Jacobian matrix J and its determinant.

$$J = \frac{\partial k_\mathrm{x}\partial k_\mathrm{z}}{\partial k_\mathrm{Dx}\partial\phi_0} \tag{A.76}$$

$$= \begin{pmatrix} \cos\phi_0 + \frac{k_\mathrm{Dx}}{\sqrt{{k_\mathrm{m}}^2-k_\mathrm{Dx}^2}}\sin\phi_0 & -k_\mathrm{Dx}\sin\phi_0 - \left[\sqrt{{k_\mathrm{m}}^2 - k_\mathrm{Dx}^2} - k_\mathrm{m}\right]\cos\phi_0 \\ \sin\phi_0 - \frac{k_\mathrm{Dx}}{\sqrt{{k_\mathrm{m}}^2-k_\mathrm{Dx}^2}}\cos\phi_0 & k_\mathrm{Dx}\cos\phi_0 - \left[\sqrt{{k_\mathrm{m}}^2 - k_\mathrm{Dx}^2} - k_\mathrm{m}\right]\sin\phi_0 \end{pmatrix} \tag{A.77}$$

The determinant of the Jacobian J computes to

$$\det(J) = k_{\mathrm{Dx}} - \left(k_{\mathrm{Dx}} - \frac{k_{\mathrm{m}} k_{\mathrm{Dx}}}{\sqrt{{k_{\mathrm{m}}}^2 - k_{\mathrm{Dx}}^2}} \right) = \frac{k_{\mathrm{m}} k_{\mathrm{Dx}}}{\sqrt{{k_{\mathrm{m}}}^2 - k_{\mathrm{Dx}}^2}}. \tag{A.78}$$

With the coordinate transform applied to equation A.70, we obtain the backpropagation formula

$$f(\mathbf{r}) = -\sqrt{\frac{2}{\pi}} \frac{i k_{\mathrm{m}}}{2 a_0 \pi} \int dk_{\mathrm{Dx}} \frac{1}{2} \int_0^{2\pi} d\phi_0 \left| \frac{k_{\mathrm{m}} k_{\mathrm{Dx}}}{\sqrt{{k_{\mathrm{m}}}^2 - k_{\mathrm{Dx}}^2}} \right| M \widehat{U}_{\mathrm{B},\phi_0}(k_{\mathrm{Dx}}) \cdot \exp(-i k_{\mathrm{m}} M l_{\mathrm{D}}) \exp(i k_{\mathrm{m}} (\mathbf{s} - \mathbf{s}_0) \mathbf{r}) \tag{A.79}$$

Note that the integration over ϕ_0 goes from 0 to 2π, which results in a double-coverage of the Fourier space. To correct for that, we introduce the additional factor $\frac{1}{2}$. Furthermore, we express $(\mathbf{s} - \mathbf{s_0})$ in terms of a lateral $(\mathbf{t}_\perp)$ and an axial $(\mathbf{s}_0)$ component (eq. A.74 and A.75).

$$k_{\mathrm{m}}(\mathbf{s} - \mathbf{s_0}) = k_{\mathrm{Dx}} \, \mathbf{t}_\perp + k_{\mathrm{m}}(M-1) \, \mathbf{s}_0 \tag{A.80}$$

$$\mathbf{s_0} = (p_0,\, M_0) = (-\sin\phi_0,\, \cos\phi_0) \tag{A.81}$$

$$\mathbf{t}_\perp = (-M_0,\, p_0) = (\cos\phi_0,\, \sin\phi_0) \tag{A.82}$$

By assuming that $(k_{\mathrm{m}} M)^2 = {k_{\mathrm{m}}}^2 - k_{\mathrm{Dx}}^2 \overset{!}{>} 0$, we can rewrite the backpropagation formula as

$$f(\mathbf{r}) = -\frac{i k_{\mathrm{m}}}{a_0 (2\pi)^{3/2}} \int dk_{\mathrm{Dx}} \int_0^{2\pi} d\phi_0 \; |k_{\mathrm{Dx}}| \, \widehat{U}_{\mathrm{B},\phi_0}(k_{\mathrm{Dx}}) \exp(-i k_{\mathrm{m}} M l_{\mathrm{D}}) \cdot \exp[i(k_{\mathrm{Dx}} \, \mathbf{t}_\perp + k_{\mathrm{m}}(M-1) \, \mathbf{s}_0)\mathbf{r}]. \tag{A.83}$$

To derive the backpropagation algorithm from the above equation, we can apply the same principles used in appendix A.3. We begin by introducing the rotation $D_{-\phi_0}$ through $-\phi_0$ about the y-axis that transforms $\mathbf{r}$ to $\mathbf{r}_{\boldsymbol{\phi_0}}$.

$$\begin{aligned} \mathbf{r}_{\boldsymbol{\phi_0}} &= (x_{\phi_0}, z_{\phi_0}) \\ x_{\phi_0} &= x\cos\phi_0 + z\sin\phi_0 \\ z_{\phi_0} &= -x\sin\phi_0 + z\cos\phi_0 \end{aligned} \qquad \begin{aligned} \mathbf{t}_\perp \cdot \mathbf{r} &= x_{\phi_0} \\ \mathbf{s_0} \cdot \mathbf{r} &= z_{\phi_0} \end{aligned}$$

$$f(\mathbf{r}) = -\frac{i k_{\mathrm{m}}}{a_0 (2\pi)^{3/2}} \int_0^{2\pi} d\phi_0 \, D_{-\phi_0} \Bigg\{ \int dk_{\mathrm{Dx}} \, |k_{\mathrm{Dx}}| \, \widehat{U}_{\mathrm{B},\phi_0}(k_{\mathrm{Dx}}) \exp(-i k_{\mathrm{m}} M l_{\mathrm{D}}) \exp[i(k_{\mathrm{Dx}} x_{\phi_0} + k_{\mathrm{m}}(M-1) z_{\phi_0})] \Bigg\} \tag{A.84}$$

Because of the factor $k_{\mathrm{m}}(M-1)\,z_{\phi_0}$ in the integral, we cannot proceed exactly as we did for the backprojection algorithm. Here, the inverse Fourier transform is applied for all coordinates z_{ϕ_0} before the rotation is performed.

$$f(\mathbf{r}) = -\frac{ik_{\mathrm{m}}}{2\pi\cdot a_0}\int_0^{2\pi} d\phi_0\, D_{-\phi_0}\Bigg\{ \mathrm{FFT}_{1\mathrm{D}}^{-1}\left\{ |k_{\mathrm{Dx}}|\,\widehat{U}_{\mathrm{B},\phi_0}(k_{\mathrm{Dx}})\exp(-ik_{\mathrm{m}}Ml_{\mathrm{D}})\exp[ik_{\mathrm{m}}(M-1)z_{\phi_0}]\right\}\Bigg\} \tag{A.85}$$

The discretization of the integral over ϕ_0 can be performed according to appendix A.3.

$$f(\mathbf{r}) = -\frac{ik_{\mathrm{m}}}{2\pi\cdot a_0}\sum_{j=1}^{N_{\mathrm{A}}}\Delta\phi_0\, D_{-\phi_j}\Bigg\{ \mathrm{FFT}_{1\mathrm{D}}^{-1}\left\{ |k_{\mathrm{Dx}}|\,\widehat{U}_{\mathrm{B},\phi_j}(k_{\mathrm{Dx}})\exp(-ik_{\mathrm{m}}Ml_{\mathrm{D}})\exp\big[ik_{\mathrm{m}}(M-1)z_{\phi_j}\big]\right\}\Bigg\} \tag{A.86}$$

with the discrete angular distance $\Delta\phi_0 = 2\pi/N_{\mathrm{A}}$ and the discrete angles $\phi_j = j\cdot\Delta\phi_0$ $(j = 1, 2, \ldots, N_{\mathrm{A}})$. In practice, the measured field at the detector is background corrected, which implies dividing by the incident plane wave at the detector $u_0(l_{\mathrm{D}})$. This last step simplifies the backpropagation formula to

$$u_0(l_{\mathrm{D}}) = a_0\exp(ik_{\mathrm{m}}l_{\mathrm{D}}) \tag{A.87}$$

$$f(\mathbf{r}) = -\frac{ik_{\mathrm{m}}}{2\pi}\sum_{j=1}^{N_{\mathrm{A}}}\Delta\phi_0\, D_{-\phi_j}\Bigg\{ \mathrm{FFT}_{1\mathrm{D}}^{-1}\left\{ |k_{\mathrm{Dx}}|\,\frac{\widehat{U}_{\mathrm{B},\phi_j}(k_{\mathrm{Dx}})}{u_0(l_{\mathrm{D}})}\exp\big[ik_{\mathrm{m}}(M-1)(z_{\phi_j}-l_{\mathrm{D}})\big]\right\}\Bigg\}. \tag{3.8}$$

The incident plane wave $u_0(l_{\mathrm{D}})$ is independent of the lateral detector coordinates $\mathbf{r_D}$ and can be interpreted as the normalization of $u_{\mathrm{B},\Phi_{\mathrm{j}}}(x_{\mathrm{D}})$ prior to its Fourier transform to $\widehat{U}_{\mathrm{B},\Phi_{\mathrm{j}}}(k_{\mathrm{Dx}})$.

As previously discussed, the Rytov approximation is better than the Born approximation for dielectric objects with the size of a couple of wavelengths. Figure A.2 illustrates this extreme difference for the backpropagation of a dielectric cylinder.

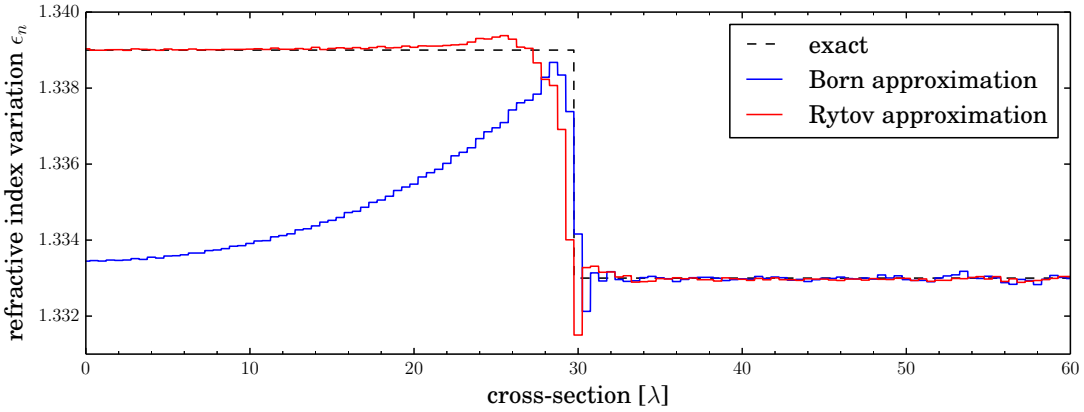

Figure A.2, Line profile of a backpropagated cylinder. The refractive index (RI) of the medium is $n_\mathrm{m} = 1.333$ and the local variation inside the cylinder is $\epsilon_n(\mathbf{r}) = n(\mathbf{r}) - n_\mathrm{m} = 0.006$. The radius of the cylinder is 30λ (vacuum wavelength λ). The scattered wave is computed at an optical distance of $z_\mathrm{D} = 100\lambda$ from the center of the cylinder and sampled at $\lambda/2$ over 512 pixels. The RI map is reconstructed on a grid of 512×512 pixels. This figure was previously published in [Mül+15d].

A.5.1 Comparison to backprojection

When comparing this equation with the backprojection algorithm from equation 3.6, we can see one major difference besides the different filter: for backpropagation, the inverse Fourier transform must be calculated separately for every distance z_{ϕ_j}. In practice, one first needs to calculate the one-dimensional signal $\widehat{U}_{\mathrm{B},\phi_j}(k_{\mathrm{Dx}})\exp(-ik_{\mathrm{m}}Ml_{\mathrm{D}})$ and then expand the signal by one dimension through the application of the second filter $\exp\left[ik_{\mathrm{m}}(M-1)\,z_{\phi_j}\right]$. The inverse Fourier transform is then computed along the axis with constant z_{ϕ_j} and the resulting 2D data are rotated by ϕ_j and added to the reconstruction plane. The name "filtered backpropagation" comes from an interpretation of the z_{ϕ_j}-exponential, which looks like a propagation in z_{ϕ_j}-direction. Thus, the main difference to the backprojection algorithm is the dependency on the distance to the detector l_{D} and the propagation direction $\mathbf{s}_0$. Table A.3 shows the differences in detail.

$$f(x,y) = \frac{A_{\mathrm{rel}}}{(2\pi)^{3/2}} \int dk_{\mathrm{Dx}} \int_0^{2\pi} d\phi_0 \, \exp(iB_{\mathrm{rel}})\,|k_{\mathrm{Dx}}|\,\widehat{P}_{\phi_0}(k_{\mathrm{Dx}}) \quad \text{(A.88)}$$

	backprojection (eq. A.41)	**backpropagation** (eq. A.83)
Sinogram $\widehat{P}_{\phi_0}(k_{\mathrm{Dx}})$	Fourier transform of projections $\widehat{P}_{\phi_0}(k_{\mathrm{Dx}})$	Fourier transform of complex scattered wave $\widehat{U}_{\mathrm{B},\phi_0}(k_{\mathrm{Dx}})$
Factor A_{rel}	$A_{\mathrm{rel}} = \frac{1}{2}$ (double coverage)	$A_{\mathrm{rel}} = -\dfrac{ik_{\mathrm{m}}}{a_0}$
Exponent B_{rel}	$B_{\mathrm{rel}} = k_{\mathrm{Dx}}(\mathbf{t}_\perp \mathbf{r})$ $\mathbf{t}_\perp = (\cos\phi_0,\, \sin\phi_0)$	$B_{\mathrm{rel}} = -k_{\mathrm{m}}Ml_{\mathrm{D}} + k_{\mathrm{Dx}}\mathbf{t}_\perp\mathbf{r} + k_{\mathrm{m}}(M-1)\mathbf{s}_0\mathbf{r}$ $\mathbf{t}_\perp = (\cos\phi_0,\, \sin\phi_0)$ $\mathbf{s}_0 = (-\sin\phi_0,\, \cos\phi_0)$

Table A.3, Backprojection and backpropagation. The backpropagation formula is of the same structure as the backprojection formula. However, dependencies on l_{D} and $\mathbf{s}_0$ illustrate the complexity that results from the first Born approximation (See also table A.1). Note that the backprojection formula has a factor of $\frac{1}{2}$ due to the integration limits of ϕ_0 (double coverage).

A.5.2 Comparison to backpropagation in 3D

Table A.4 illustrates the differences between the backpropagation algorithm in 2D and in 3D. As for the Fourier diffraction theorem (tab. A.2), the differences in the backpropagation formula are only due to the dimensionality of the problem [Mül+15d].

	$f(\mathbf{r}) = -\frac{ik_\mathrm{m}}{2\pi a_0}\left(\int dK_\mathrm{D}\right)\int_0^{2\pi} d\phi_0 \, \exp(iB_\mathrm{rel})\,\lvert k_\mathrm{Dx}\rvert\,\widehat{U}_{\mathrm{B},\phi_0}(\mathbf{k_D})$	
	2D	**3D**
Sinogram $\widehat{U}_{\mathrm{B},\phi_0}(\mathbf{k_D})$	1D Fourier transform of complex scattered wave $\widehat{U}_{\mathrm{B},\phi_0}(k_\mathrm{Dx})$	2D Fourier transform of complex scattered wave $\widehat{U}_{\mathrm{B},\phi_0}(k_\mathrm{Dx}, k_\mathrm{Dy})$
Integral dK_D	$\left(\int dK_\mathrm{D}\right) = \frac{1}{\sqrt{2\pi}}\int dk_\mathrm{Dx}$	$\left(\int dK_\mathrm{D}\right) = \frac{1}{2\pi}\iint dk_\mathrm{Dx}\, dk_\mathrm{Dy}$
Exponent B_rel	$B_\mathrm{rel} = -k_\mathrm{m} M l_\mathrm{D} + k_\mathrm{Dx}\mathbf{t}_\perp\mathbf{r} + k_\mathrm{m}(M-1)\mathbf{s}_0\mathbf{r}$	
	$M = \frac{1}{k_\mathrm{m}}\sqrt{{k_\mathrm{m}}^2 - k_\mathrm{Dx}^2}$	$M = \frac{1}{k_\mathrm{m}}\sqrt{{k_\mathrm{m}}^2 - k_\mathrm{Dx}^2 - k_\mathrm{Dy}^2}$
Vectors $\mathbf{r}$, $\mathbf{s}_0$, $\mathbf{t}_\perp$	$\mathbf{r} = (x, z)$ $\mathbf{s}_0 = (-\sin\phi_0,\, \cos\phi_0)$ $\mathbf{t}_\perp = (\cos\phi_0,\, \sin\phi_0)$	$\mathbf{r} = (x, y, z)$ $\mathbf{s_0} = (-\sin\phi_0,\, 0,\, \cos\phi_0)$ $\mathbf{t}_\perp = \left(\cos\phi_0,\, \frac{k_\mathrm{Dy}}{k_\mathrm{Dx}},\, \sin\phi_0\right)$

Table A.4, Backpropagation in 2D and in 3D. As noted in table A.2, the Fourier diffraction theorems in 2D and 3D are similar. The only differences originate from the different number of dimensions.

B. Evaluation software

B.1 General

I performed all data analysis in this work using Python 2.7.6 and the following scientific libraries:

- numpy 1.10.1 (`http://numpy.org`)
- PyFFTW 0.9.2 (based on the FFTW library [Fri+98])
- scipy 0.13.3 (`http://scipy.org`)
- scikit-image 0.11.3 [Wal+14]
- trackpy 0.2.4 [All+14]
- unwrap 0.1.1 [Her+02] (recently moved to scikit-image)

B.2 Near-field scattering

For the computation of scattered fields from theoretical cell phantoms, I made use of several software packages:

Software	Version	Approach	Use cases	Developers
bornscat	0.1.0	Born/Rytov approximation	2D phantom	P. Müller [Mül]
GMM-FIELD	2009-07-13	Mie theory	sphere	M. Ringler [Rin08]
MEEP	1.2.1	FDTD method	2D & 3D phantoms	A. Oskooi, S. G. Johnson, and others [Osk+10]
miefield	0.0.1	Mie theory	cylinder	P. Müller, H. Suárez [Mül+15a]; transl. from [Zhu11]

Table B.1, Scattering software. The table lists the software libraries for near field scattering and indicates what I used them for. Mie theory was only used for spheres or cylinders. The other approaches were used for inhomogeneous objects as well. A resourceful compendium of light scattering code is provided by Thomas Wriedt at `http://www.scattport.org/index.php/light-scattering-software`.

B.3 Phase imaging

In the course of this work, I wrote software for the analysis of quantitative phase data, including phase-retrieval in digital holographic microscopy, background-correction of phase and amplitude data, and refractive index estimation of spherical cells. The software described here has not been published and is available upon request.

Software	Version	Description
dhmlib	0.2.1	Python library for phase-retrieval, background-correction, refractive index computation using a sphere model, and more; partly inspired by a LabView script by Schürman et al. [Sch+15].
`raw2field.py`	0.3.2	batch script that converts raw data (DHM, SID4BIO) to quantitative phase images; detects and crops cell ROI and stores complex fields for further analysis; based on dhmlib
`field2ri.py`	0.3.2	batch script that computes the average RI for the cells detected with `raw2field.py`; equivalent to the technique described in [Sch+15]; based on dhmlib

Table B.2, Phase-imaging software. abbreviations: DHM: digital holographic microscopy, RI: refractive index, ROI: region of interest, SID4BIO: quantitative phase imaging camera described in section 4.1.2; The listed software is available upon request.

B.4 Numerical focusing

The backpropagation algorithm with the Rytov approximation requires data that are focused onto the rotational axis of the cell. If the experimental data are defocused, it will have to be refocused using a numerical focusing algorithm. I implemented a numerical focusing algorithm that is based on the propagation of the angular spectrum. To propagate a complex field $u_\mathrm{B}(x, y)$ by a distance Δz, the Fourier transform of the field is multiplied by the factor $\exp(ik_\mathrm{m} M\,\Delta z)$ [Sal+91; Goo05]

$$u_\mathrm{B}(x_\mathrm{D}, y_\mathrm{D}, z_0 + \Delta z) = \mathrm{FFT}_\mathrm{2D}^{-1}\left\{e^{ik_\mathrm{m} M\,\Delta z} \cdot \mathrm{FFT}_\mathrm{2D}\left\{u_\mathrm{B}(x_\mathrm{D}, y_\mathrm{D}, z_0)\right\}\right\} \tag{B.1}$$

$$M = \frac{1}{k_\mathrm{m}}\sqrt{1 - k_\mathrm{Dx}^2 - k_\mathrm{Dy}^2} \tag{B.2}$$

where FFT_2D is the 2D Fourier transform of the detector image $(x_\mathrm{D}, y_\mathrm{D})$ and $(k_\mathrm{Dx}, k_\mathrm{Dy})$ are the corresponding coordinates in Fourier space.

For experimental data, the exact focal position is usually not known. To find the correct focal position, automatic focusing algorithms are commonly applied.

Software	Version	Description
nrefocus	0.1.4	Python library for numerical focusing; supports optical transfer functions based on the Helmholtz equation and the Fresnel approximation; includes metrics and a minimizer for autofocusing [Mül13a]

Table B.3, Autofocusing software.

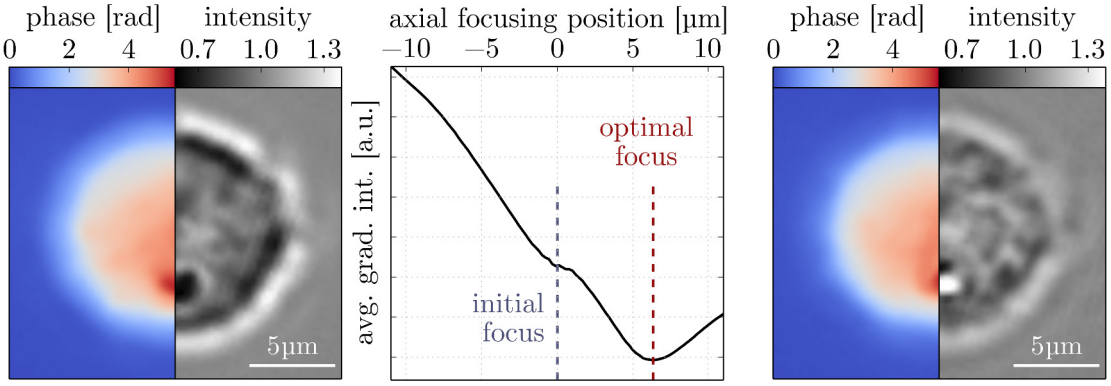

(a) initial data **(b) autofocusing** **(c) focused data**

Figure B.1, Numerical autofocusing. a) The measured complex field of an human myelocytic leukemia cell (HL60/S4) is defocused. **b)** By minimizing the average gradient of the intensity image, numerical autofocusing determines the optimal focus at an axial position of 6.35 µm. **c)** The refocused phase image is less blurry and the intensity image does not exhibit the strong halo visible in (a).

These algorithms minimize a predefined image metric to find the optimal focus. In this work, I used the average gradient of the intensity image [Lan+08; Wu+14]. Experience shows that this metric is ideal for dielectric objects such as cells, because they become hardly visible in the intensity image. The working principle of the autofocusing step is illustrated in figure B.1. The initial intensity image exhibits a strong halo, indicating that it is defocused. After finding the minimum in the average gradient with the automatic focusing algorithm, the halo in the intensity image is much weaker. In addition, the phase image becomes less blurry. Numerical autofocusing is a critical component in optical diffraction tomography, but it requires the phase *and* intensity images of the cell.

B.5 Tomographic reconstruction

I have implemented the tomographic reconstruction algorithms used in this work, backprojection and backpropagation, in two separate packages shown in table B.4. Many tomographic reconstruction algorithms exist that are based on the inverse Radon transform. However, reconstruction algorithms for 3D diffraction tomogra-

phy were publicly unavailable prior to my work. To allow a comparison between these two tomographic reconstruction algorithms, I implemented the backprojection and backpropagation algorithm in an identical way. The necessary function-

Software	Version	Description
ODTbrain	0.1.4	Python library that provides image reconstruction algorithms for **O**ptical **D**iffraction **T**omography with a **B**orn and **R**ytov **A**pproximation-based **I**nversion to compute the refractive index ($\boldsymbol{n}$) in 2D and in 3D [Mül+15b]
radontea	0.1.8	Python collection of algorithms to compute the inverse Radon transform; In this work, only the backprojection algorithm is used [Mül13b]

Table B.4, Tomographic reconstruction software.

alities to convert data in the form of a sinogram of complex-valued fields to phase data for backprojection or to complex phase data for backpropagation with the Rytov approximation are available in the ODTbrain library.

In addition to the ODTbrain library, I wrote Python scripts to automatically align the images of a sinogram, determine the rotational position of the cell in each sinogram image, and backpropagate the entire data set with the Rytov approximation. These Python scripts are listed in table B.5.

Software	Version	Description
`field_align.py`	0.3.2	batch script that performs translational image alignment; uses output of `raw2field.py` (tab. B.2)
`determine_rotation_pt.py`	0.3.2	batch script that determines the rotational position of a rotating cell by tracking a diffraction spot in the intensity image; uses output of `field_align.py`
`backpropagate.py`	0.3.2	batch script for backpropagation with the Rytov approximation (based on ODTbrain, tab. B.4); uses output of `field_align.py` and `determine_rotation_pt.py`

Table B.5, Preprocessing software for diffraction tomography. The listed software is available upon request.

C. Sample preparation

The human myelocytic leukemia cells (HL60/S4) were cultured under standard conditions at 37 °C, 5 % CO_2 in Roswell Park Memorial Institute (RPMI) medium (Gibco, Thermo Fisher Scientific, Waltham, MA, USA). The cell culture medium was supplemented with 10 % fetal bovine serum (FBS) and 1 % penicillin-streptomycin (Gibco). Prior to the measurement, the cells were centrifuged at 115 g_0 (g_0, standard gravity) for 5 min at 23 °C and resuspended in phosphate buffered saline (PBS). The cells were imaged at room temperature ($\approx$ 22 °C).

Bibliography

[Akn+15] S. Aknoun, P. Bon, J. Savatier, B. Wattellier, and S. Monneret. „Quantitative retardance imaging of biological samples using quadriwave lateral shearing interferometry“. *Optics Express* **23**:12, (2015), pp. 16383–16406. DOI: 10.1364/OE.23.016383 (cit. on p. 39).

[Alf66] J. B. Alfredo. *Dipole Radiation in the Presence of a Conducting Half-Space (International series of monographs in electromagnetic waves)*. 1st ed. Vol. 9. Pergamon Press, (1966). DOI: 10.1016/0016-0032(66)90364-4 (cit. on p. 62).

[All+14] D. B. Allan, T. A. Caswell, and N. C. Keim. *Trackpy (version 0.2.4) [Software]*. (2014). DOI: 10.5281/zenodo.9971. URL: https://github.com/soft-matter/trackpy (cit. on p. 69).

[AN+11] J. Als-Nielsen and D. McMorrow. *Elements of Modern X-ray Physics*. 2nd ed. John Wiley & Sons, Ltd, (2011). ISBN: 9780470973950. DOI: 10.1002/9781119998365 (cit. on p. 17).

[Bar52] R. Barer. „Interference Microscopy and Mass Determination“. *Nature* **169**:4296, (1952), pp. 366–367. DOI: 10.1038/169366b0 (cit. on pp. 1, 45).

[Ber94] J.-P. Berenger. „A Perfectly Matched Layer for the Absorption of Electromagnetic Waves“. *Journal of Computational Physics* **114**:2, (1994), pp. 185–200. DOI: 10.1006/jcph.1994.1159 (cit. on p. 7).

[Boh+08] C. F. Bohren and D. R. Huffman. *Absorption and Scattering of Light by Small Particles*. John Wiley & Sons, (2008). ISBN: 9780471293408. DOI: 10.1002/9783527618156 (cit. on p. 6).

[Bon+09] P. Bon, G. Maucort, B. Wattellier, and S. Monneret. „Quadriwave lateral shearing interferometry for quantitative phase microscopy of living cells“. *Optics Express* **17**:15, (2009), pp. 13080–13094. DOI: 10.1364/OE.17.013080 (cit. on p. 39).

[Boy+11] L. Boyde, K. J. Chalut, and J. Guck. „Near- and far-field scattering from arbitrary three-dimensional aggregates of coated spheres using parallel computing“. *Physical Review E* **83**:2, (2011), p. 26701. DOI: 10.1103/PhysRevE.83.026701 (cit. on p. 6).

[Boy+12] L. Boyde, A. Ekpenyong, G. Whyte, and J. Guck. „Comparison of stresses on homogeneous spheroids in the optical stretcher computed with geometrical optics and generalized Lorenz-Mie theory“. *Applied Optics* **51**:33, (2012), pp. 7934–7944. DOI: 10.1364/AO.51.007934. (cit. on p. 6).

[Bra13] W. L. Bragg. „The Structure of Some Crystals as Indicated by Their Diffraction of X-rays“. In: *Proceedings of the Royal Society of London A: Mathematical and Physical Sciences* **89**:610, (1913), pp. 248–277. ISBN: 09501207. DOI: 10.1098/rspa.1913.0083 (cit. on p. 17).

[Bra56] R. N. Bracewell. „Strip Integration in Radio Astronomy“. *Australian Journal of Physics* **9**:2, (1956), pp. 198–217. DOI: 10.1071/PH560198 (cit. on p. 56).

[Bro+76] R. A. Brooks and G. D. Chiro. „Principles of computer assisted tomography (CAT) in radiographic and radioisotopic imaging“. *Physics in Medicine and Biology* **21**:5, (1976), p. 689. DOI: 10.1088/0031-9155/21/5/001 (cit. on pp. 56, 57).

[Can86] J. Canny. „A Computational Approach to Edge Detection“. *IEEE Transactions on Pattern Analysis and Machine Intelligence* **8**:6, (1986), pp. 679–698. DOI: 10.1109/tpami.1986.4767851 (cit. on p. 42).

[Cha+06] F. Charrière, A. Marian, F. Montfort, J. Kuehn, T. Colomb, E. Cuche, P. Marquet, and C. Depeursinge. „Cell refractive index tomography by digital holographic microscopy“. *Optics Letters* **31**:2, (2006), pp. 178–180. DOI: 10.1364/ol.31.000178 (cit. on p. 35).

[Cha+12] K. J. Chalut, A. E. Ekpenyong, W. L. Clegg, I. C. Melhuish, and J. Guck. „Quantifying cellular differentiation by physical phenotype using digital holographic microscopy“. *Integrative biology : quantitative biosciences from nano to macro* **4**:3, (2012), pp. 280–284. DOI: 10.1039/c2ib00129b (cit. on p. 2).

[Cha+15] C. J. Chan, A. E. Ekpenyong, S. Golfier, W. Li, K. J. Chalut, O. Otto, J. Elgeti, J. Guck, and F. Lautenschläger. „Myosin II Activity Softens Cells in Suspension“. *Biophysical Journal* **108**:8, (2015), pp. 1856–1869. DOI: 10.1016/j.bpj.2015.03.009 (cit. on p. 37).

[Cha05] J.-C. Chanteloup. „Multiple-wave lateral shearing interferometry for wave-front sensing“. *Applied Optics* **44**:9, (2005), pp. 1559–1571. DOI: 10.1364/AO.44.001559 (cit. on p. 38).

[Che+98] B. Chen and J. J. Stamnes. „Validity of Diffraction Tomography Based on the First Born and the First Rytov Approximations“. *Applied Optics* **37**:14, (1998), pp. 2996–3006. DOI: 10.1364/AO.37.002996 (cit. on p. 13).

[Cho+07] W. Choi, C. Fang-Yen, K. Badizadegan, S. Oh, N. Lue, R. R. Dasari, and M. S. Feld. „Tomographic phase microscopy“. *Nature Methods* **4**:9, (2007), pp. 717–719. DOI: 10.1038/nmeth1078 (cit. on pp. 2, 35).

[Cho+12] W. J. Choi, K. S. Park, T. J. Eom, M.-K. Oh, and B. H. Lee. „Tomographic imaging of a suspending single live cell using optical tweezer-combined full-field optical coherence tomography“. *Optics Letters* **37**:14, (2012), pp. 2784–2786. DOI: 10.1364/OL.37.002784 (cit. on p. 27).

[Cro+70] R. A. Crowther, D. J. DeRosier, and A Klug. „The Reconstruction of a Three-Dimensional Structure from Projections and its Application to Electron Microscopy“. In: *Proceedings of the Royal Society of London A: Mathematical and Physical Sciences* **317**:1530, (1970), pp. 319–340. DOI: 10.1098/rspa.1970.0119 (cit. on p. 57).

[CT+92] C. Cohen-Tannoudji, B. Diu, and F. Laloe. *Quantum Mechanics*. 2 volume set, 1st ed. Wiley-VCH, (1992). ISBN: 9780471569527 (cit. on pp. 10, 11).

[Dav+52] H. G. Davies and M. H. F. Wilkins. „Interference Microscopy and Mass Determination“. *Nature* **169**:4300, (1952), p. 541. DOI: 10.1038/169541a0 (cit. on pp. 1, 45).

[Far+06] A. Farjadpour, D. Roundy, A. Rodriguez, M. Ibanescu, P. Bermel, J. D. Joannopoulos, S. G. Johnson, and G. Burr. „Improving accuracy by subpixel smoothing in FDTD“. *Optics Letters* **31**:20, (2006), pp. 2972–2974. DOI: 10.1364/ol.31.002972 (cit. on p. 8).

[Fri+98] M. Frigo and S. G. Johnson. „FFTW: an adaptive software architecture for the FFT“. In: *Proceedings of the 1998 IEEE International Conference on Acoustics, Speech and Signal Processing* **3**, (1998), pp. 1381–1384. DOI: 10.1109/ICASSP.1998.681704 (cit. on p. 69).

[Gab48] D. Gabor. „A New Microscopic Principle“. *Nature* **161**:4098, (1948), pp. 777–778. DOI: 10.1038/161777a0 (cit. on p. 35).

[Goo05] J. W. Goodman. *Introduction to Fourier Optics*. 3rd ed. Ben Roberts, (2005), p. 491. ISBN: 0974707724 (cit. on pp. 17, 70).

[Guc+05] J. Guck, S. Schinkinger, B. Lincoln, F. Wottawah, S. Ebert, M. Romeyke, D. Lenz, H. M. Erickson, R. Ananthakrishnan, D. Mitchell, J. Käs, S. Ulvick, and C. Bilby. „Optical deformability as an inherent cell marker for testing malignant transformation and metastatic competence“. *Biophysical journal* **88**:5, (2005), pp. 3689–3698. DOI: 10.1529/biophysj.104.045476 (cit. on pp. 36, 49).

[Hab+15] M. Habaza, B. Gilboa, Y. Roichman, and N. T. Shaked. „Tomographic phase microscopy with 180° rotation of live cells in suspension by holographic optical tweezers“. *Optics Letters* **40**:8, (2015), pp. 1881–1884. DOI: 10.1364/OL.40.001881 (cit. on p. 35).

[Her+02] M. A. Herráez, D. R. Burton, M. J. Lalor, and M. A. Gdeisat. „Fast two-dimensional phase-unwrapping algorithm based on sorting by reliability following a noncontinuous path“. *Applied Optics* **41**:35, (2002), pp. 7437–7444. DOI: 10.1364/AO.41.007437 (cit. on pp. 13, 69).

[Hos+15] P. Hosseini, Y. Sung, Y. Choi, N. Lue, Z. Yaqoob, and P. So. „Scanning color optical tomography (SCOT)“. *Optics Express* **23**:15, (2015), pp. 19752–19762. DOI: 10.1364/OE.23.019752 (cit. on p. 35).

[Isi+11] S. O. Isikman, W. Bishara, S. Mavandadi, F. W. Yu, S. Feng, R. Lau, and A. Ozcan. „Lens-free optical tomographic microscope with a large imaging volume on a chip“. In: *Proceedings of the National Academy of Sciences* **108**:18, (2011), pp. 7296–7301. ISBN: 0027-8424. DOI: 10.1073/pnas.1015638108 (cit. on p. 35).

[Kak+01] A. C. Kak and M. G. Slaney. *Principles of Computerized Tomographic Imaging*. Ed. by R. E. O'Malley. SIAM, (2001), p. 327. ISBN: 089871494X. DOI: 10.1137/1.9780898719277. URL: http://www.slaney.org/pct/pct-toc.html (cit. on pp. 9, 13, 49, 51, 52, 54).

[Kim+13] K. Kim, K. S. Kim, H. Park, J. C. Ye, and Y. Park. „Real-time visualization of 3-D dynamic microscopic objects using optical diffraction tomography“. *Optics Express* **21**:26, (2013), pp. 32269–32278. DOI: 10.1364/OE.21.032269 (cit. on p. 21).

[Kol+14] T. Kolb, S. Albert, M. Haug, and G. Whyte. „Optofluidic rotation of living cells for single-cell tomography“. *Journal of Biophotonics* **8**:3, (2014), pp. 239–246. DOI: 10.1002/jbio.201300196 (cit. on pp. 35, 37, 43, 49).

[Kos+14] J. Kostencka, T. Kozacki, M. Dudek, and M. Kujawińska. „Noise suppressed optical diffraction tomography with autofocus correction“. *Optics Express* **22**:5, (2014), pp. 5731–5745. DOI: 10.1364/OE.22.005731 (cit. on pp. 29, 35).

[Kos+15] J. Kostencka, T. Kozacki, A. Kuś, and M. Kujawińska. „Accurate approach to capillary-supported optical diffraction tomography“. *Optics Express* **23**:6, (2015), p. 7908. DOI: 10.1364/OE.23.007908 (cit. on pp. 21, 35).

[Kou+09] S. S. Kou and C. J. R. Sheppard. „Image formation in holographic tomography: high-aperture imaging conditions“. *Applied Optics* **48**:34, (2009), H168–H175. DOI: 10.1364/AO.48.00H168 (cit. on p. 31).

[Kre+08] M. K. Kreysing, T. Kießling, A. Fritsch, C. Dietrich, J. Guck, and J. A. Käs. „The optical cell rotator“. *Optics Express* **16**:21, (2008), pp. 912–914. DOI: 10.1364/oe.16.016984 (cit. on p. 35).

[Kre+14] M. Kreysing, D. Ott, M. J. Schmidberger, O. Otto, M. Schürmann, E. Martín-Badosa, G. Whyte, and J. Guck. „Dynamic operation of optical fibres beyond the single-mode regime facilitates the orientation of biological cells“. *Nature Communications* **5**:5481, (2014). DOI: 10.1038/ncomms6481 (cit. on p. 35).

[Kuj+14] M. Kujawińska, B. Kemper, A. Kus, M. Dudek, W. Krauze, J. Kostencka, and T. Kozacki. „Problems and Solutions in Tomographic Analysis of Phase Biological Objects“. In: *Fringe 2013*. Ed. by W. Osten. Springer Berlin Heidelberg, (2014), pp. 671–676. ISBN: 978-3-642-36358-0. DOI: 10.1007/978-3-642-36359-7_124 (cit. on p. 35).

[Lan+08] P. Langehanenberg, B. Kemper, D. Dirksen, and G. von Bally. „Autofocusing in digital holographic phase contrast microscopy on pure phase objects for live cell imaging“. *Applied Optics* **47**:19, (2008), pp. D176–D182. DOI: 10.1364/AO.47.00D176 (cit. on p. 71).

[LaR+08] S. J. LaRoque, E. Y. Sidky, and X. Pan. „Accurate image reconstruction from few-view and limited-angle data in diffraction tomography“. *Journal of the Optical Society of America A, Optics and Image Science* **25**:7, (2008), pp. 1772–1782. DOI: 10.1364/JOSAA.25.001772 (cit. on pp. 31, 35).

[Lin+07] B. Lincoln, F. Wottawah, S. Schinkinger, S. Ebert, and J. Guck. „High-Throughput Rheological Measurements with an Optical Stretcher“. In: *Cell Mechanics*. Vol. 83. Methods in Cell Biology. Academic Press, (2007), pp. 397–423. DOI: 10.1016/S0091-679X(07)83017-2 (cit. on p. 36).

[Lin+14] Y.-C. Lin and C.-J. Cheng. „Sectional imaging of spatially refractive index distribution using coaxial rotation digital holographic microtomography“. *Journal of Optics* **16**:6, (2014), p. 65401. DOI: 10.1088/2040-8978/16/6/065401 (cit. on p. 35).

[Lue+08] N. Lue, W. Choi, G. Popescu, K. Badizadegan, R. R. Dasari, and M. S. Feld. „Synthetic aperture tomographic phase microscopy for 3D imaging of live cells in translational motion“. *Optics Express* **16**:20, (2008), pp. 16240–16246. DOI: 10.1364/OE.16.016240 (cit. on p. 35).

[Mer76] R. M. Mersereau. „Direct fourier transform techniques in 3-D image reconstruction“. *Computers in Biology and Medicine* **6**:4, (1976), pp. 247–258. DOI: 10.1016/0010-4825(76)90064-0 (cit. on pp. 56, 57).

[Mor+53] P. M. Morse and H. Feshback. *Methods of Theoretical Physics*. 2 volume set, 1st ed. McGraw Hill, (1953). ISBN: 9780976202127 (cit. on p. 11).

[Mou+06] S. Mousset, C. Rouyer, G. Marre, N. Blanchot, S. Montant, and B. Wattellier. „Piston measurement by quadriwave lateral shearing interferometry“. *Optics Letters* **31**:17, (2006), pp. 2634–2636. DOI: 10.1364/OL.31.002634 (cit. on pp. 35, 38).

[Mül] P. Müller. *bornscat: Python library to compute forward scattering with the Born or Rytov approximation (version 0.1.0) [Software]*. URL: https://github.com/RI-imaging/bornscat (cit. on p. 69).

[Mül+15a] P. Müller and H. Suárez. *miefield: Python library to compute the near field behind cylindrical scatterers (version 0.0.1) [Software]*. (2015). URL: https://github.com/RI-imaging/miefield (cit. on p. 69).

[Mül+15b] P. Müller, M. Schürmann, and J. Guck. „ODTbrain: a Python library for full-view, dense diffraction tomography“. *BMC Bioinformatics* **16**:1, (2015), pp. 1–9. DOI: 10.1186/s12859-015-0764-0. URL: https://pypi.python.org/pypi/odtbrain (cit. on pp. 8, 23, 26, 27, 30, 49, 72).

[Mül+15c] P. Müller, M. Schürmann, C. J. Chan, and J. Guck. „Single-cell diffraction tomography with optofluidic rotation about a tilted axis“. In: *Proceedings of the International Society for Optics and Photonics* **9548**, (2015), 95480U. DOI: 10.1117/12.2191501 (cit. on p. 33).

[Mül+15d] P. Müller, M. Schürmann, and J. Guck. *The Theory of Diffraction Tomography*. Version 2. (2015). arXiv: 1507.00466v2 [q-bio.QM] (cit. on pp. 14, 17, 18, 24, 51, 58, 62, 66, 68).

[Mül13a] P. Müller. *nrefocus: Python algorithms for numerical focusing (version 0.1.4) [Software]*. (2013). URL: https://pypi.python.org/pypi/nrefocus/ (cit. on p. 71).

[Mül13b] P. Müller. *radontea: Python algorithms for the inversion of the Radon transform (version 0.1.8) [Software]*. (2013). URL: https://pypi.python.org/pypi/radontea/ (cit. on pp. 21, 58, 72).

[Osk+10] A. F. Oskooi, D. Roundy, M. Ibanescu, P. Bermel, J. D. Joannopoulos, and S. G. Johnson. „MEEP: A flexible free-software package for electromagnetic simulations by the FDTD method“. *Computer Physics Communications* **181**:3, (2010), pp. 687–702. DOI: 10.1016/j.cpc.2009.11.008 (cit. on pp. 7, 69).

[Pop+08] G. Popescu, Y. Park, N. Lue, C. Best-Popescu, L. Deflores, R. R. Dasari, M. S. Feld, and K. Badizadegan. „Optical imaging of cell mass and growth dynamics“. *American Journal of Physiology - Cell Physiology* **295**:2, (2008), pp. C538–C544. DOI: 10.1152/ajpcell.00121.2008 (cit. on p. 2).

[Rad17] J. Radon. *Über die Bestimmung von Funktionen durch ihre Integralwerte längs gewisser Mannigfaltigkeiten*. German. Tech. rep. Leipzig: Berichte über die Verhandlungen der Königlich-Sächsischen Gesellschaft der Wissenschaften zu Leipzig, (1917), pp. 262–277. DOI: 10.1090/psapm/027/692055 (cit. on pp. 9, 18).

[Ram+71] G. N. Ramachandran and A. V. Lakshminarayanan. „Three-dimensional reconstruction from radiographs and electron micrographs: application of convolutions instead of Fourier transforms". In: *Proceedings of the National Academy of Sciences of the United States of America* **68**:9, National Academy of Sciences, (1971), pp. 2236–2240. DOI: 10.1073/pnas.68.9.2236 (cit. on p. 57).

[Rin08] M. Ringler. „Plasmonische Nahfeldresonatoren aus zwei biokonjugierten Goldnanopartikeln". German. PhD thesis. Ludwig-Maximilians-Universität München, (2008). URL: http://nbn-resolving.de/urn:nbn:de:bvb:19-84894 (cit. on pp. 10, 69).

[Sal+91] B. E. A. Saleh and M. C. Teich. *Fundamentals of Photonics*. 1st ed. John Wiley & Sons, Inc., (1991). ISBN: 9780471839651. DOI: 10.1002/0471213748 (cit. on p. 70).

[Sch+15] M. Schürmann, J. Scholze, P. Müller, C. J. Chan, A. E. Ekpenyong, K. J. Chalut, and J. Guck. „Refractive index measurements of single, spherical cells using digital holographic microscopy". In: *Biophysical Methods in Cell Biology*. Ed. by E. K. Paluch. Vol. 125. Methods in Cell Biology. Academic Press, (2015), pp. 143–159. DOI: 10.1016/bs.mcb.2014.10.016 (cit. on pp. 38, 40, 47, 70).

[Sla+84] M. G. Slaney, A. C. Kak, and L. E. Larsen. „Limitations of Imaging with First-Order Diffraction Tomography". *IEEE Transactions on Microwave Theory and Techniques* **32**:8, (1984), pp. 860–874. DOI: 10.1109/TMTT.1984.1132783 (cit. on pp. 49, 54).

[Sla85] M. G. Slaney. „Imaging with diffraction tomography". PhD thesis. Purdue University, (1985). URL: https://engineering.purdue.edu/~malcolm/purdue/DiffractionTomographyThesis/ (cit. on p. 51).

[Su+13] J.-W. Su, W.-C. Hsu, C.-Y. Chou, C.-H. Chang, and K.-B. Sung. „Digital holographic microtomography for high-resolution refractive index mapping of live cells". *Journal of Biophotonics* **6**:5, (2013), pp. 416–24. DOI: 10.1002/jbio.201200022 (cit. on p. 21).

[Sun+09] Y. Sung, W. Choi, C. Fang-Yen, K. Badizadegan, R. R. Dasari, and M. S. Feld. „Optical diffraction tomography for high resolution live cell imaging". *Optics Express* **17**:1, (2009), pp. 266–277. DOI: 10.1364/OE.17.000266 (cit. on pp. 21, 35).

[Sun+14] Y. Sung, N. Lue, B. Hamza, J. Martel, D. Irimia, R. R. Dasari, W. Choi, Z. Yaqoob, and P. So. „Three-Dimensional Holographic Refractive-Index Measurement of Continuously Flowing Cells in a Microfluidic Channel“. *Physical Review Applied* **1**:1, (2014), p. 14002. DOI: 10.1103/PhysRevApplied.1.014002 (cit. on p. 35).

[Taf+95] A. Taflove, S. C. Hagness, and Others. *Computational Electrodynamics: The Finite-Difference Time-Domain Method*. 3rd ed. Artech House, (1995). ISBN: 978-1580538329 (cit. on p. 7).

[Tam+81] K. C. Tam and V Perez-Mendez. „Tomographical imaging with limited-angle input“. *Journal of the Optical Society of America* **71**:5, (1981), pp. 582–592. DOI: 10.1364/JOSA.71.000582 (cit. on pp. 30, 35).

[Ver+09] S. Vertu, J.-J. Delaunay, I. Yamada, and O. Haeberlé. „Diffraction microtomography with sample rotation: influence of a missing apple core in the recorded frequency space“. *Central European Journal of Physics* **7**:1, (2009), pp. 22–31. DOI: 10.2478/s11534-008-0154-6 (cit. on pp. 31, 32).

[Wal+14] S. van der Walt, J. L. Schönberger, J. Nunez-Iglesias, F. Boulogne, J. D. Warner, N. Yager, E. Gouillart, T. Yu, and the scikit-image contributors. „scikit-image: image processing in Python“. *PeerJ* **2**, (2014), e453. DOI: 10.7717/peerj.453 (cit. on p. 69).

[Wed+95] T. C. Wedberg, J. J. Stamnes, and W Singer. „Comparison of the filtered backpropagation and the filtered backprojection algorithms for quantitative tomography“. *Applied Optics* **34**:28, (1995), pp. 6575–6581. DOI: 10.1364/ao.34.006575 (cit. on pp. 23, 29, 49).

[Wis80] W. J. Wiscombe. „Improved Mie scattering algorithms“. *Applied Optics* **19**:9, (1980), pp. 1505–1509. DOI: 10.1364/AO.19.001505 (cit. on p. 6).

[Wol+86] M. Wolman and F. H. Kasten. „Polarized light microscopy in the study of the molecular structure of collagen and reticulin“. *Histochemistry* **85**:1, (1986), pp. 41–49. DOI: 10.1007/BF00508652 (cit. on p. 3).

[Wol69] E. Wolf. „Three-dimensional structure determination of semi-transparent objects from holographic data“. *Optics Communications* **1**:4, (1969), pp. 153–156. DOI: 10.1016/0030-4018(69)90052-2 (cit. on pp. 13, 17, 21, 51).

[Wu+14] S. Y. Wu, N. Dugan, and B. M. Hennelly. „Investigation of autofocus algorithms for brightfield microscopy of unstained cells“. In: *Proceedings of the International Society for Optics and Photonics* **9131**, (2014), 91310T. DOI: 10.1117/12.2051944 (cit. on pp. 29, 71).

[Yee+66] K. S. Yee and Others. „Numerical solution of initial boundary value problems involving Maxwell's equations in isotropic media“. *IEEE Transactions on Antennas and Propagation* **14**:3, (1966), pp. 302–307. DOI: 10.1109/tap.1966.1138693 (cit. on p. 7).

[Zer42a] F. Zernike. „Phase contrast, a new method for the microscopic observation of transparent objects“. *Physica* **9**:7, (1942), pp. 686–698. DOI: 10.1016/S0031-8914(42)80035-X (cit. on p. 35).

[Zer42b] F. Zernike. „Phase contrast, a new method for the microscopic observation of transparent objects part II“. *Physica* **9**:10, (1942), pp. 974–986. DOI: 10.1016/S0031-8914(42)80079-8 (cit. on p. 35).

[Zhu11] G. K. Zhu. *Cylinder scattering, MATLAB Central File Exchange (URL accessed 2012)*. (2011). URL: http://www.mathworks.com/matlabcentral/fileexchange/30162-cylinder-scattering (cit. on p. 69).

Acronyms

2D	two dimensions, two-dimensional *adj.*
3D	three dimensions, three-dimensional *adj.*
CT	computerized tomography
DHM	digital holographic microscopy
DNA	desoxyribonucleic acid
FBS	fetal bovine serum
FDTD	finite-difference time-domain; FDTD method: numerical computation of light propagation based on the Maxwell equations
GPU	graphical processing unit
HL60/S4	human myelocytic leukemia cell line
ODT	optical diffraction tomography
PBS	phosphate buffered saline (buffer solution)
RI	refractive index
RMS	root-mean-square metric; the RMS error quantifies tomographic reconstruction quality, see equation 3.10
RPMI	Roswell Park Memorial Institute (cell culture medium)
SART	simultaneous algebraic reconstruction technique
SD	standard deviation
TV	total variation metric; the TV error quantifies tomographic reconstruction quality, see equation 3.11

Notation

Vector
Vectors are printed as bold symbols. To simplify the comparison between 2D and 3D backpropagation algorithms, 2D vectors are defined in the x-z-plane, e.g.

$$\mathbf{r} = (x, z) \tag{2D}$$
$$\mathbf{r} = (x, y, z). \tag{3D}$$

Fourier transform
The unitary angular frequency form of the Fourier transform is used. The Fourier transform $\widehat{F}(\mathbf{k})$ of a function $f(\mathbf{r})$ and its inverse are defined in N dimensions as

$$\widehat{F}(\mathbf{k}) = \frac{1}{(2\pi)^{N/2}} \iint d^N r\, f(\mathbf{r}) \exp(-i\mathbf{kr}) \qquad \text{(Fourier transform)}$$
$$f(\mathbf{r}) = \frac{1}{(2\pi)^{N/2}} \iint d^N k\, \widehat{F}(\mathbf{k}) \exp(i\mathbf{kr}). \qquad \text{(inverse Fourier transform)}$$

Delta distribution
The Dirac delta distribution is defined by the following identity:

$$\delta(p-a) = \frac{1}{2\pi} \int dx\, \exp(i(p-a)x)$$

Nabla operator
The Nabla operator is defined in 2D and in 3D following the above definition of vectors.

$$\nabla = \left(\frac{\partial}{\partial x}, \frac{\partial}{\partial z}\right) = (\partial_x, \partial_z) \tag{2D}$$
$$\nabla = \left(\frac{\partial}{\partial x}, \frac{\partial}{\partial y}, \frac{\partial}{\partial z}\right) = (\partial_x, \partial_y, \partial_z) \tag{3D}$$

The Nabla operator is used to define derivatives such as gradient (scalar product), divergence (dot product), and curl (cross product), for instance:

$$\nabla \cdot f(\mathbf{r}) \qquad \text{(gradient of the scattering potential } f(\mathbf{r})\text{)}$$
$$\nabla \cdot \mathbf{B}(\mathbf{r}, t) \qquad \text{(divergence of the magnetic field } \mathbf{B}(\mathbf{r}, t)\text{)}$$
$$\nabla \times \mathbf{E}(\mathbf{r}, t) \qquad \text{(curl of the electric field } \mathbf{E}(\mathbf{r}, t)\text{)}$$

Symbols

a_0	amplitude of a plane wave $u_0(\mathbf{r})$
α	refraction increment
$\mathbf{B}(\mathbf{r}, t)$	magnetic field
c_0	speed of light in vacuum
c	speed of light in a dielectric medium $c = {c_0}/{n_\mathrm{m}}$
d	diameter of an object
d_c	characteristic distance for the validity criterion of the Rytov approximation
$D_{-\phi_j}$	rotation operator that rotates by $-\phi_j$ about the y-axis
$D^\mathrm{tilt}_{-\phi_j}$	rotation operator that rotates by $-\phi_j$ about a tilted axis
$\mathbf{D}(\mathbf{r}, t)$	electric displacement field
$\delta(\mathbf{r})$	delta distribution
Δd_opt	relative optical thickness of an object compared to the surrounding medium
$\mathbf{E}(\mathbf{r}, t)$	electric field
$\epsilon_n(\mathbf{r})$	local variation of the refractive index, $\epsilon_n(\mathbf{r}) = n(\mathbf{r}) - n_\mathrm{m}$
ε_0	permittivity of free space
$\varepsilon_\mathrm{r}(\mathbf{r})$	relative permittivity of a material, describes how electric charges influence electromagnetic fields
$f(\mathbf{r})$	scattering potential/object function; the inhomogeneity in the Helmholtz equation defined by the refractive index, $f(\mathbf{r}) = {k_\mathrm{m}}^2 \left[\left({n(\mathbf{r})}/{n_\mathrm{m}} \right)^2 - 1 \right]$
$\widehat{F}(\mathbf{k})$	Fourier transform of $f(\mathbf{r})$
$\mathrm{FFT}_{N\mathrm{D}}$	Fast Fourier transform operator in N dimensions. The inverse operator is depicted as $\mathrm{FFT}^{-1}_{N\mathrm{D}}$
$G(\mathbf{r})$	Green's function of the Helmholtz equation

$H_0^{(1)}(x)$	zero order Hankel function of the first kind with argument x
$\mathbf{H}(\mathbf{r}, t)$	magnetizing field
$I(\mathbf{r})$	intensity of an optical wave
$\mathbf{j}_\mathrm{f}(\mathbf{r}, t)$	free current density
$\mathbf{k}$	coordinate vector in Fourier space
$\mathbf{k}$	wave vector of an electromagnetic wave with the wave number $k = \lvert\mathbf{k}\rvert = {}^{2\pi n}/_{\lambda}$
$\mathbf{k_D}$	Fourier coordinates corresponding to the spatial detector coordinates $\mathbf{r_D}$
k_m	wave number in a medium with refractive index n_m, $k_\mathrm{m} = {}^{2\pi n_\mathrm{m}}/_{\lambda}$
l_D	distance between rotational center and detector plane
λ	vacuum wavelength of the light that is used for image acquisition
M	z-component of the unit vector $\mathbf{s}$
$\mathbf{M}(\mathbf{r}, t)$	magnetization field
μ_0	permeability of free space
$\mu_\mathrm{r}(\mathbf{r})$	relative permeability of a material, describes how magnetic dipoles influence electromagnetic fields
$n(\mathbf{r})$	refractive index distribution of a sample, $n(\mathbf{r}) = n_\mathrm{m}\,(1 + \epsilon_n(\mathbf{r}))$
n_m	refractive index of a medium
N_A	number of images/projections in a sinogram
ω	angular frequency of an electromagnetic wave
p	x-component of the unit vector $\mathbf{s}$
$p_{\phi_0}(\mathbf{r_D})$	projection of an object onto a line (2D) or plane (3D) defined by $\mathbf{r_D}$ at a rotational angle ϕ_0
$\widehat{P}_{\phi_0}(\mathbf{k_D})$	Fourier transform of $p_{\phi_0}(\mathbf{r_D})$
$\mathbf{P}(\mathbf{r}, t)$	polarization field
ϕ_0	acquisition angle of a projection in a sinogram
$\varphi(\mathbf{r})$	complex phase of a scattered wave, $u(\mathbf{r}) = \exp(\varphi(\mathbf{r}))$
$\varphi_0(\mathbf{r})$	complex phase of a plane wave, $u_0(\mathbf{r}) = \exp(\varphi_0(\mathbf{r}))$
$\varphi_\mathrm{s}(\mathbf{r})$	scattering component of a complex phase $\varphi(\mathbf{r}) = \varphi_0(\mathbf{r}) + \varphi_\mathrm{s}(\mathbf{r})$

$\varphi_{\mathrm{R}}(\mathbf{r})$	Rytov approximation of $\varphi_{\mathrm{s}}(\mathbf{r})$
$\Phi(\mathbf{r})$	phase of an optical wave
$\Psi(\mathbf{r}, t)$	scalar field for the description of wave propagation
q	y-component of the unit vector $\mathbf{s}$
R_{ϕ_0}	Radon transform operator along angle ϕ_0
$\mathbf{r_D}$	detector coordinates for tomography, $\mathbf{r_D} = x_{\mathrm{D}}$ in 2D and $\mathbf{r_D} = (x_{\mathrm{D}}, y_{\mathrm{D}})$ in 3D with $z_{\mathrm{D}} = l_{\mathrm{D}}$
$\rho_{\mathrm{f}}(\mathbf{r}, t)$	free charge density
$\mathbf{s}$	normal unit vector of an arbitrary plane wave, 2D: $\mathbf{s} = (p, M)$, $p^2 + M^2 = 1$ 3D: $\mathbf{s} = (p, q, M)$, $p^2 + q^2 + M^2 = 1$
$\mathbf{s}_0$	normal unit vector of an incident plane wave, 2D: $\mathbf{s}_0 = (p_0, M_0)$, $p_0^2 + M_0^2 = 1$ 3D: $\mathbf{s}_0 = (p_0, q_0, M_0)$, $p_0^2 + q_0^2 + M_0^2 = 1$
t	time
t	variable of integration for the Radon transform
$\mathbf{t}_\perp$	unit vector perpendicular to $\mathbf{s}_0$
θ_{tilt}	tilt angle of the rotational axis of a sample with respect to the image plane
$u(\mathbf{r})$	scattered wave, $u(\mathbf{r}) = u_0(\mathbf{r}) + u_{\mathrm{s}}(\mathbf{r})$
$u_0(\mathbf{r})$	plane wave, solution to the homogeneous Helmholtz equation
$u_{\mathrm{s}}(\mathbf{r})$	scattering component of a scattered wave $u(\mathbf{r})$
$u_{\mathrm{B}}(\mathbf{r})$	Born approximation of $u_{\mathrm{s}}(\mathbf{r})$
$u_{\mathrm{B},\phi_0}(\mathbf{r_D})$	Born approximation $u_{\mathrm{B}}(\mathbf{r})$ at the detector plane $\mathbf{r_D}$ for a rotational position ϕ_0 of the sample
$u_{\mathrm{R}}(\mathbf{r})$	Rytov approximation of $u_{\mathrm{s}}(\mathbf{r})$
$\widehat{U}_{\mathrm{B}}(\mathbf{k})$	Fourier transform of $u_{\mathrm{B}}(\mathbf{r})$
$\widehat{U}_{\mathrm{B},\phi_0}(\mathbf{k_D})$	Fourier transform of $u_{\mathrm{B},\phi_0}(\mathbf{r_D})$

Acknowledgements

This thesis would not have been possible without the support of my friends and colleagues:

Prof. Jochen Guck for making this work possible. Jochen, thank you for actively supporting my personal and academic freedom, constantly encouraging me, believing in me, and always being available for discussions. I enjoyed working with you.

Mirjam Schürman for her thoughtful challenges. Mirjam, thank you for an endless number of productive discussions. You always gave invaluable feedback that constantly improved my work. It was a delight to tackle diffraction tomography with you and I am happy that our teamwork was so successful.

Moritz Kreysing, Martin Weigert, Kevin Chalut, Gheorghe Cojoc, and Chi J. Chan for many fruitful discussions in journal clubs, seminars, and other meetings. You made me view my project from different angles, which was a priceless experience and helped me to put my work into perspective. Kevin, thank you for agreeing to review this thesis.

The entire Guck group, especially Elke Ulbricht, Katrin Wagner, Janine Tittel, Nicole Träber, and Christoph Faigle for many discussions, helpful conversations, and the kind atmosphere that made me enjoy my time at the institute. In particular, I would like to thank Heike Neumann for her work as a group assistant. Heike, thank you for your patience and your help.

André Scholich, Maximilian Frydetzki, Philipp Rosendahl, Richard Hartmann, and Yannic Utz for so many wonderful chats on programming, physics, math, and pizza.

Prof. Ivo Sbalzarini and Dr. Pavel Tomančak for agreeing to be part of my thesis advisory committee, their encouraging responses, and their constructive feedback.

The computer department, especially Nick Dannenberg, Matthias Gierth, and Alexander Mestiashvili for making it possible to use the biocluster for my FDTD simulations.

The human myelocytic leukemia cells (HL60/S4) were a generous gift of D. and A. Olins (University of New England).

This project has received funding from the European Union's Seventh Framework Programme for research, technological development and demonstration under grant agreement no 282060.

Erklärung

Hiermit versichere ich, dass ich die vorliegende Arbeit ohne unzulässige Hilfe Dritter und ohne Benutzung anderer als der angegebenen Hilfsmittel angefertigt habe; die aus fremden Quellen direkt oder indirekt übernommenen Gedanken sind als solche kenntlich gemacht. Die Arbeit wurde bisher weder im Inland noch im Ausland in gleicher oder ähnlicher Form einer anderen Prüfungsbehörde vorgelegt.

Es fanden keine früheren erfolglosen Promotionsverfahren statt. Ich erkenne die Promotionsordnung der Fakultät Mathematik und Naturwissenschaften vom 23. Februar 2011 an.

Ich habe diese Arbeit von Februar 2013 bis März 2016 unter der Betreuung von Prof. Dr. Jochen Guck am Biotechnologischen Zentrum der Technischen Universität Dresden angefertigt.

Dresden, 14. März 2016